Optimisation of planning and delivery methods for Gamma Knife Stereotactic Radiosurgery

Alvaro Alexander Rojas Villabona, MBBS, MSc

Thesis submitted for the degree of:

PhD in Stereotactic Radiosurgery

Institute of Neurology, University College London

Research conducted at:

The National Hospital for Neurology and Neurosurgery

Queen Square, London

March 2018

To my loved ones

Acknowledgements

First and foremost, I thank my primary supervisor Prof Hans Rolf Jäger for his unfailing encouragement and support and Mr Neil Kitchen for his generous mentorship during my fellowship in the Gamma Knife Centre at Queen Square. Prof Xavier Golay has once again accepted me into his team and Dr Enrico de Vita more recently contributed to my work with his supervision.

The triple-MRA work would not have been possible without the tireless help of Dr Magdalena Sokolska. I am very grateful for her support and friendship.

Dr Katherine Miszkiel, Dr Thomas Solbach and Ms Joan Grieve spent many hours looking at scans, measuring landmarks and drawing target volumes for my research. I am thankful for their diligence and perseverance. I am indebted to Mr Ian Paddick for many long and illuminating discussions about the convolution algorithm and the Leksell frame.

The Gamma Knife Centre at Queen Square not only welcomed and encouraged my research but they also assisted me with many logistical tasks during my fellowship.

Dr Francesca Benedetta Pizzini, and the Gamma Knife team at University Hospital of Verona, enthusiastically recruited and scanned patients for the AVM follow-up study. I am very grateful for their collaboration.

Invaluable support and encouragement came from my fellow PhD students Dr Marilena Rega, Dr Francisco Torrealdea, Dr Kenji Yamamoto, James Fairney and

Dr Eleni Demetriou. The consultant Neurosurgeons and Neuroradiologists at the National Hospital not only allowed me to approach and study their patients but they also encouraged me and contributed to this dissertation in various other ways.

I am very grateful for the financial support that I have received for my research. Elekta (UK) Limited generously funded my three-year academic position and the Queen Square Radiosurgery Centre (QSRC) funded the convolution and frame stability projects. Along with the Department of Neurosurgery at the National Hospital, they also contributed towards my attendance at multiple scientific conferences and training courses. The AVMs project was funded by the National Brain Appeal (Small Acorns grant awarded to Alvaro Rojas-Villabona) and the EPSRC (First grant EP/K027476/1 awarded to Karin Shmueli). The Brainlab AG allowed me to use their Elements software free of charge for triple-MRA post-processing.

Abstract

The work presented in this dissertation is the response to a series of technical and clinical challenges encountered during the first four years of operations in the Gamma Knife Centre at Queen Square. These challenges, which are common to most contemporary Gamma Knife centres, were prospectively addressed and practical solutions were developed for the questions they posed.

The dosimetric differences between the new convolution algorithm and the standard TMR 10 algorithm traditionally used for prediction of dose distribution in Gamma Knife Radiosurgery (GKR) were explored. It was demonstrated that inhomogeneity correction with the convolution algorithm results in a considerable but consistent dose shift compared to TMR 10. No significant difference in relative dose distribution was noted and it was concluded that a reduction of the prescription dose is necessary to obtain the same absolute dosimetric effect with the convolution algorithm.

The stability of the stereotactic Leksell frame G in GKR was demonstrated using a comprehensive study design that involved repeated measurements of landmarks by two observers. The study provided reliable and realistic evidence of submillimetre stability of the stereotactic frame throughout the treatment procedure which is important for evaluation and development of new frameless radiosurgery systems.

The technical feasibility of using a combination of three magnetic resonance angiography sequences (triple-MRA), instead of digital subtraction angiography (DSA), for visualisation and delineation of brain Arteriovenous Malformations

(AVMs) for GKR targeting was demonstrated. Target volumes obtained using triple-MRA are on average 10% smaller than AVM targets obtained with the standard DSA planning method and this can potentially reduce the risk of adverse radiation effects (ARE). The treatment planning method described here has laid the way for a change in clinical practice that favours a less invasive treatment planning approach.

The same principle of less invasive AVM imaging with triple-MRA was used at the post-GKR stage, when a DSA is performed to confirm AVM obliteration. Triple-MRA was found to consistently confirm or rule out residual AVMs in patients who had undergone GKR for brain AVMs, compared to DSA, and it can also be reliably used for characterisation of residual AVMs. The use of triple-MRA as a first line for assessment of obliteration after GKR is recommended.

Statement of contributions

I, Alvaro Alexander Rojas Villabona, confirm that the work presented in this thesis is my own, except where specifically stated below. Where information has been derived from other sources, I confirm that this has been indicated in the thesis.

The research questions addressed in chapters 3 and 4 i.e., the dosimetric differences between the convolution and TMR 10 algorithms and the evaluation of the stability of the Leksell frame were proposed by Mr Ian Paddick. He also contributed to the design of the studies and supervised data analysis. Dr Katherine Miszkiel was one of the landmark evaluators for the frame stability study in chapter 4.

The ASL-MRA sequence used in Chapters 5 and 6 was modified with the generous help of Dr Magdalena Sokolska, from an original sequence developed by Dr Yuriko Suzuki and Prof Matthias J.P. van Osch at the Gorter Center for High Field MRI and the Department of Radiology, Leiden University Medical Center, Leiden, Netherlands. Triple-MRA datasets used for planning of GKR in chapter 6 were assessed by Dr Thomas Solbach and Ms Joan Grieve for delineation of triple-MRA volume. AVM volume delineation using the conventional DSA method was performed by the practising GKR clinical team for delivery of radiosurgery. Dr Marilena Rega and Dr Francisco Torrealdea helped with the development of a Matlab code for computation of triple-MRA and DSA volumes.

Research participants for the study in chapter 6 had previously received GKR at the University Hospital of Verona and attended follow-up DSA for clinical purposes at the same institution. They were enrolled in research and scanned with triple-MRA by Dr Francesca Benedetta Pizzini and her team in Italy. Dr Pizzini and Dr Solbach also contributed with the evaluation of follow-up triple-MRA datasets for comparison with DSA.

The manuscripts of all the experimental chapters were revised by the co-authors for publication

Contents

Acknowledgements **6**

Abstract **8**

Statement of contributions **10**

Contents **12**

Abbreviations **17**

List of tables **23**

List of figures **25**

Publications **28**

Presentations **29**

1. Introduction **31**

2. Literature review **35**

2.1 Gamma Knife Radiosurgery 35

2.2 History of Gamma Knife Radiosurgery 36

2.3 The Gamma Knife Perfexion 37

2.4 Leksell stereotactic frame G 38

2.5 Gamma Knife dosimetry 41

2.5 Clinical Applications of Gamma Knife Radiosurgery 42

2.5.1 Vestibular schwannoma 43

2.5.2 Meningioma 45

2.5.4 Brain metastases 47

2.5.3 Trigeminal Neuralgia 49

2.5.5 Arteriovenous Malformations 51

2.6 Imaging of brain AVMs 54

5.2.1 Time-Of-Flight MR Angiography 58

5.2.2 Contrast Enhanced MR Angiography 59

5.2.3 Arterial Spin Labelling MR Angiography 61

3. Investigation of dosimetric differences between the TMR 10 and convolution algorithm for Gamma Knife Stereotactic Radiosurgery 64

3.1 Abstract 64

3.2 Introduction 66

3.3 Methods 67

3.3.1 Patients 67

3.3.2 Radiosurgery planning procedure with TMR 10 68

3.3.3 CT imaging and electron density calibration 71

3.3.4 Treatment re-planning with convolution algorithm 71

3.3.5 Statistical analysis 72

3.3.6 Effect of frame and pin materials on convolution calculation 72

3.4 Results 73

3.4.1 Dosimetric effect of head approximation 76

3.4.3 Dose to organs at risk 78

3.4.4 The effect of frame and pin materials on convolution calculation 79

3.5 Discussion 80

3.5.1 Dose implications of convolution algorithm for GKR 80

3.5.2 Potential dose calculation inaccuracies with convolution 83

3.5.3 Head definition with CT 85

3.6 Conclusions 86

4. Evaluation of the stability of the stereotactic Leksell G frame in Gamma Knife Radiosurgery 87

4.1 Abstract 87

4.2 Introduction 89

4.3 Methods 90

4.3.1 Patients 90

4.3.2 Stereotactic frame and pre-treatment imaging 91

4.3.3 Post-treatment imaging and landmarks measurement 92

4.3.4 Data analysis 94

4.4 Results 95

4.5 Discussion 102

4.5.1 Intra and Inter-observer variability 103

4.5.2 Localization uncertainty due to imaging techniques 106

4.5.3 Frame stability 109

4.5.4. Effect of frame weight bearing on the stereotactic frame 110

4.6 Conclusions 110

5. Can Gamma Knife Radiosurgery for brain arteriovenous malformations be planned on triple Magnetic Resonance Angiography? 112

5.1 Abstract 112

5.2 Introduction 115

5.3 Methods 118

5.3.1 Patients 118

5.3.2 Triple-MRA imaging protocol 120

5.3.3 DSA protocol and stereotactic MRI for GKR planning 124

5.3.4 AVM target definition on triple-MRA..... 125

5.3.5 Data analysis 127

5.4 Results..... 129

5.5 Discussion 135

5.6 Conclusions..... 147

6. Triple Magnetic Resonance Angiography (triple-MRA) for confirmation of obliteration following Gamma Knife radiosurgery for brain arteriovenous malformations. 148

6.1 Abstract..... 148

6.2 Introduction..... 150

6.3 Methods..... 152

6.3.1 Patients..... 152

6.3.2 MRA imaging 153

6.3.3 DSA imaging 154

6.3.4 Data analysis 156

6.4 Results..... 158

6.4.1 Confirmation of AVM obliteration..... 158

6.4.2 Characterisation of residual AVMs in cases of incomplete response. 161

6.4.3 Image quality and reporting level of confidence 164

6.5 Discussion 166

6.6 Conclusions..... 176

7. Conclusions and future work..... 177

References..... 181

Appendices..... 211

Appendix 1. Confirmation of ethical opinion for the convolution project. 212

Appendix 2. Ethical considerations of the convolution project. 215

Appendix 3. Confirmation of ethical opinion for the study on triple-MRA for planning of GKR for brain AVMs. 217

Appendix 4. Confirmation of ethical opinion for the study on triple-MRA for confirmation of obliteration following GKR of brain AVMs. 223

Appendix 5. Evaluation forms used for assessment of DSA and triple-MRA. 225

Abbreviations

AANS	American Association of Neurological Surgeons
ANOVA	Analysis of variance
AP	Anteroposterior
ARE	Adverse radiation effects
ARUBA	A randomized trial for unruptured brain AVMs
ARV	Alvaro Rojas Villabona
ASL	Arterial spin labelling
ASL-MRA	Arterial spin labelling based angiography
ASTRO	American Society for Therapeutic Radiology and Oncology
AVM	Arteriovenous malformation
BM	Brain metastases
BNI	Barrow Neurological Institute
CB-CT	Cone beam computed tomography
CB-CTA	Cone beam computed tomography angiography
CC	Craniocaudal
CcI	Concordance index

CE	Contrast enhanced
CE-MRA	Time-resolved contrast-enhanced MRA
CENTRA	Contrast-enhanced robust timing angiography
CISS	Constructive interference in steady state
cNm	Centi Newton-metres
CNS	Congress of Neurological Surgeons
CT	Computed tomography
DBS	Deep brain stimulation
DI	Degree of inclusion
DnI	Degree of non-inclusion
DSA	Digital subtraction angiography
DSAv	AVM volume obtained with DSA
eGFR	Estimated glomerular filtration rate
EPI	Echo planar imaging
FBP	Francesca Benedetta Pizzini
FFE	Fast field echo
FISP	Fast imaging with steady state precession
FLASH	Fast low angle shot
FOV	Field of view
f/s	Frames per second
Gad	Gadolinium
GCP	Good clinical practice
GI	Gradient index

GKR	Gamma Knife Radiosurgery
GRE	Gradient recovery echo
Gy	Grey
HD-TOF	High definition time-of-flight MR angiography
HU	Hounsfield units
IASP	International Association for the Study of Pain
IFMM	Intra fraction motion management
Inf	Inferior
IV	Intravenous
JG	Joan Grieve
LGKS	Leksell Gamma Knife Society
MDT	Multi-disciplinary team
min	Minutes
min:sec	Minutes:seconds
MIPs	Maximum intensity projections
Mm	Millimetre
mmol	Millimoles
MR	Magnetic resonance
MRA	Magnetic resonance angiography
MRI	Magnetic resonance imaging
ms	Milliseconds
mSv	Microsievert
n	Number

NA	Non-applicable
NPV	Negative predictive value
OAR	Organs at risk
Obs	Observations
pCASL	Pseudo-continuous arterial spin labelling
PCI	Paddick conformity index
PPS	Patient positioning system
PPV	Positive predictive value
QSRC	Queen Square Radiosurgery Centre
RCT	Randomised clinical trial
REZ	Root entry zone
RF	Radiofrequency
RL	Right-left
ROC	Receiver operating characteristic
s	Seconds
SD	Standard deviation
SENSE	Sensitivity encoding
SM	Spetzler-Martin
SNR	Signal-to-noise ratio
SPGR	Spoiled gradient recovery
SPSS	Statistical package for the social sciences
SRS	Stereotactic radiosurgery
SSC	Superior semicircular canals

STAR	Signal targeting with alternating radiofrequency
Sup	Superior
T	Tesla
te-pCASL	Time-encoded pseudo-continuous ASL
TERMA	Total energy released per unit mass
TFE	Turbo field echo
tMRAv	AVM volume obtained with triple-MRA
TMR 10	Tissue maximum ratio 10
TN	Trigeminal neuralgia
TOF	Time-of-flight
TONE	Tilt-optimized non-saturated excitation
TRAK	Time-resolved MRA with keyhole
TR-CE-MRA	Time-resolved contrast-enhanced MRA
TRICKS	Time resolved imaging of contrast kinetics
Triple-MRA	Triple magnetic resonance angiography
TWIST	Time-resolved MRA with interleaved stochastic trajectories
TS	Thomas Solbach
TV	Target volume
VIPR	Vastly under-sampled isotropic projection
VS	Vestibular schwannoma
vs.	Versus
WBRT	Whole brain radiotherapy
y	Year

2D	2 dimensional
3D	3 dimensional
4D	4 dimensional
95%CI	95% confidence interval

List of tables

Table 1.1. Koos neuro-topographic grading system 44

Table 1.2. Barrow Neurological Institute (BNI) pain intensity score for trigeminal neuralgia..... 50

Table 1.3. Spetzler-Martin grading scale..... 52

Table 2.1. Characteristics of the cerebral angiography technique which could potentially be used for AVM targeting. 57

Table 3.1. Demographic and diagnosis details of the study subjects..... 68

Table 3.2. GKR plans calculated with different dose calculation algorithms and head shape approximation method..... 74

Table 3.3. Change in beam-on-time between treatment plans calculated with different head shape approximation methods and dose calculation algorithms. 76

Table 3.4. Relative difference in beam-on-time between the TMR 10 and convolution algorithm per diagnosis..... 78

Table 3.5. Difference in dose to organs at risk between the TMR 10 and convolution algorithm. 79

Table 3.6. Effect of the stereotactic frame on the convolution algorithm 80

Table 3.7. Dosimetric differences between the TMR 10 and convolution algorithm for GKR per diagnosis 82

Table 4.1. Demographic details and diagnoses of the study subjects. 91

Table 4.2. Fiducial error in stereotactic definition of MRI and CT scans for the main study group.....96

Table 4.3. Intra-observer and inter-observer variability of the measurements 97

Table 4.4. Distance (mm) between the location of the landmarks in the MRI and CT scans..... 99

Table 5.1. Demographic details and AVM characteristics of the study subjects 119

Table 5.2. Triple-MRA scanning parameters 123

Table 5.3. AVM target volumes obtained using the standard DSA method and triple-MRA..... 130

Table 6.1. Demographic details and AVM characteristics of the study subjects 153

Table 6.2. Scanning parameters of triple-MRA sequences..... 155

Table 6.3. Confirmation of obliteration with triple-MRA and DSA following GKR of brain AVMs..... 160

Table 6.4. Characterisation of residual AVMs using triple-MRA compared to DSA 163

List of figures

Figure 2.1. The Gamma Knife Perfexion..... 39

Figure 2.2. Leksell stereotactic coordinate frame G..... 40

Figure 2.3. Gamma Knife Radiosurgery for brain tumours..... 46

Figure 2.4. GKR treatment plan for trigeminal neuralgia..... 50

Figure 2.5. Right cerebellar AVM treated with GKR..... 53

Figure 2.6. Catheter-based cerebral angiography using Digital Subtraction Angiography (DSA)..... 55

Figure 2.7. Time-Of-Flight effect. 58

Figure 2.8. Diagram of the accelerated CENTRA Keyhole acquisition method for time resolved CE-MRA mechanism. 60

Figure 2.9. 4DASL angiography labelling and sequence diagram. 63

Figure 3.1. Head shape approximation methods..... 70

Figure 3.2. CT artefact from titanium fixation pin introducing significant error to the convolution calculation..... 75

Figure 4.1. Landmarks used for frame stability evaluation 93

Figure 4.2. Fiducial indicator box accidentally misplaced at post-GKR CT scan 96

Figure 4.3. Difference between the MRI and CT coordinate measurements versus frame-on time in the study group for each of the landmarks analysed..... 100

Figure 4.4. Distribution of the distance (mm) between the location of the landmarks in the MRI and CT scans for the negative controls and the main study group..... 102

Figure 4.5. Discrepancy between MRI and CT imaging planes causing overestimation of the difference seen in the outliers (case 33)..... 105

Figure 4.6. Submillimetre discrepancies between the location of the landmarks in the MRI and CT scans attributed to imaging distortion..... 108

Figure 5.1. Research pathway and image analysis framework used for target delineation with DSA and triple-MRA. 118

Figure 5.2. Representative example of the ASL survey developed to individualise timing of ASL-MRA. 122

Figure 5.3. Imaging used for AVM delineation with the standard DSA based method and triple-MRA 126

Figure 5.4. Bland-Altman plot of the difference between DSA and triple-MRA volumes 131

Figure 5.5. DSA and triple-MRA volumes in the case with the lowest DI and CcI. 133

Figure 5.6. Case 10, in which triple-MRA volume was larger than DSA volume. 134

Figure 5.7. CE-MRA and DSA in a study subject with brain AVM. 139

Figure 5.8. ASL-MRA and DSA in a patient with a brain AVM 140

Figure 6.1. Representative example of DSA and triple-MRA datasets presented to the independent observers for review in a case with complete AVM obliteration 157

Figure 6.2. Diagnostic accuracy (ROC curve) of triple-MRA and individual MRA sequences for confirmation of AVM obliteration following GKR..... 159

Figure 6.3. Representative case of confirmation of AVM obliteration using triple-MRA. 162

Figure 6.4. Combined use of three MRA sequences for identification and characterisation of residual AVMs in two representative cases 165

Figure 6.5. Observer's level of confidence on the assessment of triple-MRA and DSA regarding the absence/presence of a residual AVM 166

Figure 6.6. Identification of residual AV shunt using ASL-MRA and CE-MRA in two cases with residual AVMs after GKR..... 171

Publications

Rojas-Villabona, A., Kitchen, N. & Paddick, I. (2016a) Investigation of dosimetric differences between the TMR 10 and convolution algorithm for Gamma Knife stereotactic radiosurgery. *J Appl Clin Med Phys*, 17(6), 6347.

Rojas-Villabona, A., Miszkiel, K., Kitchen, N., Jäger, R. & Paddick, I. (2016b) Evaluation of the stability of the stereotactic Leksell Frame G in Gamma Knife radiosurgery. *J Appl Clin Med Phys*, 17(3), 5944.

Rojas-Villabona, A., Sokolska, M., Solbach, T., Grieve, J., Rega, M., Torrealdea, F., Benedetta Pizzini, F., Suzuki, Y., Van Osch, M., De Vita, E., Biondetti, E., Shmueli, K., Atkinson, D., Murphy, M., Paddick, I., Golay, X., Kitchen, N. & Jager, R. (2017) Can Gamma Knife Radiosurgery for brain arteriovenous malformations be planned on triple Magnetic Resonance Angiography (triple-MRA)?. *Under peer review for publication.*

Rojas Villabona, A., Benedetta Pizzini, F., Solbach, T., Sokolska, M., Ricciardi, G., Lemonis, C., De Vita, E., Suzuki, Y., Van Osch, M., Foroni, R., Montemezzi, S., Atkinson, D., Ciceri, E., Kitchen, N., Nicolato, A., Golay, X. & Jager, R. (2017) Triple Magnetic Resonance Angiography (Triple-MRA) for Confirmation of Obliteration Following Gamma Knife Radiosurgery for Arterial-Venous Malformations of the Brain. *Under peer review for publication.*

Presentations

Rojas-Villabona, A., Sokolska, M., De Vita, E., Murphy, M., Solbach, T., Grieve, J., Rangi, P., Suzuki, Y., Van Osch, M., Atkinson, D., Biondetti, E., Shmueli, K., Golay, X., Paddick, I., Kitchen, N. & Jager, R. **Triple Magnetic Resonance Angiography (Triple-MRA) for Planning of Gamma Knife Radiosurgery of Brain Arteriovenous Malformations**. *Poster presentation.* 25th annual meeting of the International Society for Magnetic Resonance in Medicine (ISMRM). 22-27 April 2017. Honolulu, Hawaii, USA

Rojas Villabona, A., Benedetta Pizzini, F., Solbach, T., Ricciardi, G., Sokolska, M., Lemonis, C., De Vita, E., Suzuki, Y., Van Osch, M., Foroni, R., Montemezzi, S., Atkinson, D., Longhi, M., Ciceri, E., Kitchen, N., Nicolato, A., Golay, X. & Jager, R. **Triple Magnetic Resonance Angiography (Triple-MRA) for Confirmation of Obliteration Following Gamma Knife Radiosurgery for Arterial-Venous Malformations of the Brain.** *Poster presentation.* 25th annual meeting of the International Society for Magnetic Resonance in Medicine (ISMRM). 22-27 April 2017. Honolulu, Hawaii, USA

Rojas-Villabona, A., Benedetta-Pizzini, F., Ricciardi, G., Sokolska, M., De-Vita, E., Lemonis, C., Suzuki, Y., JP Van Osch, M., Atkinson, D., Boscolo-Galazzo, I., Rangi, P., Foroni, R., Longhi, M., Kitchen, N., Nicolato, A., Golay, X., Jäger, HR. **Triple Magnetic Resonance Angiography (tMRA) for confirmation of obliteration following Gamma Knife radiosurgery for arteriovenous malformations of the brain**. *Oral plenary presentation.* 18th International

Leksell Gamma Knife Society (LGKS) meeting. 15-19 May 2016. Amsterdam, The Netherlands

Rojas-Villabona, A., Sokolska, M., De-Vita, E., Suzuki, Y., JP Van Osch, M., Atkinson, D., Rangi, P., Kitchen, N., Golay, X., Jäger, HR. **Triple Magnetic Resonance Angiography (tMRA) for planning of stereotactic radiosurgery for brain arteriovenous malformations**. *Invited oral presentation*. 6th International Conference of the Novalis Circle. 19 February 2016. Munich, Germany

Rojas-Villabona, A., Miszkiel, K., Kitchen, N., Jäger, HR., Paddick, I. **Evaluation of the stability of the stereotactic Leksell G frame in Gamma Knife Radiosurgery.** *Oral presentation.* 12th International Stereotactic Radiosurgery Society (ISRS) Congress. 7-11 June 2015. Yokohama, Japan

Rojas-Villabona, A., Miszkiel, K., Kitchen, N., Jäger, R., Paddick, I. **A dosimetric comparison of head contouring using the skull scaling instrument method and CT outlining for Gamma Knife Radiosurgery**. *Oral presentation*. 12th International Stereotactic Radiosurgery Society (ISRS) Congress. 7-11 June 2015. Yokohama, Japan

Rojas-Villabona, A., Miszkiel, K., Kitchen, N., Jäger, R., Paddick, I. **Evaluation of the stability of the stereotactic Leksell G frame in Gamma Knife Radiosurgery.** *Oral presentation.* Society of British Neurological Surgeons Spring meeting. 22-24 April 2015. Southampton, UK

1. Introduction

The technical development of Gamma Knife Radiosurgery (GKR) started in the 1950s and it flourished in the 1980s, with the introduction of Computed Tomography (CT) and Magnetic Resonance (MR) imaging (Leksell, 1951; Leksell & Jernberg, 1980). GKR has significantly contributed to the shift towards less invasive management of neurosurgical pathologies over the last few decades (Koga et al, 2010).

The safety and efficacy of GKR has been steadily demonstrated by cumulative numbers of studies -mainly outcome reports- and a variety of intracranial conditions including brain tumours, vascular malformations and functional pathologies are now routinely treated using the Gamma Knife (Mansouri et al, 2015a; Nagy et al, 2012). The indications for GKR continue to expand, with an increasing interest in functional and staged radiosurgery while the volume of patients receiving GKR also grows. More than a million patients have been treated with the Gamma Knife to date and there are over 300 Gamma Knife centres operating in 45 countries around the world (Leksell Gamma Knife Society, 2016). The Gamma Knife Centre at Queen Square started operations in October 2013 and since its opening a series of technical and clinical challenges have been encountered. These challenges, common to most contemporary Gamma Knife centres, are the main focus of this dissertation.

GKR is, for radiation oncology standards, a relatively aggressive treatment with doses about ten times that of standard radiotherapy. At the same time, it is a less invasive treatment modality for intracranial pathologies that would otherwise be

managed surgically. For these reasons, it continues to be closely scrutinised by both the radiation oncology and neurosurgery communities. GKR has been compared to other treatment modalities and radiosurgical techniques and its limitations have been readily identified (Park et al, 2016). It has been criticised for failing to correct treatment dose for tissue heterogeneity and for using instead a simpler algorithm, Tissue Maximum Ratio 10 (TMR 10), to predict the distribution of ionizing radiation in the brain. TMR 10 assumes the patient's head is of an even density, equivalent to water (Nakazawa et al, 2014b). This results in a significant approximation of the dose delivered by the Gamma Knife and for this reason a new dose calculation algorithm (convolution) capable of performing heterogeneity corrections has been developed and released by the manufacturer (Elekta, 2011b). The dosimetric differences between TMR 10 and convolution algorithms need to be better understood before the new method can be deployed in a clinical setting. However, both methods are available in GKR planning system and the choice of which algorithm to use, together with appropriate dose adjustments, are at the discretion of the radiosurgery practitioner. This issue is addressed in **chapter 3** by investigating how GKR dose calculations vary when using the new convolution algorithm compared with the established TMR 10 algorithm.

Radiosurgery has recently seen an accelerated development of frameless radiosurgical techniques which are thought to deliver submillimetre accuracy without the discomfort of a solid frame fitting procedure (Schlesinger et al, 2012). In addition, the latest enhancement of the Gamma Knife itself, the Icon, incorporates a stereotactic cone beam CT and real-time motion management to enable frameless immobilization (Ruschin et al, 2013). However, most data on the safety and efficacy of stereotactic radiosurgery comes from GKR and probably around 99% of all GKR procedures have been performed using the stereotactic Leksell frame G (Lunsford et al, 2013). The Leksell frame is therefore considered to be the gold standard stereotactic immobilization method and its accuracy and stability will serve as a reference to assess performance of new frameless technologies. For this reason, we have investigated the stability of the Leksell frame by evaluating the possibility that the actual location of a target within the

stereotactic system at treatment differs from its calculated location, due to displacement of the reference frame between initial stereotactic imaging and the end of the stereotactic procedure. This data, presented in **chapter 4**, will be valuable for future evaluation and development of frameless radiosurgery systems.

The publication of the ARUBA trial (A randomized trial for un-ruptured Brain arteriovenous malformations) in 2014 changed the clinical management of un-ruptured arteriovenous malformations (AVM) and a less invasive approach is now favoured (Mohr et al, 2014). The ARUBA trial concluded that medical management alone is superior to medical management with interventional therapy (microsurgery, embolization and/or radiosurgery) for the prevention of death or stroke in patients with un-ruptured brain AVMs followed up for 33 months. The methodology and external validity of this trial has been extensively questioned and its applicability to our field is greatly undermined by the poor representation of radiosurgery -only 31 patients- and the lack of subgroup outcome data (Bambakidis et al, 2014). Nonetheless, the ARUBA trial has raised awareness of the invasiveness of treatments used for AVMs and has reinforced the imperative for these interventions to be made less invasive, where possible. In radiosurgery, this can be achieved by optimising the planning method which is currently based on digital subtraction angiography (DSA), an invasive procedure that carries a non-negligible risk of complication (Kaufmann et al, 2007). We proposed that a combination of three advanced MR angiography (MRA) sequences could be successfully used as an alternative to DSA for the planning of GKR (**chapter 5).** The MRA sequences selected and optimised for this study are 4D arterial spin labelling based MR angiography (ASL-MRA), time-resolved contrast-enhanced MRA (CE-MRA) and high definition time-of-flight angiography (HD-TOF), and they are collectively referred to as triple-MRA.

A parallel study was also carried out to apply the same principle of less invasive AVM imaging with a combination of MRA sequences at the post-GKR stage, when a DSA is routinely performed to confirm AVM obliteration (**chapter 6)**. This study aimed to evaluate whether triple-MRA can be used as an alternative to

DSA to confirm AVM obliteration following GKR and to characterise residual AVMs in case of incomplete response. This is clinically relevant because triple-MRA can not only avoid unnecessary DSA examinations for patients with cured AVMs, but it can also help rationalize its use in patients with residual AVMs, who may need further treatments.

The studies presented in this dissertation have been motivated by distinct challenges of radiosurgery practice at Queen Square. The evaluation of the convolution algorithm, for instance, was performed to inform our GKR practitioners on dosimetry algorithm selection. The use of triple-MRA for GKR planning has the potential to reduce the invasiveness of AVM radiosurgery treatment. The methodology used to address these challenges was purposefully planned and the research procedures prospectively conducted to ensure the external validity of the results, which are better understood within the context of a rapidly evolving and changing discipline.

2. Literature review

2.1 Gamma Knife Radiosurgery

GKR is a well-established radiation based treatment for benign and malignant tumours, vascular malformations and functional disorders of the brain (Koga et al, 2010). The Gamma Knife Stereotactic Radiosurgery (SRS) technique, as developed by Lars Leksell in the 1950's and subsequently used in most Gamma Knife peer reviewed publications, involves the stereotactic delivery of a high dose of radiation to a well-defined intracranial target in a single session using a rigid skull immobilisation system (Leksell, 1968; Lipski et al, 2015).

The energy delivered using the Gamma Knife is expected to inactivate all cells contained within the radiosurgical target while preserving the normal surrounding tissue (Lippitz et al, 2014). This makes GKR fundamentally different to standard radiotherapy in which the more radio-sensitive tumour cells are selectively inactivated while minimal or tolerable exposure and damage is caused to normal cells within the treatment volume (Patel & Mehta, 2007). This is achieved in standard radiotherapy by dose fractionation which exploits the increased repair capacity of normal cells and creates a therapeutic window which enables the use of standard radiotherapy (Bentzen, 2006). In GKR, however, the high dose delivered elicits a necrotizing effect and tissue preservation within the target is not expected. Preservation of the surrounding structures, in the other hand, is accomplished by a steep dose gradient outside the radiosurgical target and this is one of the key factors that make radiosurgery feasible (Paddick & Lippitz, 2006).

The principle of radiosurgery has been extended to treatment of extracranial conditions and it has been greatly diversified with the development of a variety of systems and techniques capable of safely delivering high doses of ionizing radiation to well defined targets. This is reflected by the most recent definition of SRS by the American Association of Neurological Surgeons (AANS), the Congress of Neurological Surgeons (CNS), and the American Society for Therapeutic Radiology and Oncology (ASTRO), which states: "SRS is a distinct discipline that utilizes externally generated ionizing radiation in certain cases to inactivate or eradicate defined target(s) in the head and spine without the need to make an incision. The target is defined by high-resolution stereotactic imaging. SRS is typically performed in a single session, using a rigidly attached stereotactic guiding device, other immobilization technology and/or a stereotactic image-guidance system, but can be performed in a limited number of sessions, up to a maximum of five. Technologies that are used to perform SRS include linear accelerators, particle beam accelerators, and multisource Cobalt 60 units. In order to enhance precision, various devices may incorporate robotics and real time imaging" (Barnett et al, 2007).

2.2 History of Gamma Knife Radiosurgery

The term and concept of stereotactic radio-surgery were first described by Lars Leksell in 1951 (Leksell, 1951). This pioneering work, carried out in partnership with Börje Larsson, combined a stereotactic guiding device with a radio-therapeutic modality, initially proton beams and linear accelerators which were soon abandoned in favour of the more practical and efficient cobalt-60 sources (Larsson et al, 1958). The first prototype of a Gamma Knife device using 179 Co^{60} sources was developed by Leksell and Larsson at the Karolinska institute in Sweden and first used to treat a patient in 1967 (Leksell, 1968).

The use of the Gamma Knife in the early days was limited to pathologies that could be targeted with the imaging methods available at the time; such as trigeminal neuralgia in which the Gasser ganglion can be located using plain X

rays (Leksell, 1971). Probably for this reason, the second Gamma Knife unit in Stockholm was specially re-designed to treat AVMs, which could be well depicted at the time using DSA (Steiner et al, 1972). Early work in functional radiosurgery in the 1970's included thalamotomies for intractable pain and capsulotomies for psychiatric disorders (Leksell & Backlund, 1978; Leksell et al, 1972) but it was only in the 1980's when the introduction of CT and MR imaging enabled the safe and successful application of GKR to a prolific variety of intracranial conditions (Hounsfield, 1976; Leksell et al, 1985a; Leksell & Jernberg, 1980; Leksell et al, 1985b). The 1980's also saw the installation of a third unit (first out of Sweden) in Buenos Aires, Argentina and the commissioning of the fourth GKR unit in Sheffield, United Kingdom in the summer of 1985 (Walton et al, 1987). The fifth Gamma Knife in the world, and first in the United States, became operational in the University of Pittsburgh in 1987 (Lunsford et al, 1989). More than one million GKR procedures have been performed around the world since then (Berkowitz et al, 2013).

2.3 The Gamma Knife Perfexion

The Perfexion Gamma Knife was released in 2006 as an entirely redesigned radiosurgery unit that differed fundamentally from previous models of the Leksell Gamma Knife. It did not only incorporate a new fully automated collimator arrangement and patient positioning system but also software developments were included to improve the ability to create complex shapes of isodose volumes. The Gamma Knife Perfexion was used for all research activities presented in this thesis.

It incorporates 192 Co^{60} sources distributed in 8 sectors cylindrically arranged. Each sector comprises 24 sources distributed in five rows that when aligned with the adjacent sectors form five rings of beams as shown in Figure 2.1 (Lindquist & Paddick, 2007). The radiation beams are shaped using cylindrical 120 mm long tungsten tubes (collimators) built into a collimator body. Three collimator sizes are incorporated, 4, 8 and 16 mm and an automated drive system slides each

sector back and forth enabling selective exposure of the collimators of the selected size to the sources (Figure 2.1c). A sector can also be positioned between two rows of collimators and this enables blocking of individual sectors during treatment (Petti et al, 2008). The collimated beams are converged with high accuracy to a fixed isocentre where the target is positioned during treatment using a skull immobilisation system and a fully automated patient positioning system (Novotny et al, 2014).

2.4 Leksell stereotactic frame G

The safety and efficacy of GKR relies on the high precision of its image-guided targeting system. The use of a stereotactic frame tightly attached to the skull is still considered the most accurate technique for beam delivery inside the head (Rojas-Villabona et al, 2016b). The Leksell stereotactic coordinate frame is a dedicated stereotactic tool introduced by the Swedish Neurosurgeon Lars Leksell in the 1970s and further developed over the last few decades (Leksell & Jernberg, 1980). It was extensively used as a stereotactic tool for brain biopsies before neuro-navigation systems were developed and it is still used for GKR and insertion of deep brain stimulation electrodes (Simon et al, 2005).

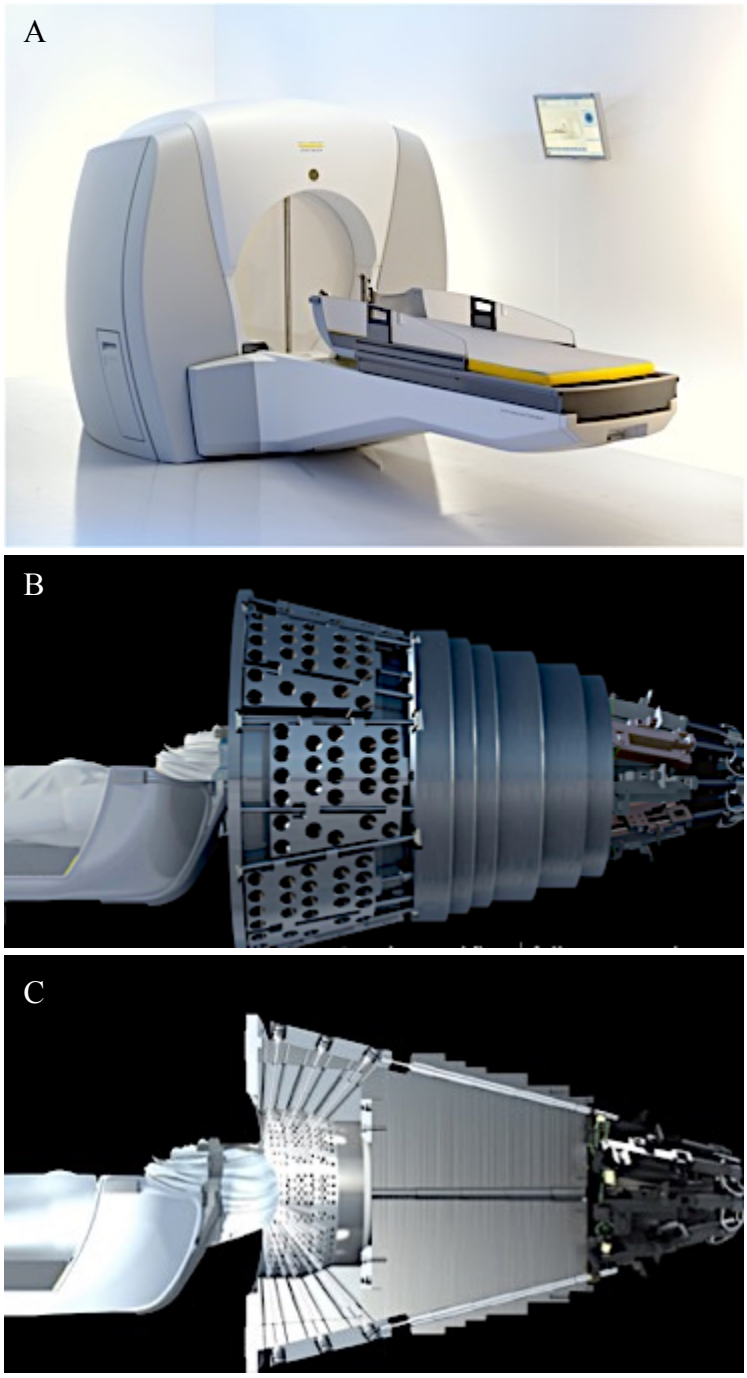

Figure 2.1. The Gamma Knife Perfexion. (A) The Gamma Knife perfexion incorporates 192 Co^{60} sources distributed in 8 sectors cylindrically arranged. Each sector comprises 24 sources distributed in five rows that when aligned with the adjacent sectors form five rings of beams (B). Three collimator sizes are incorporated (4, 8 and 16 mm) and an automated drive system slides each sector back and forth enabling selective positioning of that group of sources on the collimators of the desired size (C).
https://www.elekta.com/radiosurgery/leksell-gamma-knife-perfexion.html

The most recent version of the Leksell frame is the model G which is made of titanium-aluminium alloy. The dimensions of the rectangular frame base are 190 x 210 mm, and a straight or curved front piece can be used anteriorly. Four vertical posts and titanium pins are used to secure the frame to the outer layer of the skull and a system of fiducial markers attached to the frame during imaging enables the accurate definition of scans into a computerised stereotactic coordinate system. The coordinates of the frame centre are 100, 100, 100, and a hypothetical frame origin, i.e., x, y and z = 0, is located in the right upper posterior corner of the frame. For GKR, virtually any target located above the upper border of the frame base (z =167) can be treated and long posts are available to enable coverage of lesions located as low as the upper cervical spine (C2). Figure 2.2 shows the assembled Leksell frame G as it is used for GKR at QSRC.

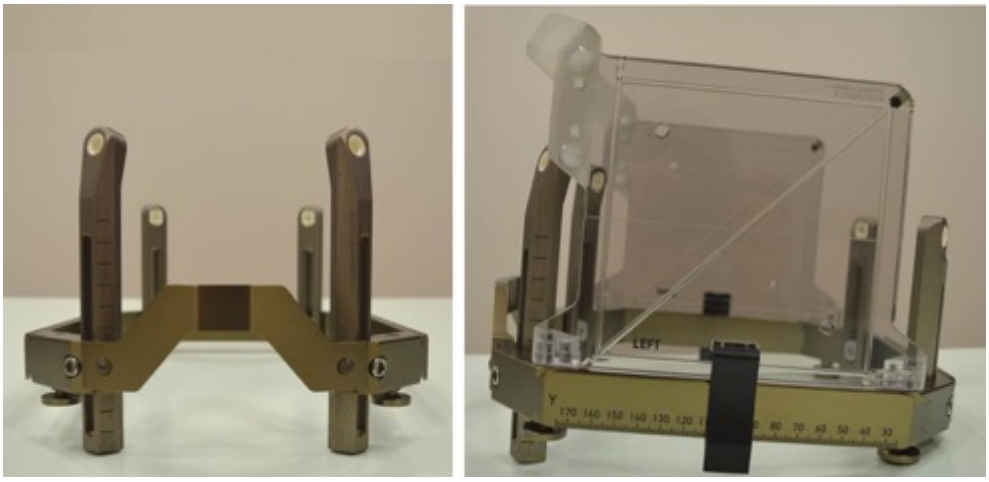

Figure 2.2. Leksell stereotactic coordinate frame G. Left: Frame assembled with the curved front piece in the upwards position, angled anterior insulated posts and medium straight insulated posts posteriorly. Right: Lateral view of the Leksell G frame with the MRI fiducial indicator box attached.

2.5 Gamma Knife dosimetry

A typical radiosurgery treatment plan is made of a number of exposures, called isocenters or shots, directed to different areas of the target to conformaly cover a pre-defined target volume (TV). Once the location of the shots has been specified in the coordinate system, a treatment dose and prescription isodose (PI) are selected based on pathology (Table 3.7), target size, location, previous treatments and surrounding organs at risk (Lippitz et al, 2014). The final treatment plan is made of the stereotactic coordinates and length of exposure (Beam-on-time) of a number of shots with their specified collimator size arrangement.

Shots can be planned with a combination of collimator sizes (hybrid) and this feature allows each individual isocentre of a treatment plan to have its own optimized shape, thereby, increasing the overall matching between the volume of the prescription isodose (PIV) and the TV. This concept of how well the PIV conforms to the TV is known as conformity and a number of parameters have been described to assess treatment plans in this regard (Lindquist & Paddick, 2007). The most basic of these is coverage, which is the percentage of TV that is included or covered by the PIV. More complex indices have also been developed to describe agreement between the TV and PIV. They include the prescription isodose to target volume ratio (PITV), defined by Shaw et al and also known as conformity index, and the new conformity index described by Paddick et al (Paddick & Lippitz, 2006; Shaw et al, 1993). They are calculated using the following equations:

$$PITV\ (Conformity\ index) = \frac{PIV}{TV} \tag{2.1}$$

$$Paddick's\ new\ conformity\ index = \frac{{TV_{PIV}}^2}{TV \times PIV} \tag{2.2}$$

where TV_{PIV} is the volume of the target encompassed by the PIV. An ideal PITV is 1, or slightly higher, and a score of less than unity suggests a lack of target

coverage. Paddick's conformity index is between 0 and 1, with the highest score representing the most conformal plan (Paddick & Motti, 2013)

As a consequence of the number, locations and respective weights of multiple isocenters used, a high degree of heterogeneity inside the target volume and a very steep dose falloff outside the target volume is created. The latter, enables maximal exposure within the target with minimal damage to surrounding structures and is one of the factors that makes radiosurgery possible (Massager et al, 2006). Therefore, dose distribution outside the target, is as important as conformity in the assessment of planning quality. The most basic metric describing dose fall-off outside the target is selectivity which is the percentage of PIV included in the TV. Ideally all PIV should be inside the TV which results in 100% selectivity. The Gamma Knife planning software also enables the calculation of dose volume histograms that describe dose distribution inside and outside TV, PIV and defined organs at risk. A gradient Index has also been described to objectively measure dose falloff outside the target (Paddick & Lippitz, 2006). It is the ratio of the volume of half the prescription isodose volume ($PIV_{1/2}$) to the volume of the prescription isodose (PIV):

$$Gradient\ Index = \frac{PIV_{1/2}}{PIV} \tag{2.3}$$

2.5 Clinical Applications of Gamma Knife Radiosurgery

A variety of intracranial conditions including brain tumours, vascular malformations and functional pathologies are now routinely treated using the Gamma Knife (Mansouri et al, 2015a; Nagy et al, 2012). The worldwide estimates of treatment by indication, as reported by the International Leksell Gamma Knife Society (LGKS) between 1968 and 2016, shows malignant tumours as the most common indication (44.2%) followed by benign tumours (36.8%), vascular (11.3%) and functional disorders (7.3%) (Leksell Gamma Knife Society, 2016). This varies between countries and between GKR centres. At Queen Square, benign tumours (i.e., vestibular shwannoma and meningioma) are the most

frequent indication (48%) followed by vascular malformations, namely AVMs (19.5%). Malignant pathology (i.e., brain metastases) is our third most common indication (18%) followed by functional disorders, mainly trigeminal neuralgia in 8% of the cases (unpublished data). This pathology distribution is reflected on the subjects recruited for our studies (Table 3.1) and for this reason the literature review focuses on the five most common pathologies treated at QSRC which comprises more than 93% of our practice.

2.5.1 Vestibular schwannoma

Vestibular schwannomas (VS), also called acoustic neuromas, are benign intracranial neoplasms arising from the Schwann cells that myelinate the vestibular portion of the eighth cranial nerve (Bari et al, 2002). Data from histopathological studies have demonstrated an overall VS incidence of 0.57 to 2.7% but the clinical incidence is considered to be 10 per-million per-year (Yoshimoto, 2005). Hearing loss is the most common presenting complaint affecting 95% of patients and this is followed in frequency by tinnitus, vertigo, dizziness and less often hydrocephalus (Matthies & Samii, 1997).

VS can be classified by size and neurotopographic features using the Koos grading system as shown in Table 1.1 (Koos et al, 1998). It describes a predictable growth process from small intra-canalicular lesions to larger tumours that occupy the cerebello-pontine cistern and eventually displace the brainstem. As part of their natural history, between 29 and 54% of these tumours continue to grow if left untreated and 37 – 46% loose functional hearing following diagnosis (Arthurs et al, 2011; Yoshimoto, 2005). However, only around 20% of them do require active treatment and for this reason, conservative management with regular imaging surveillance has traditionally been advocated as the appropriate first line treatment for newly diagnosed -small to moderate size- vestibular schwannomas.

Microsurgery, using either a translabyrinthine or retrosigmoid approach, is the traditional treatment with approximately 1% of the cases requiring additional treatment. It has, however, a poorer hearing preservation rate and between 14 and

29% of patients experience permanent facial neuropathy. For this reason it is reserved for larger tumours, i.e., > 30 mm in diameter (Arthurs et al, 2011).

SRS is an increasingly popular intervention for VS which results in arrest of tumour growth in 91 – 95% of treated cases with 1.6% to 4.2% of the cases needing additional treatment after SRS (Myrseth et al, 2007). Comparative studies have repeatedly demonstrated that GKR provides the best outcome in terms of tumour control and functional preservation for enlarging intra-canalicular VS (Koos I) and those protruding into the cerebellopontine angle (Koos II), compared to conservative management and surgical excision (Lipski et al, 2015). Several reports also demonstrate the successful application of GKR to larger VS with satisfactory control rates and minimal complications (Chung et al, 2010).

Most evidence on safety and efficacy of SRS for VS comes from GKR with a treatment dose between 11 and 13 Gy delivered to the tumour margin in a single session (Figure 2.3). Hearing preservation with this method ranges from 44 to 63%. Permanent facial and trigeminal neuropathy occur in less than 10% and 11 - 16% of the cases, respectively (Yamakami et al, 2003).

Table 1.1. Koos neuro-topographic grading system.

Grade	Description
I	Small intra-canalicular tumour
II	Small tumour (<2 cm diameter) protruding into the CP angle
III	Tumour occupying CP cistern with no brainstem displacement
IV	Any tumour displacing the brainstem

CP = Cerebellopontine

2.5.2 Meningioma

Meningiomas are a heterogeneous group of tumours arising from the arachnoid villi in the meninges and they account for more than one third of all central nervous system tumours (Kohler et al, 2011). The vast majority of them are benign, with only 2% classified as anaplastic or malignant (Harrison et al, 2016). There is great heterogeneity in diagnosis, histological type and aggressiveness which warrants individualised treatment selection. Tumour size and location, along with tumour behaviour, are the main factors determining treatment choice.

Complete surgical resection, including dural base and underlying bone, is the first line treatment for benign intracranial meningiomas when achievable (Santacroce et al, 2012). Conservative management with regular imaging surveillance is frequently used for incidental, non-growing or inoperable tumours and the use of radiation based treatments as primary or secondary management has become increasingly important in the multimodality care of patients with meningiomas (Mansouri et al, 2015a).

SRS was initially used for the management of skull base meningiomas which are difficult to resect (Figure 2.3). It has, however, gained acceptance as a first line modality in the management of meningiomas in other locations, due to good tumour control rates in the long term and low side-effects (Sheehan et al, 2010). Tumour control rates with GKR vary between 86% to 97% for small to medium size meningiomas (< 3.5 cm diameter) in case series with long-term follow-up (Mansouri et al, 2015b; Santacroce et al, 2012; Sheehan et al, 2010). Adjuvant SRS after subtotal excision of intracranial meningiomas has also been demonstrated to improve progression-free survival at 15 years compared to subtotal excision alone (87% vs. 30% at 15 years, respectively) (Condra et al, 1997).

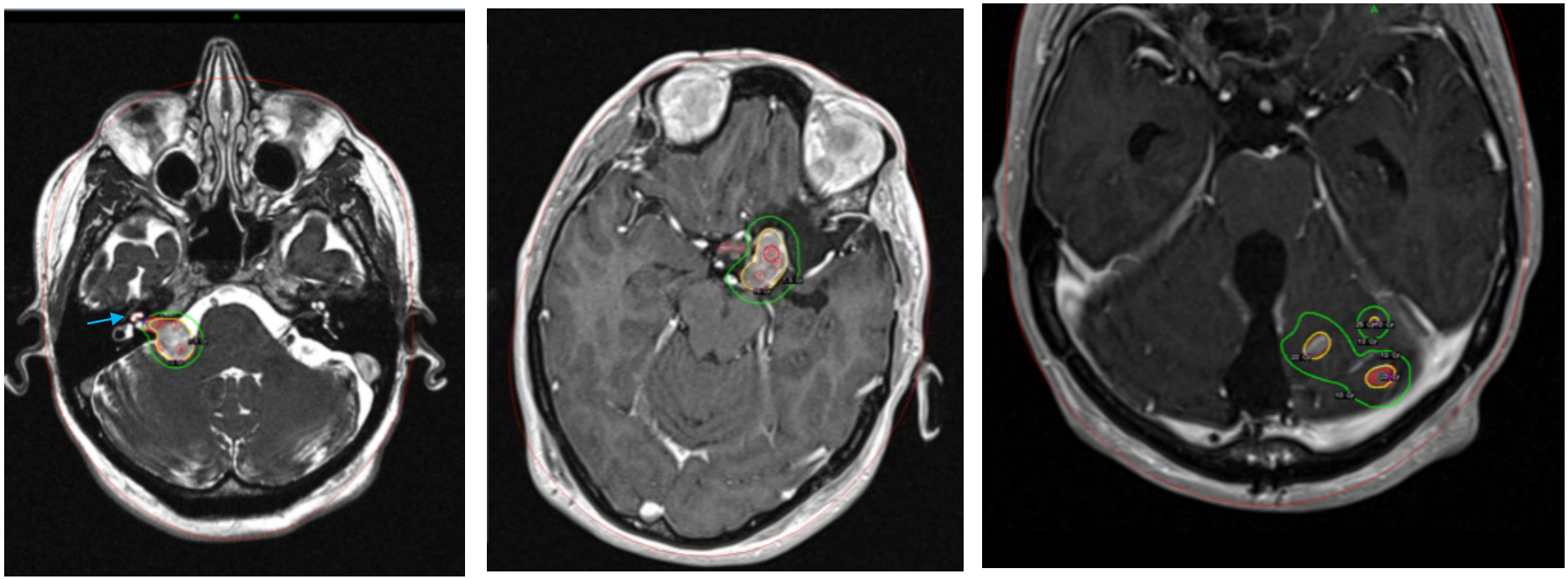

Figure 2.3. Gamma Knife Radiosurgery for brain tumours. *Left:* Representative GKR treatment plan of a right sided vestibular schwannoma compressing the brainstem. This T2 weighted MR sequence enables identification of the adjacent cochlea (blue arrow) which is considered the critical structure to protect for hearing preservation. *Middle:* GKR is the treatment of choice for this residual skull base meningioma due to its proximity to the optic pathways (delineated in red) and several critical vascular structures. *Right:* GKR treatment plan of three metastatic lesions in the posterior fossa in a patient who has undergone surgical resection of a larger lesion in the close proximity.

2.5.4 Brain metastases

Brain metastases (BM) are the most common brain tumours in adults and their estimated incidence is between 4 and 15 cases per 100.000 persons/year (Counsell et al, 1996; Eichler & Loeffler, 2007). The number of cancer patients who develop BM varies across groups from 8 - 40% (Linskey et al, 2010; Schouten et al, 2002). The most common primary tumours in patients with BM are lung cancer (40% – 50%), breast cancer (15% – 25%), and melanoma (5% – 20%) (Karlsson et al, 2009).

The presence of BM denotes high morbidity and extremely poor prognosis with median survival of around 51 days when the lesions are considered inoperable and left untreated (Langley et al, 2013). Management depends on several factors including primary tumour, number of lesions, tumours' location and size, patient´s performance status and the extent, prognosis and treatability of extra cranial disease (Banfill et al, 2012). Patient age and primary tumour control are the most important factors to predict survival of patients with BM (Karlsson et al, 2009).

The cornerstones of treatment are surgery, whole brain radiotherapy (WBRT), chemotherapy and SRS (Figure 2.3). A multidisciplinary approach is favoured with frequently a combination of treatments to prolong survival, preserve neurologic and neurocognitive function, and maximize quality of life (Eichler & Loeffler, 2007).

Surgical resection of BM may benefit selected patients, particularly those with a solitary metastasis causing raised intracranial pressure, where decompression produces rapid symptom relief (Eichler & Loeffler, 2007). WBRT has been used for several decades to treat patients with BM based on non-randomized studies suggesting that WBRT increases the median survival time to 3 – 4 months compared with no treatment (1 month) and corticosteroids alone (2 months) (Zimm et al, 1981). The benefit of WBRT compared to supportive care alone has not been studied in RCT. The Medical Research Council QUARTZ trial, indicated no evidence of benefit on quality of life or overall survival for patients with

inoperable BM from non-small cell lung cancer treated with WBRT and Optimal Supportive Care (OSC) as compared to patients receiving OSC alone (Langley et al, 2013). The most recent Cochrane systematic review on WBRT for treatment of newly diagnosed multiple BM also concluded that WBRT does not provide a significant benefit in terms of OS, neurological function, or symptoms control (Tsao et al, 2012). The long-term neurotoxic effects of WBRT have become a deterrent to its use, particularly on patients with good performance status who are expected to survive significantly longer than the onset time of prominent WBRT-induced neurocognitive decline (Khalsa et al, 2013; Langley et al, 2013). In current clinical practice, WBRT is reserved for patients with multiple BM not amenable to surgery or SRS, poor functional status, or active/disseminated systemic disease for palliation of neurological symptoms. Nevertheless, it has been demonstrated that the number of distant recurrences is higher when WBRT is omitted and this has been used as an argument to use WBRT as an adjuvant to surgery or SRS (Aoyama et al, 2006; Tsao et al, 2012).

SRS is a widely accepted treatment modality for newly diagnosed patients, alone or in combination with WBRT, and as a salvage therapy for progressive intracranial disease after WBRT (Karlsson et al, 2009). Large multicentre series have reported a consistently high local tumour control rate of 80% - 90% following GKR for single and multiple BM which is the most common indication for GKR in the US (Chang et al, 2000; Da Silva et al, 2009; Karlsson et al, 2009; Salvetti et al, 2013). Prospective randomised studies have shown prolonged survival for patients with single brain metastasis treated with SRS plus WBRT compared to WBRT alone (Andrews et al, 2004). SRS offers several advantages over craniotomy and WBRT, such as the treatment of surgically inaccessible lesions in deep-seated or eloquent areas, shorter admissions, and feasibility for physically ill patients with multiple lesions (Figure 2.3). The ARE that occur after GKR are usually mild and include treatment induced oedema (4% – 6%), seizures (2% – 6%) and delayed radiation necrosis (2% – 17%) (Banfill et al, 2012; Breneman et al, 1997). Cognitive dysfunction is rare following SRS (Aoyama et al, 2007); however, SRS does not address distant failure in the brain which occurs in around 30% of the patients following SRS (Hanssens et al, 2011).

2.5.3 Trigeminal Neuralgia

Trigeminal neuralgia (TN) is defined by the International Association for the Study of Pain (IASP) as "sudden, usually unilateral, severe, brief, stabbing, recurrent pain in the distribution of one or more branches of the fifth cranial nerve" (IASP, 1986). In patients with tumours, multiple sclerosis, AVMs or other lesions that affect the trigeminal pathway the condition is considered secondary whereas it is termed idiopathic if no structural abnormalities of this kind are found (Zakrzewska, 2002). In the majority of patients with idiopathic TN, a neurovascular conflict involving the trigeminal nerve is observed in the Root Entry Zone (REZ) as the nerve enters the brain in the skull base, and mounting evidence supports this as a major causative or contributing factor (Nurmikko & Eldridge, 2001; Zakrzewska & Coakham, 2012).

The first line treatment for TN is medical management with antiepileptic and antidepressant agents and this results in adequate pain control in the majority of newly diagnosed cases (Zakrzewska, 2002). For those patients whose pain is not controlled medically, or the side effects of medication are unacceptable, surgical options are available. These can be divided into ablative and non-ablative procedures. The only non-ablative procedure available involves surgical microvascular decompression. It is the most invasive procedure of all but also the most effective in terms of long-term pain relief. Percutaneous ablative procedures such as thermo-coagulation or glycerol injection are also routinely used (Nurmikko & Eldridge, 2001). GKR is an ablative treatment and the National Institute for Health and Clinical Excellence (NICE) has issued guidelines on SRS for TN using the Gamma Knife in the UK (Allsop et al, 2015).

Modern GKR of TN involves the delivery of 80 - 90 Gy to the cisternal portion of the trigeminal nerve using a single 4 mm shot positioned 7 - 8 mm anterior to the REZ as shown in Figure 2.4. The Barrow Neurological Institute (BNI) pain intensity score (Rogers et al, 2000) is extensively used in radiosurgery to assess treatment response (Table 1.2). Several groups have consistently reported adequate pain control (BNI I - III) in 65 - 75% of the patients at 1 year, 60 - 65%

at two years and 40 - 60% at 5 years post GKR (Baschnagel et al, 2014; Dhople et al, 2009; Regis et al, 2006; Rogers et al, 2000; Verheul et al, 2010). Usual time to response is between 2 and 12 weeks and non-bothersome facial numbness, which is reported in up to 25% of the cases, is the commonest side effect (Dhople et al, 2009; Kondziolka et al, 2010).

Table 1.2. Barrow Neurological Institute (BNI) pain intensity score for trigeminal neuralgia.

Score	Description
I	No trigeminal pain, no medication
II	Occasional pain, not requiring medication
IIIa	No pain, pain medication used
IIIb	Some pain adequately controlled with medication
IV	Some pain not adequately controlled with medication
V	Severe pain no relieved with medication

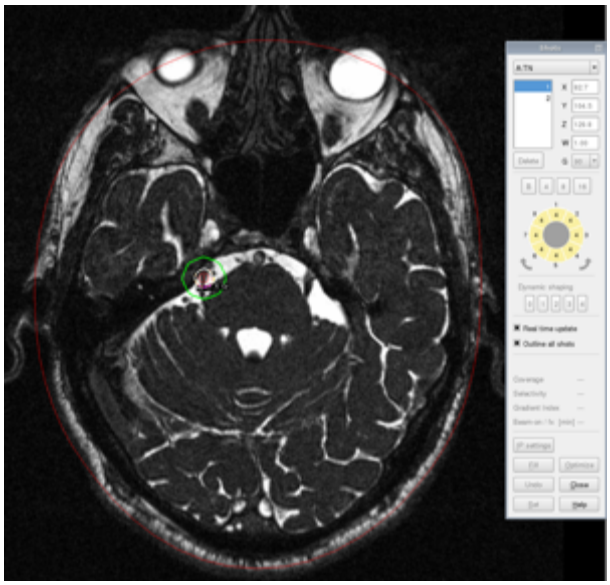

Figure 2.4. GKR treatment plan for trigeminal neuralgia. Single 4 mm shot in the cisternal portion of the trigeminal nerve, 7 - 8 mm anterior to the REZ.

2.5.5 Arteriovenous Malformations

AVMs are congenital vascular abnormalities characterized by anomalous connections between arteries and veins leading to arteriovenous shunting through a network of coiled and tortuous vessels, the so-called nidus, without a normal intervening capillary bed (Hernesniemi et al, 2008). Brain AVMs prevalence varies between 15 and 18 per 100 000 adults (Al-Shahi et al, 2002a). The overall AVM detection rate is 1 per 100 000 adults/ year and they are incidental findings on brain MRI scans in approximately 0.05% of the population (Morris et al, 2009; Stapf et al, 2002). Around half of patients with brain AVMs present with intracranial haemorrhage and this is a potential source of substantial neurological morbidity and mortality (van Beijnum et al, 2011). The annual haemorrhage risk of patients with brain AVMs may be as low as 0.9% per year in cases with un-ruptured, superficially located AVMs with superficial drainage, but may be as high as 34% per year in patients with previously ruptured, deeply seated brain AVMs with deep venous drainage (da Costa et al, 2009; Stapf et al, 2006). Less often patients present with seizures, headaches, bruit or tinnitus and an increasing number of patients are incidentally diagnosed (Hernesniemi et al, 2008)

Currently available treatment options for cerebral AVMs include microsurgery, endovascular embolization and SRS, alone or in combination, and in some cases conservative management with regular imaging surveillance (Rubin et al, 2014). Microsurgery (i.e., craniotomy and excision) has been reported to have a low risk of complications in small AVMs located in non-eloquent and accessible areas and it results in immediate cure when complete resection is achieved (Mohr et al, 2013). Embolization is a less invasive approach used to obliterate small malformations, to make larger AVMs amenable for surgery/radiosurgery, or to eliminate a possible cause of active haemorrhage (e.g. associated aneurysms) (van Beijnum et al, 2011).

Radiosurgery is a well-established non-invasive option for small to medium size compact AVMs. It produces a detectable decrease in blood flow through the AVM a few months after treatment, which gradually progresses so that by two to

three years, approximately 75% of the AVMs are completely obliterated, Figure 2.5 (Koltz et al, 2013).

Large AVMs generally require staged or multimodality treatments and the treatment outcome is dependent on both patient characteristics and AVM location/morphology (van Beijnum et al, 2011). The latter can be systematically assessed using the Spetzler-Martin grade scale (Table 1.3), which is a composite score of nidus size (3cm, 3 - 6cm, > 6cm; 1 - 3 points), eloquence of adjacent brain (1 point if located in brainstem, thalamus, hypothalamus, cerebellar peduncles, or sensorimotor, language, and primary visual cortex), and the presence of deep venous drainage (1 point if any or all drainage is through deep veins, such as internal cerebral veins, basal veins, or pre-central cerebellar veins) (Spetzler & Martin, 1986). GKR has been extensively used for brain AVMs and, except for timing of obliteration, the outcome for patients with AVMs Spetzler-Martin grade I to III appears to be comparable to surgical outcomes reported on similar grade cohorts (Koltz et al, 2013). GKR is the treatment of choice when surgical risks are thought to be excessive and complete obliteration is not expected or achievable with endovascular treatment (Koltz et al, 2013).

Table 1.3. Spetzler-Martin grading scale.

Parameter		Score
Size	< 3 cm	1
	3 - 6 cm	2
	> 6 cm	3
Eloquence	Non-eloquent	0
	Eloquent	1
Drainage	Superficial only	0
	Deep	1
AVM total score		1 - 5

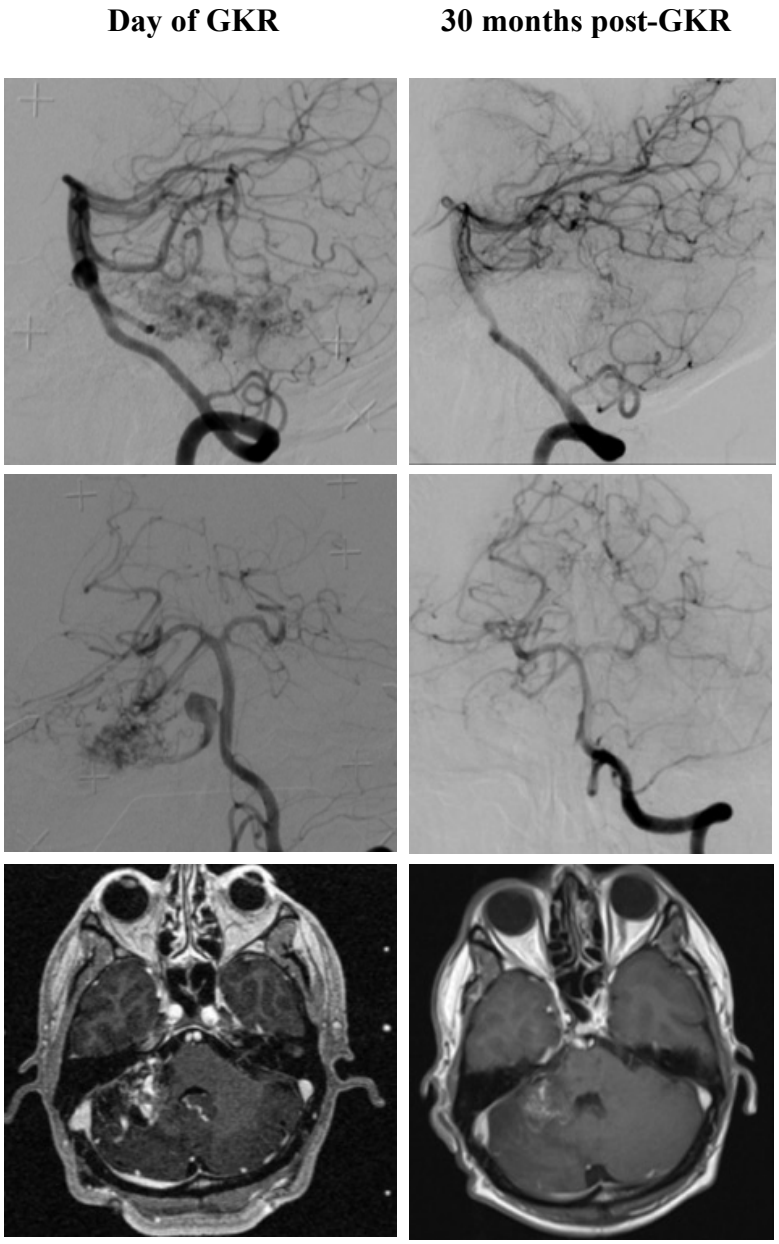

Figure 2.5. Right cerebellar AVM treated with GKR. Left: DSA and MRI (bottom) performed on the day of GKR showed a sizeable right side cerebellar AVM which was treated with GKR. Right: MRI scan (bottom) of the same patient 30 months after GKR shows reduction of size of the treated vascular abnormality and DSA (top) confirmed treatment response.

Interventional treatment of ruptured AVMs is advisable and the aim of treatment is to completely resect/obliterate the lesion to minimize the risk of new bleeding (van Beijnum et al, 2011). The recently published ARUBA trial suggested that medical management alone is superior to medical management with interventional therapy (either surgery, embolization or radiosurgery) for the prevention of death or stroke in patients with un-ruptured brain AVMs followed up for 33 months. However, the methodology and external validity of the trial has been extensively questioned and a consensus on the best management option for un-ruptured AVMs has not been reached (Bambakidis et al, 2014).

2.6 Imaging of brain AVMs

Stereotactic catheter-based DSA has historically been the main imaging modality used for delineation of AVM for GKR planning (Figure 2.6), and it is still considered the reference standard technique for AVM visualization and targeting (Pollock et al, 2016). DSA, which is performed on the day of treatment together with volumetric MRI, enables very high resolution, dynamic and vessel selective, 2D imaging of the cerebral vasculature (Seymour et al, 2016).

Although widely used in most Gamma Knife centres around the world, DSA conveys a small risk of severe peri-procedural complications, it exposes both patients and medical staff to ionizing radiation and carries the risk associated with injection of iodinated contrast agents. Kaufmann et al retrospectively reviewed the complication data of 19826 consecutive patients undergoing diagnostic cerebral angiography at one institution from 1981 to 2003 and reported neurologic complications in 522 examinations (2.63%). Twenty-seven of these (0.14%) were strokes with permanent disability, twelve deaths occurred (0.06%) and access site hematoma (4.2%) was the most common complication overall (Kaufmann et al, 2007).

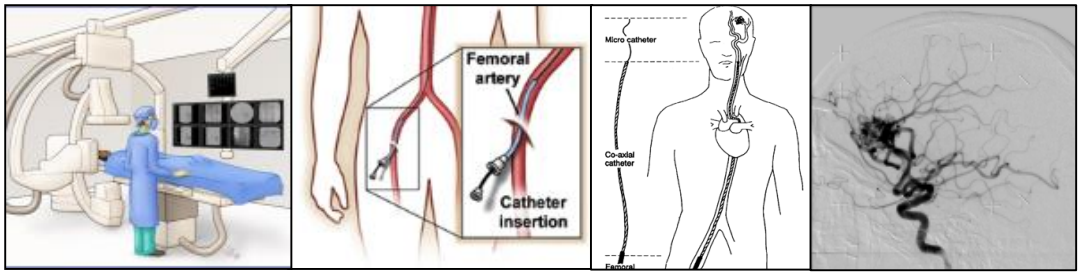

Figure 2.6. Catheter-based cerebral angiography using Digital Subtraction Angiography (DSA). This interventional diagnostic procedure involves insertion of an endovascular catheter into the femoral artery which is then advanced to the intracranial blood vessels. An iodinated contrast agent is injected and a series of 2D X-ray images depicting the architecture of cerebral vessels obtained. After catheter removal, the patient is kept lying flat and under observation for several hours to prevent/early detect potential complications.

Higher obliteration rates and less complications are achieved with GKR when inclusion of the entire AVM nidus is accomplished and the venous drainage excluded from the treatment volume. It is well accepted that, despite its invasiveness, DSA is the best technique currently available for this purpose (Safain et al, 2014). The ideal angiography technique for planning of GKR for AVMs, however, should not only have sufficient space resolution to depict the structural anatomy of the lesion and enough temporal resolution to characterise the vascular dynamics of the abnormality, allowing for heterogeneity in the structure of the blood vessels and flow. It should also involve no radiation or contrast exposure and should be presented in a format compatible with the GKR planning method and software. Table 2.1 summarises the characteristics of the cerebral angiography techniques which could potentially be used for AVM targeting. This list is by no means exhaustive but most currently available angiography techniques can be grouped into one of the listed categories. The papers quoted in Table 2.1 describe the advantages and disadvantages of these techniques compared to DSA.

Cone-Beam CT Angiography (CB-CTA) has been shown to be feasible and useful for planning of GKR of AVMs. Safain et al reported consistent visualization of

the AVM nidus, feeding arteries and draining veins on CB-CTA imaging of a series of 22 patients undergoing GKR (Safain et al, 2014). Nonetheless, CTA is a relatively invasive technique that exposes the patient to ionizing radiation and iodinated contrast agent and is heavily affected by metal or embolic materials causing a starburst like artefact (Figure 3.2). Therefore, the focus of this literature review is on MRA sequences and their individual characteristics that define their suitability for planning of GKR.

Table 2.1. Characteristics of the cerebral angiography technique which could potentially be used for AVM targeting.

Technique			Invasive	Contrast	Radiation exposure	Time resolution	Spatial resolution	Readout	Reference
DSA		**Dynamic 2D X Ray**	Femoral artery catheter	Iodinated contrast	Yes	142 - 333 ms (3-7 f/s)	0.3 mm 1024 × 1024 matrix	NA	(Teksam et al, 2004)
CT Angiography		**CB-CTA**	IV access	Iodinated contrast	Yes	Single time point	Submillimetre 1 mm slices	NA	(Safain et al, 2014)
MR angiography	**TOF**	**TOF**	IV access	Gad based	no	Single time point	0.57x0.57x0.57 mm	NA	(Yu et al, 2012)
	CE-MRA	**TR-CE-MRA**	IV access	Gad based	no	1.4 s	1.02 x 1.13 x 2 mm		(Machet et al, 2012)
		4D-CE-MRA	IV access	Gad based	no	572 ms	1.1 x 1.1 x 1.1 mm	Keyhole	(Kukuk et al, 2010)
	ASL-MRA	**pCASL-VIPR**	no	no	no	Single time point	0.68 x 0.68 x 0.68 mm	Radial acquisition	(Wu et al, 2013)
		4D MRA	no	no	no	83 ms (50 - 100 ms)	1 x 1 x 1 mm	True FISP Cardiac gated	(Yu et al, 2012)
		te-pCASL	no	no	no	200 ms	1.3 x 1.3 x 0.75 mm	T1-TFE-EPI LL readout	(Suzuki et al, 2014)
		CINEMA-STAR	no	no	no	212 ms	1.1 x 1.1 x 0.9 mm	STAR LL readout	(Suzuki et al, 2017)

5.2.1 Time-Of-Flight MR Angiography

TOF imaging is probably the oldest and most popular MRA technique. It relies on the signal difference between stationary background tissues and flowing blood to collect images of the blood vessels (Bednarz et al, 2000). During a TOF acquisition, the static tissue is repeatedly excited with RF pulses reducing the steady-state magnetization signal (signal saturation). Unsaturated blood flowing into the excited volume gives considerably more MR signal than the background tissue creating the blood-to-background contrast known as TOF, Figure 2.7 (Bosmans et al, 1995). The TOF effect is known to improve with increased magnetic field strength and with the addition of gadolinium based contrast agents to the blood (MacDonald & Frayne, 2015). This is because stronger magnetic fields increase the T_1 of static tissue -improving its saturation as well as bulk magnetization- while gadolinium based contrast agents reduce the T_1 of blood which enhances blood magnetisation recovery and improves the contrast between flowing blood and background tissues in this inherently T_1 weighted acquisition (Yang et al, 2002). With the introduction of acceleration techniques and stronger magnetic fields TOF continues to improve and super high resolution images can be obtained with enhanced depiction of smaller vessels (Kang et al, 2009).

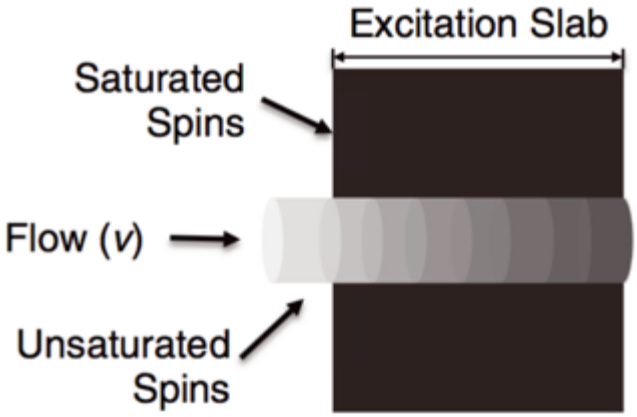

Figure 2.7. Time-Of-Flight effect. TOF imaging relies on the contrast between the repeatedly excited static tissue (saturated) and the unsaturated blood flowing into the acquisition volume. (MacDonald & Frayne, 2015)

5.2.2 Contrast Enhanced MR Angiography

Time-resolved CE-MRA, also referred to as TRICKS, TWIST or TRAK, has been compared to DSA regarding the diagnosis of brain AVMs (Machet et al, 2012). Good sensitivity for brain AVM detection and a good agreement with DSA on nidus size and type of venous drainage was reported. Nonetheless, it still suffers from low temporal and spatial resolution and vessels superposition, making differentiation of the arterial feeders of the nidus difficult at times. CE-MRA using sensitivity encoding (SENSE) in combination with Keyhole acquisition and segmented central *k*-space ordering, i.e., contrast-enhanced robust-timing angiography (CENTRA), has been reported to provide sub-second temporal resolution and 100% agreement with DSA with regard to Spetzler-Martin grade of cerebral AVMs (Hadizadeh et al, 2008).

CE-MRA is performed by tracking an intravenous injection of gadolinium based contrast agents. The MR acquisition sequence uses the T1 shortening produced by gadolinium to collect positive vascular contrast which is also potentiated by the TOF effect of the flowing blood (Bosmans et al, 1995). A 3D T1 weighted image must be collected before contrast injection, usually with a fast gradient recovery echo (GRE) technique such as spoiled gradient recovery (SPGR), and a second image - or a series of images- is acquired when the contrast agent is in the blood vessels of interest. The pre- and post-contrast images are then subtracted leaving only the enhanced signal from the blood vessels (MacDonald & Frayne, 2015).

The acquisition of the second image can be timed to obtain selective images of the arteries or veins if a single time point CE-MRA technique is used. More advanced CE-MRA acquisitions allow time-resolved imaging in order to dynamically visualize the first passage of contrast agent (Lindner et al, 2015). One of these is the keyhole technique in which only one complete reference image, including all the *k*-space, is acquired during the scan and the dynamic images collect only the central *k*-space - or portions of it - which contain the image contrast information, Figure 2.8 (Willinek et al, 2008). The central *k*-space obtained with the dynamic

images is then merged with the profiles of the reference scan to achieve edge definition and sharpness at image reconstruction.

CE MRA has an inherently high signal-to-noise ratio (SNR) compared to other MRA methods, and this allows significant acceleration of the imaging speed with methods such as constrained reconstruction (Chang et al, 2015; Lustig et al, 2007; Swan et al, 2002) and parallel imaging, i.e., SENSE (Haider et al, 2010; Johnson et al, 2010; Taschner et al, 2008). Acceleration rates of up to 60 times have been reported without compromising the overall visual quality (Willinek et al, 2008).

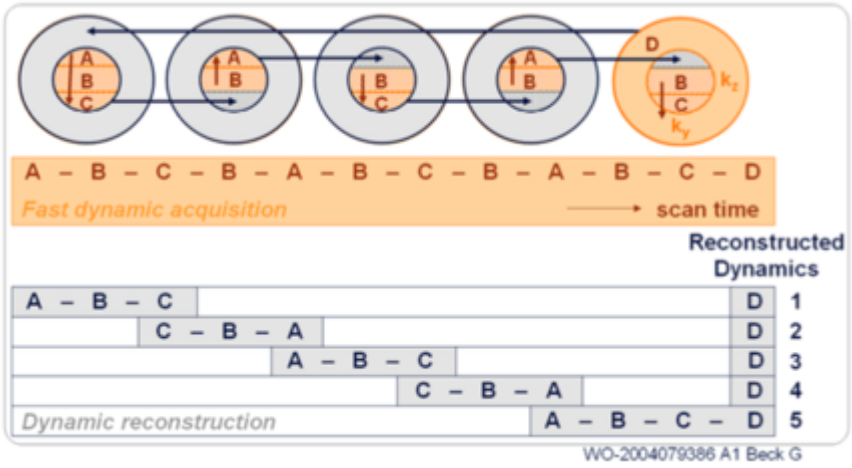

Figure 2.8. Diagram of the accelerated CENTRA Keyhole acquisition method for time resolved CE-MRA mechanism. In this acquisition only a sampled portion of the central *k*-space cylinder is collected in each phase of the fast dynamic acquisition enabling accelerated imaging of the first passage of contrast (Hadizadeh et al, 2011).

5.2.3 Arterial Spin Labelling MR Angiography

ASL is an innovative MR technique in which arterial blood water is magnetically labelled with a radiofrequency (RF) pulse proximal to the brain and used as an intrinsic contrast agent and flow tracer (Le et al, 2012). This is achieved by inverting the longitudinal magnetization of arterial water spins which changes the contrast properties of inflowing blood with respect to the surrounding tissue (Alsop & Detre, 1998). The subtraction of an image with inverted blood spins (label) and without inversion (control) results in images of the inflowing blood only (Lindner et al, 2015). Under normal conditions, most labelled water is extracted at the capillary level into the tissue, giving rise to the parenchymal perfusion signal intensity for which ASL is better known (Petersen et al, 2006; Xu et al, 2010). The same principle, with an early acquisition -before the tagged water leaves the vasculature- can be applied to obtain angiographic images with near zero background and inflow dynamics similar to DSA, as seen in Figure 2.9 (Suzuki et al, 2014). The T1 recovery of the labelled spins is shorter than capillary transit time and for this reason signal intensity is not normally seen within intracranial veins in ASL angiography (Kukuk et al, 2010). However, because AVMs lack a capillary bed for water extraction to take place, and the labelled spins are shunted into the venous circulation with minimal transit time, venous signal intensity can be obtained from the AVM draining veins using ASL (Jang et al, 2014).

Depending on the labelling strategy and the image acquisition technique, static (Wu et al, 2013) or time-resolved images (Jang et al, 2014; Kopeinigg & Bammer, 2014) of the whole vascular tree (Wu et al, 2013) or only individually selected branches can be generated (Dai et al, 2010; Robson et al, 2010). Continuous or pulsed labelling strategies can be used with ASL. Pulsed methods are preferred for time resolved angiography because the inversion of a defined blood volume at once enables the leading portion of the bolus to be scanned as it reaches the imaging slab (Yan et al, 2010). In continuous ASL, flowing blood is continuously labelled and as a consequence tagged blood spins may have already reached the imaging slab by the time of acquisition and this makes it difficult to

visualize the arrival of the labelled bolus. Nonetheless, continuous ASL can have higher labelling efficiency and vessel selectivity (Helle et al, 2013; Wu et al, 2007).

Regarding the acquisition methods, a 3D technique is preferred for visualization of the whole cerebral vasculature because signal at all locations is sampled simultaneously and it allows image reformatting in arbitrary views (Lindner et al, 2015). Single thick slab acquisitions can be used to reduce scanning time but their image resolution and geometrical coverage are poorer (Robson et al, 2010). 3D balanced steady state free precession (bSSFP) also allows shorter acquisition with good signal-to- noise ratio (SNR) but it is rather susceptible to artefacts and poor image quality (Bieri & Scheffler, 2005). Radiofrequency spoiled gradient echo imaging (T1-TFE) is a commonly used method with high SNR which is favoured by its less tendency to artefacts (Nakamura et al, 2013).

Feasibility studies with non-contrast enhanced 3D intracranial MR angiography using pseudo-continuous arterial spin labelling (pCASL) and an accelerated radial acquisition known as vastly under-sampled isotropic projection (VIPR) achieved very good spatial resolution (0.68 x 0.68 x 0.68 mm, Table 2.1). It demonstrated reduced saturation artefacts compared with a standard TOF protocol in five healthy and five diseased subjects and showed great promise for static intracranial angiography (Wu et al, 2013). Furthermore, the combination of pCASL with 3D T1 Turbo-Field Echo (TFE) readout and a keyhole acceleration has enabled the acquisition of time-resolved (4D) MRA with high spatial and temporal resolution (Helle et al, 2010). Similar sequences using different combinations of labelling strategy, acquisition technique and acceleration methods have been recently described and successfully applied to several cerebrovascular diseases (Jensen-Kondering et al, 2015).

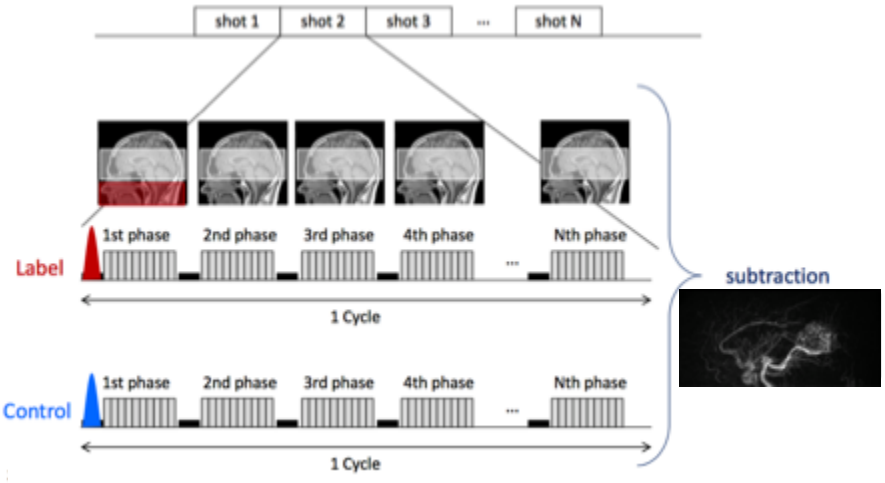

Figure 2.9. 4DASL angiography labelling and sequence diagram. The labelling plane is positioned proximal to the imaging slab and two sets of interleaved tagging states, control and label, are acquired and subtracted to yield an angiographic image. Courtesy of Yuriko Suzuki (Suzuki et al, 2014).

3. Investigation of dosimetric differences between the TMR 10 and convolution algorithm for Gamma Knife Stereotactic Radiosurgery

Rojas-Villabona, A., Kitchen, N. & Paddick, I.

J Appl Clin Med Phys (2016), 17(6), 217-29.

3.1 Abstract

Introduction: Since its inception, doses applied using GKR have been calculated using a simple TMR algorithm, which assumes the patient's head is of even density, the same as water. This results in a significant approximation of the dose delivered by the Gamma Knife. We investigated how GKR dose calculations varied when using a new convolution algorithm clinically available for GKR planning that takes into account density variations in the head compared with the established calculation algorithm.

Methods: Fifty-five patients undergoing GKR and harbouring 85 lesions were voluntarily and prospectively enrolled into the study. Their clinical treatment plans were created and delivered using TMR 10, but were then recalculated using the density correction algorithm. Dosimetric differences between the planning algorithms were noted. Beam-on-time, which is directly proportional to dose, was

the main value investigated. Changes of mean and maximum dose to organs at risk (OAR) were also assessed. Phantom studies were performed to investigate the effect of frame and pin materials on dose calculation using the convolution algorithm.

Results: Convolution yielded a mean increase in beam-on-time of 7.4% (3.6% – 11.6%). However, approximately 1.5% of this amount was due to the head contour being derived from the CT scans, as opposed to measurements using the Skull Scaling Instrument with TMR. Dose to the cochlea calculated with the convolution algorithm was approximately 7% lower than with the TMR 10 algorithm. No significant difference in relative dose distribution was noted and CT artefact typically caused by the stereotactic frame, glue embolization material or different fixation pin materials did not systematically affect convolution isodoses. Nonetheless, substantial error was introduced to the convolution calculation in one target located exactly in the area of major CT artefact caused by a fixation pin.

Conclusions: Inhomogeneity correction using the convolution algorithm results in a considerable, but consistent, dose shift compared to the TMR 10 algorithm traditionally used for GKR. A reduction of the prescription dose may be necessary to obtain the same clinical effect with the convolution algorithm. Head shape definition using CT outlining can reduce treatment uncertainty from head shape approximations.

3.2 Introduction

GKR relies on mathematical algorithms to predict the distribution of ionizing radiation in the brain (Wu et al, 1996). The dose distribution is affected by electron density heterogeneities of the tissues and this is a well-established concept that is compensated for in conventional radiotherapy and other forms of radiosurgery (Lu et al, 2005). However, for a number of reasons heterogeneity corrections have been unavailable for GKR. Doses applied with GKR have been traditionally calculated using a simpler water-based algorithm (Elekta, 2011a). The TMR 10 is the most recent enhancement of the water-based dose calculation algorithm used for GKR and it relies on a number of approximations to enable fast isodose computation during treatment planning. One of the most significant of these is the approximation of the head to water-equivalent density and this could introduce important uncertainty to isodose and beam-on-time calculations due to the increased electron density of brain and bone (relative to water) and the near-zero density of air cavities in the skull (Nakazawa et al, 2014b).

The TMR 10 algorithm requires input data of off-axis ratios (dose profiles) and other parameters, such as, output factors, attenuation/virtual attenuation coefficients, virtual source-to-focus distances and scaling distances. The data used as input for the simulation has been extracted by analysing Monte Carlo simulations and subsequently adapting the calculation model to the results (Sempau et al, 2001). This simple algorithm was a practical method to overcome the relatively slow processing capabilities of older workstations, but with the advent of faster processors, the effect of tissue inhomogeneities can finally be calculated in reasonable time during the treatment planning process (Mack et al, 2006).

The ability to account for tissue heterogeneity in GKR has become available in the form of a convolution algorithm (Elekta, 2011b). It calculates dose by convolving a field describing the total amount of energy released by primary photons per unit mass (TERMA) with kernels describing how the energy is distributed by secondary particles (Lu et al, 2005). To account for tissue

heterogeneities in the head, the TERMA and the kernels are scaled by material densities obtained from CT Hounsfield units (HU), which are directly proportional to the electron density of the tissues (Wu et al, 1996).

The Convolution algorithm is known to more accurately predict dose distributions across the brain (Xu et al, 2014; Xu et al, 2015). However, doses used for GKR were tested and optimized using water-based algorithms over the last few decades and the dosimetric differences between the water-based and convolution algorithms need to be better understood before this method can be confidently employed in a clinical setting. This study is aimed to understand the dosimetric implications of using convolution algorithm for GKR.

3.3 Methods

Treatment plans of a representative group of patients were created using the TMR 10 algorithm and re-planned using the convolution algorithm. Beam-on-time, which is proportional to treatment dose, and a number of metrics commonly used to evaluate dose distribution, such as the Paddick Conformity Index (PCI), Gradient Index (GI) and coverage were estimated with both algorithms. Changes of mean and maximum dose to OAR were also assessed. Phantom studies were performed to investigate the effect of frame and pin materials on dose calculation using the convolution algorithm.

3.3.1 Patients

Fifty-five patients undergoing GKR for a variety of intracranial diseases between September 2013 and June 2014 were recruited for the study. Table 3.1 shows the demographic and diagnosis details of these subjects. The study was approved by the Queen Square Research Ethics Committee (Appendix 1). Written consent was received from all participants for an additional stereotactic CT scan of the head which is not part of the standard imaging procedure for planning of GKR in our centre. Please see appendix 2 for ethical considerations.

Table 3.1. Demographic and diagnosis details of the study subjects.

Age mean (range): 53.4 (26 - 76)		
Female: 32 (58.2%)		
Diagnosis	**Patients**	**Targets (%)**
Meningioma	16	24 (28.2)
Acoustic neuroma	17	17 (20.0)
AVM	11	12 (14.2)
Trigeminal neuralgia	4	4 (4.7)
Multiple metastases	3	24 (28.2)
Single metastases	2	2 (2.4)
Paraganglioma	2	2 (2.4)
Total	**55**	**85 (100%)**

3.3.2 Radiosurgery planning procedure with TMR 10

A Leksell stereotactic coordinate frame G (Elekta Instruments AB, Stockholm, Sweden) was applied to the head of the patients using titanium pins. Twenty-four manual measurements of the patient's head were manually taken for head shape approximation using the skull scaling instrument or "bubble" method shown in Figure 3.1.

Stereotactic imaging for planning included three dimensional (3D) post-contrast T1 and T2 weighted sequences acquired with a Magnetom Avanto 1.5 T MRI system (Siemens AG, Erlangen, Germany) as follows: T1 weighted: fast low angle shot (FLASH); T2 weighted: constructive interference in steady state (CISS); acquisition matrix: 448 x 448; Slice thickness: 1.5 mm, no overlap; Field of view (FOV): 210 x 210 mm; voxel size: 0.47 x 0.47 x 1.5 mm. GKR treatment plans were created using Leksell GammaPlan 10.1 and the water-based TMR 10 algorithm (Elekta Instruments AB). Targets and OAR were delineated and a treatment plan produced using several radiation isocenters to conformaly cover the target volume. Dose and prescription isodose were chosen based on recognized standards for each pathology (Lippitz et al, 2014). Treatments were delivered using a Leksell Gamma Knife Perfexion (Elekta AB).

The quality of head shape approximation with the scaling instrument and target position were thought to influence potential differences of beam-on-time between the dose calculation algorithms and they were therefore further assessed for each target. Discrepancies between the head outline obtained from manual measurements (red line, Figure 3.1d) and the head contour as observed in the CT scan (Figure 3.1e) were manually assessed by a single observer (ARV) at the axial level of the target initially. Multiplane evaluations were subsequently performed, looking for discrepancies above or at the level of the target, which is the expected trajectory of the beams. The maximum distance between the actual head contour and the line of the head shape from manual measurements were recorded using arbitrary ranges as follows: less than 0.5 cm, 0.5 to 1 cm and more than 1 cm. The position of the target in the head was evaluated with reference to the skull base, the head surface and the apex, manually measuring the minimum distance between these structures and the margin of the target. The targets were then classified using arbitrary thresholds - that is to say, skull base lesion if less than 2.5 cm from any bony structure on the base of the skull (n: 35), apex target if less than 2.5 cm from the highest point of the head in the stereotactic system (n: 10), and superficial if less than 2.5 cm from the head surface at any point (n: 28). These categories were not mutually exclusive.

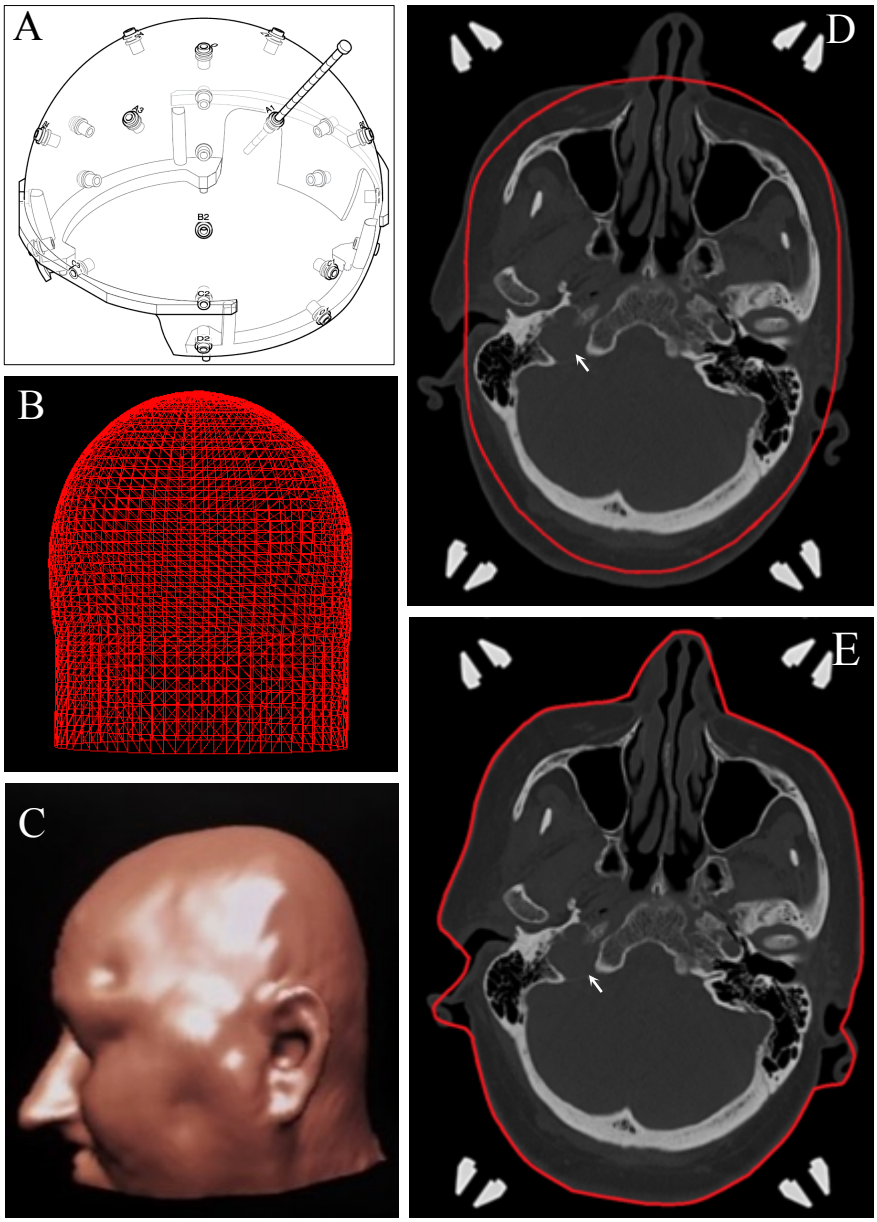

Figure 3.1. Head shape approximation methods. Skull scaling instrument (A) and the 3D model (B) generated with twenty-four manual measurements of the patient's head. Segmentation of the head surface using CT outlining produces a more accurate head shape model (C) and visual assessment of the CT scans can easily reveal discrepancies between the manual method (D) and CT outlining (E) in a subject with a right paraganglioma (arrow).

3.3.3 CT imaging and electron density calibration

Stereotactic non-contrast CT scanning of the whole head was performed in all subjects using a Siemens Somatom Definition AS multislice helical CT scanner (Siemens AG, Forchheim, Germany). Acquisition matrix: 512 x 512; Slice thickness: 1.5 mm, no overlap; FOV: 240 x 240 mm; voxel size: 0.47 x 0.47 x 1.5 mm. A frame-CT adapter was used to position the patient on the CT scanner.

A Gammex 467 Tissue Characterization Phantom (Gammex. Middelton, WI, USA) together with the CT scanner and parameters above were used to establish the relationship between electron density (ρe) of various tissues and their corresponding CT number in HU for that specific scanner (Constantinou et al, 1992). The CT number and electron density relative to water of the rod materials for the phantom used were entered in the treatment planning system and used as a reference for inhomogeneity corrections using the convolution algorithm.

3.3.4 Treatment re-planning with convolution algorithm

The original treatment plans calculated with the TMR 10 algorithm were transferred to an independent Leksell GammaPlan 10.1 workstation, calibrated with the same reference dose (3.484 Gy/min to 20/10/2012), for re-planning. The head segmenting tool in Leksell GammaPlan 10.1 was used to generate a 3D model of the patient's head from CT images (Figure 3.1c and 3.1e). Minor modifications were performed manually to correct errors in irregular areas such as nose and ears and to completely exclude the stereotactic frame which can be mistakenly included in the model. The treatment plan was initially recalculated with the same TMR 10 algorithm, but using the new head shape obtained from CT outlining. All other treatment parameters including prescription dose, percentage isodose, number and location of isocenters and collimator size remained locked. Under these conditions it can be safely assumed that beam-on-time is directly proportional to delivered dose.

Electron density was subsequently calculated for each case using the CT scans and parameters from the calibration procedure above. The CT fiducial indicator

box was excluded from the electron density calculations in GammaPlan and the treatment plans re-calculated using the convolution algorithm. Dose calculations in Leksell GammaPlan 10.1 can be made independently for each individual target or summed to account for scatter from other targets in the case of multiple lesions. The latter method better represents the dose delivered to the patient and this was used to obtain the study figures.

3.3.5 Statistical analysis

The non-parametric Wilcoxon signed-rank test was primarily used to assess the significance of differences in beam-on-time between the treatment plans. The actual difference, in minutes, between treatment plans does not fully describe the effect of heterogeneity correction for GKR planning. Therefore, percentage difference in beam-on-time was calculated for each target and used for further statistical analysis. Beam-on-time percentage difference was normally distributed and the independent samples t-test was used to compare target groups (e.g., skull base vs. non-skull base targets). Analysis of variance (ANOVA) was used to compare percentage difference in beam-on-time between diagnoses and Spearman's rank correlation coefficient (ρ) was used to assess the relationship between percentage difference in beam-on-time and other numerical variables (i.e., TV, number of isocenters, beam-on-time) with the convolution algorithm. Each target was considered an independent study element for statistical purposes and data analysis was performed using the Statistical Package for the Social Sciences (SPSS Statistics, Version 22, IBM Corp).

3.3.6 Effect of frame and pin materials on convolution calculation

The effect of CT artefact from the frame materials on inhomogeneity correction with the convolution algorithm was evaluated using a Leksell Gamma Knife Solid Water dosimetry phantom (Elekta Instruments AB). The phantom was initially scanned without the Leksell G frame fixation posts and pins using the same CT scanner and parameters above. Subsequently, the frame fixation posts and titanium pins were added to the phantom setup and scanned under the same

conditions. The angled long insulated posts (155 mm) were used anteriorly and the medium straight posts (110 mm) posteriorly, to mimic a typical clinical setup. Posts were positioned in the *z* (sup-inf) direction to maximise the chance that some beams passing through the calibration point (100,100,100) would pass through the pins. Typical clinical pin lengths of 35 mm anteriorly and 45 mm posteriorly were used.

The CT fiducial indicator box was then added to the phantom arrangement which was re-scanned using different pin materials (i.e., titanium, aluminium and older style aluminium/tungsten carbide tip pins). An experimental GKR plan was generated using the convolution algorithm and a single 4 mm shot located in the centre of the coordinate system (100, 100, 100). The maximum dose was set to 100 Gy and the dose rate was 2.704 Gy on the day of the experiment. Convolution plans were then calculated using the CT scans from each of the scenarios described above. The planning procedure was also performed with single isocenters of the 8 and 16 mm collimators.

3.4 Results

In total 85 targets were treated in 55 subjects recruited for the study. These were adequately distributed across the head with 41% of the targets located less than 2.5 cm from a bony structure in the skull base and 12% of the targets located less than 2.5 cm from the apex. Meningiomas (24 targets in 16 patients) and brain metastases (26 lesions in 5 patients) were the most common lesions comprising around two thirds of the study targets (Table 3.1). Four AVM patients had undergone partial embolization of their vascular lesion with 25 - 50% Glubran (N-butyl-cyanoacrylate and metacrylossisulfolane; GEM, Viareggio, Italy) suspended in ethiodized oil. Table 3.2 summarizes the estimates of beam-on-time, coverage, PCI and GI for the three treatment plans produced per target, i.e., 1. TMR 10 algorithm and head definition from manual measurements, 2. TMR 10 algorithm and head definition from CT scans, 3. Convolution algorithm and head definition from CT scans.

Table 3.2. GKR plans calculated with different dose calculation algorithms and head shape approximation method. Parameters of treatment plans created using the TMR 10 algorithm and head approximation with the skull scaling instrument (1) and recalculated using head definition from CT scan outlining (2) and the convolution algorithm (3).

Parameter	**1. TMR 10 + manual measurements** mean (min - max) median; SD	**2. TMR 10 + CT head definition** mean (min - max) median; SD	**3. Convolution + CT head definition** mean (min - max) median; SD
Beam-on-time (min) n: 84[a]	31.12 (6.5 – 83.9) 30.2; 18.6	31.59 (6.6 – 85.5) 30.7; 18.9	33.39 (6.8 – 89.3) 32.7; 19.9
Coverage (%) n: 80[a,b]	97.5 (94.3 – 100) 97.0; 1.58	97.4 (94.3 – 100) 97.0; 1.6	97.0 (91– 100) 96.6; 0.83
PCI n: 52[a,b,c]	0.82 (0.48 – 0.93) 0.84; 0.08	0.82 (0.48 – 0.93) 0.84; 0.08	0.82 (0.51 – 0.93) 0.84; 0.08
GI n: 45[a,c,d]	2.776 (2.48 – 3.52) 2.730; 0.244	2.776 (2.48 – 3.52) 2.730; 0.245	2.749 (2.46 – 3.53) 2.660; 0.253

[a] 1 target excluded due to its location in the area of pin distortion in the CT scan.
[b] No treatment volume calculated for trigeminal neuralgia cases
[c] PCI and GI were ignored for 28 small lesions with TV < 0.5 cc (Paddick, 2000; Paddick & Lippitz, 2006)
[d] GI was not calculated for 11 lesions with close proximity to another target.

Beam-on-time calculated with the convolution algorithm was longer for all the study targets except a very small metastatic lesion which was located precisely under the frame fixation pin as shown in Figure 3.2. The CT artefact generated by the titanium pin introduced significant error to the convolution calculation through an abnormally low-density artefact in the CT scan (HU: -664.4, SD: 65.84; $\rho_{e:}$ 0.291, < water). This resulted in a shorter beam-on-time if the convolution algorithm was used compared to TMR 10 (6.08 vs. 6.10 min, respectively). This lesion was excluded from further analysis. The percentage difference in beam-on-time between treatment plans, for the 84 targets included in the analysis, are summarised in Table 3.3. No significant difference in coverage, PCI or GI was observed between the head shape definition methods or dose algorithms.

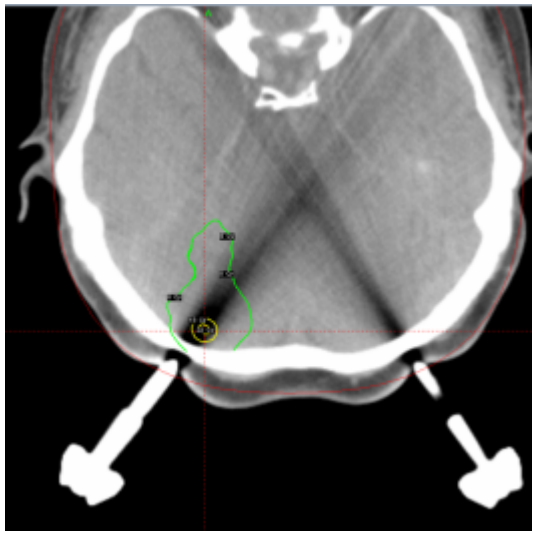

Figure 3.2. CT artefact from titanium fixation pin introducing significant error to the convolution calculation. Small brain metastasis (TV: 0.057 ml) located precisely under the Leksell G frame pin causes significant CT scan distortion and shorter beam-on-time if the convolution algorithm is used.

Table 3.3. Change in beam-on-time between treatment plans calculated with different head shape approximation methods and dose calculation algorithms.

	1. Manual measurements vs CT head definition mean (min - max) SD; (*p*) [b]	**2. TMR 10 vs convolution** mean (min - max) SD; (*p*) [b]	**3. Overall difference** mean (min - max) SD; (*p*) [b]
Beam-on-time % difference n: 84[a]	1.45% (0.0 – 3.4) 0.76; < *0.001*	5.86% (2.1 – 8.8) 1.21; < *0.001*	7.39% (3.6 – 11.6) 1.42; < *0.001*

[a] 1 target excluded. Very small lesion in the area of the pin artefact.
[b] Wilcoxon signed-rank test

3.4.1 Dosimetric effect of head approximation

Head shape definition using CT outlining resulted in an average increase of 1.45% (95%CI: 1.3 - 1.6; $p < 0.001$) in beam-on-time compared to treatment plans using manual measurements with the skull scaling instrument. Beam-on-time with CT outlining was the same (n: 8) or longer in all cases and the maximum difference observed was 3.4%. The latter was a skull base target with significant discrepancies between the head approximation methods (Figures 3.1d and 3.1e). Visual evaluation of the head shape generated from manual measurements showed a discrepancy of more than 0.5 cm at the axial level of 70% of the targets and a multiplane discrepancy of more than 1 cm was observed above or at the level of 31% of the targets. The change in beam-on-time for lesions with a discrepancy of more than 0.5 cm at the axial level of the target (1.7%; 95%CI: 1.5 - 1.9%) was significantly higher than the rest of the lesions (0.9%; 95%CI: 0.6 - 1.2%); $p < 0.001$. Similarly, lesions with more than 1 cm discrepancy above or at the level of the target (1.6%; 95%CI: 1.4 - 1.7%) had significantly higher changes in beam-on-time compared to targets with less than 0.5 cm multiplane discrepancy (0.6%; 95%CI: 0.3 - 0.9%); $p < 0.001$.

Table 3.4 shows the relative difference in beam-on-time between the planning methods per diagnosis. Convolution seems to reveal a fairly consistent shift from

TMR 10 for indications where the target location is the same (e.g., vestibular schwannoma). For indications where the location varies widely (e.g., meningiomas or metastases) convolution seems to demonstrate greater dosimetric inconsistencies. The ANOVA, however, failed to demonstrate a significant difference in beam-on-time percentage between diagnosis groups ($p = 0.115$). Location of the target in the head, specifically the depth, appears to negatively correlate with change in beam-on-time between the TMR 10 and convolution algorithm. Tumours located less than 2.5 cm from the surface at any point in the head showed greater changes in beam-on-time compared to deeper lesions, 6.5% (95%CI: 6.1 - 6.9; SD: 1.03) vs. 5.5% (95%CI: 5.2 - 5.8; SD: 1.17), $p < 0.001$, respectively. Similarly, distance from the edge of the target to the head surface negatively correlated with percentage change in beam-on-time between the algorithms (ρ: -0.36, $p = 0.001$).

Change in beam-on-time for targets located in the skull base was not significantly different from those distant to that bony structure (5.6% vs. 6.0%; $p = 0.1$). Similarly, no relative difference was noted between targets located in the apex and the rest of the lesions distributed across the head anatomy (6.2% vs. 5.8%; $p = 0.27$). Beam-on-time percentage difference between the planning algorithms did not correlate with target volume (ρ: 0.12; $p = 0.2$), number of shots (ρ: -0.005; $p = 0.96$), beam-on-time with TMR 10 algorithm (ρ: -0.14, $p = 0.19$) or difference in beam-on-time between the head shape definition methods (ρ: 0.08; $p = 0.47$). Beam-on-time difference in AVM patients who had undergone partial glue embolization (5.2%; 95%CI: 4.3 – 6.1; SD: 0.56) was comparable to patients without previous endovascular treatment (5.0%; 95%CI: 4.2 – 5.7; SD: 0.8), and no significant difference between them was noted ($p = 0.6$).

Table 3.4. Relative difference in beam-on-time between the TMR 10 and convolution algorithm per diagnosis.

	TMR 10 vs convolution mean (min - max) SD; (*p*) [b]	**Overall difference Convolution + head definition from CT scans** mean (min - max) SD; (*p*) [b]
AVM n: 12	5.1% (3.7 – 6.3) 0.76; *0.002*	6.0% (4.7 – 8.0) 1.0; *0.002*
Metastases n: 25[a]	5.8% (2.0 – 7.9) 1.42; *< 0.001*	7.1% (3.6 – 10.1) 1.63; *< 0.001*
Meningioma n: 24	6.2% (4.4 – 8.6) 1.03; *< 0.001*	7.8% (6.0 – 11.6) 1.24; *< 0.001*
Trigeminal neuralgia n: 4	5.4% (4.7 – 6.8) 0.95; *0.068*	7.3% (6.5 – 8.3) 0.74; *0.068*
Acoustic neuroma n: 17	5.9% (4.5 – 7.6) 0.94; *< 0.001*	7.9% (6.6 – 9.8) 0.85; *< 0.001*
Paraganglioma n: 2	6.2% (3.5 – 8.8) 3.75; *0.18*	8.7% (7.0 – 10.4) 2.35; *0.18*

[a] 1 target excluded due to its location in the area of pin distortion in the CT scan
[b] Wilcoxon signed-rank test

3.4.3 Dose to organs at risk

Clinically relevant OAR were defined in 28 subjects and differences in mean and maximum dose between the TMR 10 and convolution plans were calculated. The ipsilateral cochlea was the OAR in twenty-four cases with vestibular schwannoma, cerebellopontine angle meningioma, paraganglioma and trigeminal neuralgia. The mean and maximum calculated dose to the cochlea with the convolution algorithm was approximately 7% lower than equivalent estimates obtained with the TMR 10 algorithm, as shown in Table 3.5. The optic apparatus was in close proximity to the target in four subjects and a lesser effect on mean and maximum dose to this OAR (2.0 and 2.4%, respectively) was noted between the planning algorithms.

Table 3.5. Difference in dose to organs at risk between the TMR 10 and convolution algorithm.

Organs at risk		TMR 10 mean (95%CI); SD	Convolution mean (95%CI); SD	% Difference mean (min - max); SD
Cochlea n: 24	mean dose (Gy)	2.7 (2.2–3.2); 1.1	2.5 (2.1–3.0); 1.0	- 7.3% (3.6–11.1); 2.12
	max dose (Gy)	4.8 (3.6–5.9); 2.7	4.5 (3.3–5.6); 2.7	- 7.0% (1.6–11.7); 2.49
Optic apparatus n: 4	mean dose (Gy)	3.5 (2.3–4.7); 0.8	3.4 (2.2–4.5); 0.7	-2.0% (0.0–3.1); 1.4
	max dose (Gy)	6.5 (4.9–8.2); 1.05	6.4 (4.6–8.2); 1.1	- 2.4% (1.3–5.3); 1.89

3.4.4 The effect of frame and pin materials on convolution calculation

The effect of CT distortion from the stereotactic frame on the convolution algorithm was assessed by means of change in beam-on-time if an identical treatment plan was calculated using CT scans acquired with and without the Leksell frame G. The experiment demonstrated a maximum 4% longer beam-on-time using the CT acquired with the posts and pins for the plan composed of a single shot of the 4 mm collimator. This effect was smaller for a similar plan with the 8 mm collimator and no effect at all was seen for the 16 mm collimator, Table 3.6.

No significant difference in beam-on-time was seen if the titanium or aluminium pins were used for single shot plans of the 4, 8 and 16 mm collimators. Only a small change of the order of 0.8% was seen for the 4 mm collimator plan if the aluminium/tungsten carbide tip pins were used compared to titanium or aluminium pins.

Table 3.6. Effect of the stereotactic frame on the convolution algorithm.

	Phantom only beam-on-time	**Frame and pins No fiducial indicator box** beam-on-time	**Percentage difference**
4 mm	73.23 min	76.21 min	4.0 %
8 mm	43.79 min	44.56 min	1.7 %
16 mm	37.34 min	37.26 min	- 0.2 %

3.5 Discussion

This study aimed to evaluate the dosimetric implications of using inhomogeneity corrections with the convolution algorithm for GKR. The novel algorithm, available in the GKR planning system, was compared to TMR 10 which is the standard water-based algorithm traditionally used in GKR. Fifty-five actual GKR treatment plans were re-calculated with the convolution algorithm keeping all other treatment parameters unchanged and the study provided clinically relevant information on the magnitude of dose approximations traditionally accepted with TMR 10 algorithm. The overall dose difference if convolution algorithm is used along with head definition from CT outlining, is 7.4% on average and the maximum observed was 11.6%. However, 1.5% of this amount is due to the increased accuracy of the head contour from the CT scans, as opposed to manual measurements from the skull scaling instrument.

3.5.1 Dose implications of convolution algorithm for GKR

Doses currently used for GKR are the result of several decades of empirical optimisation using water-based algorithms. This titration process has resulted in a set of dosage recommendations shown to provide maximum clinical efficacy with the lowest morbidity (Lippitz et al, 2014). These doses have incorporated the uncertainty inherent to water-based algorithms and treatment plans calculated

with the new calculation algorithm should therefore be adequately understood and adjusted to ensure the dose delivered is comparable.

The increment in dose to the target, attributable to inhomogeneity corrections, if exactly the same TMR 10 treatment plan is recalculated with the convolution algorithm was found to be 5.9% in our study. Similar results have been reported with phantom and clinical experiments (Xu et al, 2015). Xu et al reported an average dose difference of 6.5% between the convolution and the TMR classic algorithm using a single shot placed in different positions along the *x*, *y* and *z* axes on the stereotactic system with varying collimator sizes in a polystyrene phantom and a human head CT scan (Xu et al, 2014). Their study compared the dose calculation algorithms with a fixed geometry and established the baseline performance of the convolution algorithm. Similarly, Nakazawa et al found a 1 - 7% change of absolute dose to the target in 29 cases of vestibular schwannomas which were re-planned with the convolution algorithm (Nakazawa et al, 2014b). Our study does not only quantify the uncertainty of the water-based algorithm in a larger group of patients with different intracranial conditions but it also informs radiosurgery prescribers on dose adjustments that may be required if the convolution algorithm is to be used clinically. For example, in a typical trigeminal neuralgia case a maximum dose of 80 Gy is planned with the TMR 10 algorithm. Re-planning this treatment with the convolution algorithm (assuming that homogeneity correction better simulates dose distribution) reveals that this target would actually receive a lower dose of around 76 Gy when treated with TMR 10. Table 3.7 shows similar estimates for other pathologies and demonstrates the rather conservative approach of the water-based algorithm where the uncertainty always results in “under-treating” the target. However, if the trigeminal neuralgia patient above was to be treated with the convolution algorithm and the same prescription isodose, 80 Gy would actually be delivered to the target which exceeds the originally intended dose.

Table 3.7. Dosimetric differences between the TMR 10 and convolution algorithm for GKR per diagnosis.

	Prescription dose	**Beam-on-time % difference TMR 10 vs convolution** mean (min - max)	**Dosimetric change with convolution** (Gy)
AVM n:12	25 Gy	5.1% (3.7 – 6.3)	1.27 Gy (0.9 – 1.6)
Metastases n:25	25 Gy	5.8% (2.0 – 7.9)	1.45 Gy (0.5 – 1.9)
Meningioma n:24	15 Gy	6.2% (4.4 – 8.6)	0.93 Gy (0.7 – 1.3)
Trigeminal neuralgia n:4	80 Gy	5.4% (4.7 – 6.8)	4.32 Gy (3.7 – 5.4
Acoustic neuroma n:17	13 Gy	5.9% (4.5 – 7.6)	0.76 Gy (0.5 – 1.0)
Paraganglioma n:2	15 Gy	6.2% (3.5 – 8.8)	0.93 Gy (0.5 – 1.3)

The clinical significance of dose differences between the TMR 10 and convolution algorithm is debatable. No clinical studies have been published reporting outcomes of patients treated with the convolution algorithm but evidence from standard radiotherapy suggests that doses should be adjusted to obtain the same clinical effect if a homogeneity correction is to be used (Aarup et al, 2009; Vanderstraeten et al, 2006). The dose shift in our study seems to be consistent, particularly for tumours with the same location, and a simple dose reduction could potentially be sufficient to compensate for the differences between the planning algorithms (Table 3.7). Phantom-based studies initially demonstrated substantial changes in dose distribution in bone tissue and tissue interfaces (Moskvin et al, 2004). However, no substantial difference in dose distribution surrogates such as gradient index, PCI and coverage was noted in our study. Nakasawa et al also reported no change of relative dose distribution by visual assessment of the plans and suggested that the setting of multiple beams from all directions would offset the discrepancy of the dose distribution around the target. The latter could also explain our finding of lower difference in beam-on-time for targets deeply located in the brain where a higher degree of

uncertainty compensation takes place as the beams travel longer distances through different tissue densities.

The dosimetric differences between the planning algorithms in our study were relatively consistent particularly for targets located in the same area (i.e., trigeminal neuralgia and vestibular schwannomas). Therefore, keeping the same absolute dose by simply reducing the prescription isodose if the convolution algorithm is used may be appropriate for these pathologies. The dose uncertainty with TMR 10, however, seems to be less predictable for pathologies with variable location in the brain, such as metastases or meningiomas, and the convolution algorithm could better simulate the true dose delivered to these individual targets. Further clinical studies and close monitoring of outcomes for patients treated with the convolution algorithm must also be prospectively conducted to investigate potential differences on efficacy and side effects profile. A further implication of using a new dose calculation algorithm for GKR is the potentially poor comparability between clinical studies performed using the TMR 10 and the convolution algorithm in the future.

The study also investigated differences in dose to OAR with the convolution algorithm, particularly the cochlear apparatus. Our findings demonstrate that doses delivered to the cochlea with the TMR 10 algorithm are actually 7.0% lower than initially thought. This difference is well explained by the high density of the temporal bone where the cochlea is embedded and reflects the fact that TMR 10 does not take into account attenuation of the beams as they travel through different tissue densities. A further degree of reduction in dose to the cochlea could take place if the prescription dose with the convolution algorithm were to be adjusted to deliver the same dose traditionally delivered to the targets with the TMR 10 algorithm.

3.5.2 Potential dose calculation inaccuracies with convolution

The convolution algorithm is by definition a better method to predict dose distribution in the brain and most modern therapeutic radiation techniques now

rely on inhomogeneity corrected dose calculations (Vanderstraeten et al, 2006). Convolution is, however, based on the physical densities of tissues obtained from tomographic studies and errors can be introduced to the calculation if artefacts are present. Potential inaccuracies arise mainly from external elements that change the apparent density of the tissues in the CT scan, i.e., contrast agent, intracranial clips, titanium cranioplasties, embolization materials and the stereotactic frame itself. In our study, one of the targets (out of 85) was considerably affected by imaging artefact from the frame pins and in this specific case the uncertainty of the convolution algorithm was significantly high. A method of overriding the electron density in areas of artefact would significantly reduce this uncertainty.

A visual evaluation of the whole head CT scan should be sufficient to detect CT artefacts that potentially affect the convolution calculations. Adequate electron density calibration needs to be performed for each individual CT scan and scanning protocol and special attention must be given to the consistency of the scanning procedure to reduce technical variability.

In our study, the imaging procedure was done with the stereotactic frame and this can produce CT artefact itself, as seen in Figure 3.2. Distortion from the frame ring occurs mainly in the lowest aspect of the scan and this is very unlikely to be part of a beam's incoming trajectory. However, areas of artefact caused by the fixation posts and pins are certainly likely to be crossed by the collimated beams. Apart from our incidental finding of a lesion located precisely under the fixation pin, it was not possible to investigate the effect of the frame artefact in the patients and their more complex radiosurgery plans. Nonetheless, the phantom studies demonstrated no change on treatment plans with the 8 and 16 mm collimators and only a minor change (4%, worst-case scenario) if a single shot of the 4 mm collimator is used. This difference is probably undetectable for more complex multi-isocenter treatment plans and the significance of this finding as a weakness of the convolution algorithm is debatable because the frame will also be in place at the time of treatment. No significant difference was noted between different pin materials.

Potential dosimetric inaccuracies have been suggested with onyx embolization material and the effect of other embolization agents has not been fully understood (Shtraus et al, 2010). In our study four AVM patients had undergone partial glue embolization and the dose shift with the convolution algorithm in these cases was comparable to subjects who had not had endovascular treatment before GKR. These findings are consistent with the study by Mamalui-Hunter et al who concluded that dose inaccuracy due to attenuation of the ^{60}Co beam by the AVM embolization material was very small for glue (n- butyl 2 cyanoacrytate) and also for Onyx (ethylene vinyl alcohol) because of the high-energy of the ^{60}Co beam (Mamalui-Hunter et al, 2011). No patient in our study had undergone embolization with Onyx and our findings of no increased uncertainty due to previous embolizations apply only to glue.

3.5.3 Head definition with CT

Implementation of the convolution algorithm also involves using CT outlining to define the shape of the head and this results in dosimetric differences of approximately 1.5%. The maximum dose discrepancy due to head shape approximation in our study was 3.4% and comparable results have been reported by other groups (Nakazawa et al, 2014a; Wright et al, 2011). Nakazawa et al reported an average difference of -0.16% between measured and CT-based contours with a maximum difference of 3.4% and concluded it was an acceptable range. The manual method is certainly a practical and convenient approach and the justification of a head CT scan for head definition only is debateable. However, the head is a complex irregular structure and CT outlining can generate a better 3D model. It should be used if a CT scan of the head is available for other clinical reasons or the convolution algorithm is to be used. The uncertainty from head approximation tends to be greater in deep-seated targets and can be foreseen if significant discrepancies are noted on visual evaluation of the head contour.

3.6 Conclusions

Inhomogeneity correction with the convolution algorithm results in a considerable but consistent dose shift compared to the TMR 10 algorithm traditionally used for GKR. No significant difference in relative spatial dose distribution was noted and a reduction of the prescription dose may be necessary to obtain the same absolute dosimetric effect with the convolution algorithm. This study has revealed that dose to the cochlea during GKR is approximately 7% lower than initially predicted with the TMR 10 algorithm and further reduction may be achieved if prescription doses with the convolution algorithm are adjusted. Head shape definition using CT outlining can be used to reduce uncertainty from head shape approximations and CT artefact typically caused by the stereotactic frame, glue embolization material or different fixation pin materials do not systematically affect convolution calculations. Nonetheless, special attention must be given to cases with major CT artefacts around the target where the convolution algorithm may not optimally simulate dose distributions.

4. Evaluation of the stability of the stereotactic Leksell G frame in Gamma Knife Radiosurgery

Rojas-Villabona, A., Miszkiel, K., Kitchen, N., Jäger, R. & Paddick, I.

J Appl Clin Med Phys (2016), 17(3), 75-89.

4.1 Abstract

Introduction: The purpose of this study was to evaluate the stability of the Leksell Frame G in GKR.

Methods: Forty patients undergoing GKR underwent pre-treatment stereotactic MRI for GKR planning and stereotactic CT immediately after GKR. The stereotactic coordinates of four anatomical landmarks (cochlear apertures and the summits of the anterior post of the superior semicircular canals, bilaterally) were measured by two evaluators on two separate occasions in the pre-treatment MRI and post-treatment CT scans and the absolute distance between the observations is reported. The measurement method was validated with an independent group of patients who underwent both stereotactic MRI and CT imaging before treatment (negative controls; n: 5). Patients undergoing GKR for AVM also underwent DSA, which could result in extra stresses on the frame. The distance between landmark localization in the scans for the negative control group (0.63 mm; 95%CI: 0.57 – 0.70; SD: 0.29) represents the overall consistency of the evaluation

method and provides an estimate of the minimum displacement that could be detected by the study. Two patients in the study group had the fiducial indicator box accidentally misplaced at post-treatment CT scanning. This simulated the scenario of a frame displacement, and these cases were used as positive controls to demonstrate that the evaluation method is capable of detecting a discrepancy between the MRI and CT scans, if there was one.

Results: The mean distance between the location of the landmarks in the pre-treatment MRI and post-treatment CT scans for the study group was 0.71 mm (95%CI: 0.68 – 0.74; SD: 0.32), which was not statistically different from the overall uncertainty of the evaluation method observed in the negative control group ($p = 0.06$). The subgroup of patients with AVM (n: 9), who also underwent DSA, showed a statistically significant difference between the location of the landmarks compared to subjects with no additional imaging: 0.78 mm (95%CI: 0.72 – 0.84) vs. 0.69 mm (95%CI: 0.66 – 0.72), $p = 0.016$. This is however a minimal difference (0.1 mm) and the mean difference in landmark location for each AVM patient remained submillimetre.

Conclusions: This study demonstrates submillimetre stability of the Leksell Frame G in GKR throughout the treatment procedure.

4.2 Introduction

GKR has traditionally relied on a rigid immobilization system to stereotactically converge multiple beams of ionizing radiation at a defined intracranial target. The procedure is aimed to eradicate or inactivate the target and the biological effect of the energy delivered is expected to affect all the structures within the volume of the prescribed dose, while minimizing exposure to the surrounding tissue (Sheehan et al, 2014). Therefore, the accuracy of the stereotactic system which encompasses localization of the targets with minimal spatial error and a high degree of reproducibility, is of paramount importance for safe delivery of GKR (Maciunas et al, 1994).

The overall application accuracy of GKR, also referred to as the total clinically relevant error (Maciunas et al, 1994), is the result of individual inaccuracies associated with each step in the procedure and they can be grouped into three categories. First, is the difference between the radiation delivered to the patient and that defined in the treatment plan in terms of magnitude, location or distribution. This can result from errors or approximations in dose calculation or due to mechanical inaccuracy of the treatment delivery itself, which is the estimate of accuracy usually provided by the manufacturers. The second category refers to inaccurate definition of the target which results from erroneous imaging technique selection, inappropriate interpretation of the images or geometrical inaccuracies of the scans due to distortion or other technical factors (Sandstrom et al, 2014). This latter error has been well described and is usually assessed in standard QA procedures (Mack et al, 2002). The third source of error, which is the main scope of this study, is the possibility that the actual location of a target within the stereotactic system at treatment differs from its calculated location due to displacement of the reference frame between the imaging procedure and the treatment. Such displacement could occur from instability due to inadequate frame placement or from stresses induced in the frame between imaging and treatment. This source of error may be more likely to be significant in the case of multiple image studies (e.g., MRI, CT and DSA) and it tends to be overlooked by studies evaluating the accuracy of stereotactic systems by assuming that the frame

is rigid and therefore stable without actively testing it for potential displacements. Also, most studies investigating the stability of fixation systems are laboratory- and phantom-based and standard QA procedures are not capable of detecting potential frame displacement throughout the clinical procedure (Heck et al, 2007).

The most commonly used immobilization and localization method for GKR is the Leksell stereotactic coordinate frame which is a dedicated stereotactic radiosurgery tool introduced by the Swedish Neurosurgeon Lars Leksell in the 1970s and has been further developed over the last few decades (Leksell & Jernberg, 1980). The Leksell G frame was extensively used as a stereotactic tool for brain biopsies before neuro-navigation systems were developed and it is widely used for GKR and insertion of Deep Brain Stimulation (DBS) electrodes (Simon et al, 2005). The later procedure involves localization of very small targets such as the subthalamic nucleus and ventral intermediate nucleus of the thalamus and the level of precision required for such task is comparable to the accuracy required for targeting of the trigeminal nerve in GKR where a few millimetres of error could result in completely missing the target (Massager et al, 2007). This reinforces the importance of actively evaluating the stability of the Leksell frame during GKR, which is the main aim of this study.

4.3 Methods

4.3.1 Patients

Forty consecutive patients undergoing GKR for a variety of intracranial diseases between September 2013 and June 2014 underwent stereotactic MR imaging for GKR planning and stereotactic CT imaging after GKR for research purposes, i.e., evaluation of the convolution algorithm for GKR planning. The study was approved by the research ethics committee (Appendix1) and written consent was received from all participants. The demographic details and diagnosis of the subjects included in the study are shown in Table 4.1.

Table 4.1. Demographic details and diagnoses of the study subjects.

Age mean (min - max)	53.4 y (26 - 76)	
Female, n (%)	23 (57.5%)	
Diagnosis, n (%)	Acoustic neuroma	16 (40%)
	Meningioma	10 (25%)
	AVM	9 (22.5%)
	TN	4 (10%)
	Brain metastases	1 (2.5%)
	Total	40

AVM: Arteriovenous Malformation; TN: Trigeminal Neuralgia

4.3.2 Stereotactic frame and pre-treatment imaging

A Leksell stereotactic coordinate frame G (Elekta AB, Stockholm, Sweden), assembled as shown in Figure 2.2, was used for GKR. The curved front piece was in the upwards position, along with the angled anterior insulated posts (155 mm) and medium straight posts posteriorly (110 mm), which were used in most cases. Three patients had the frame applied with the front piece downwards to avoid nose compression and longer straight posts (137 mm) were used posteriorly on one patient to obtain a lower frame position. Application of the stereotactic frame was performed in a sitting position under local anaesthesia and the frame was manually checked for rigidity before fitting. An injection of 5 ml of lidocaine hydrochloride 1% was given in the planned site of each of the four titanium pins, which were advanced to the outer skull table and adjusted to a consistent pin pressure of 45 cNm using a torque driver.

Stereotactic MRI for GKR planning was performed after frame application and using a Magnetom Avanto 1.5 T MRI system (Siemens AG, Erlangen, Germany). A frame MRI adapter (Elekta AB) was used to support and immobilise the patient's head and stereotactic frame on the MRI table. Post-contrast 3D T1 and T2 weighted volumetric imaging was performed: T1 weighted: FLASH; T2 weighted: CISS; acquisition matrix: 448 x 448; Slice thickness: 1.5 mm, no overlap; FOV: 210 x 210 mm; voxel size: 0.47 x 0.47 x 1.5 mm. The MRI scans were defined in stereotactic space using Leksell GammaPlan 10.1 (Elekta AB) based on fiducial markers obtained from the indicator box (Figure 2.2). An appropriate radiosurgical treatment plan was developed using the aforementioned

planning system and delivered using the Leksell Gamma Knife Perfexion (Elekta AB). Patients undergoing GKR for AVM (n: 9) also underwent DSA for lesion targeting and radiosurgery planning. This invasive procedure involves longer frame-on times and increased patient handling, which could result in extra stresses on the stereotactic frame and a potentially higher risk of frame displacement.

4.3.3 Post-treatment imaging and landmarks measurement

A post-GKR stereotactic non-contrast CT of the head was performed immediately after treatment and prior to frame removal using a Siemens Somatom Definition AS multislice helical CT scanner (Siemens AG, Forchheim, Germany). Acquisition matrix: 512 x 512; Slice thickness: 1.5 mm, no overlap; FOV: 240 x 240 mm; pixel size: 0.47 x 0.47 mm. A frame CT adapter (Elekta AB) was used to secure the patient in the correct position and the scans were independently defined in stereotactic space using fiducial markers from the CT indicator box.

The stereotactic coordinates of four landmarks were measured in the pre-treatment MRI and again in the post-treatment CT scans by two different evaluators on two separate occasions with at least one week's difference between repeated measures. Figure 4.1 shows the landmarks used for evaluation; bilateral cochlear apertures, at the base of the modiolus, and the summits of the anterior post of the superior semicircular canals (SSC). The landmark coordinates in the pre-treatment MRI scan were taken from the T2 weighted images and from the bone reconstruction on the post-treatment CT scan as shown in Figure 4.1. The stereotactic coordinates of the cochlear apertures were measured in the axial plane. In two study cases, one of the cochlear apertures was bisected by two slices and this resulted in discrepancies in the *z* coordinate reflecting the slice thickness rather than the apparent location of the landmark. A consensus was reached between the observers for these two cases and measurements were obtained from the same slice. To minimize the effect of slice thickness on the results, the stereotactic location of the SSC was taken from the reconstructed coronal plane. The distance between the stereotactic location of the landmarks observed in the pre-treatment MRI scan and the post-treatment CT scan was measured.

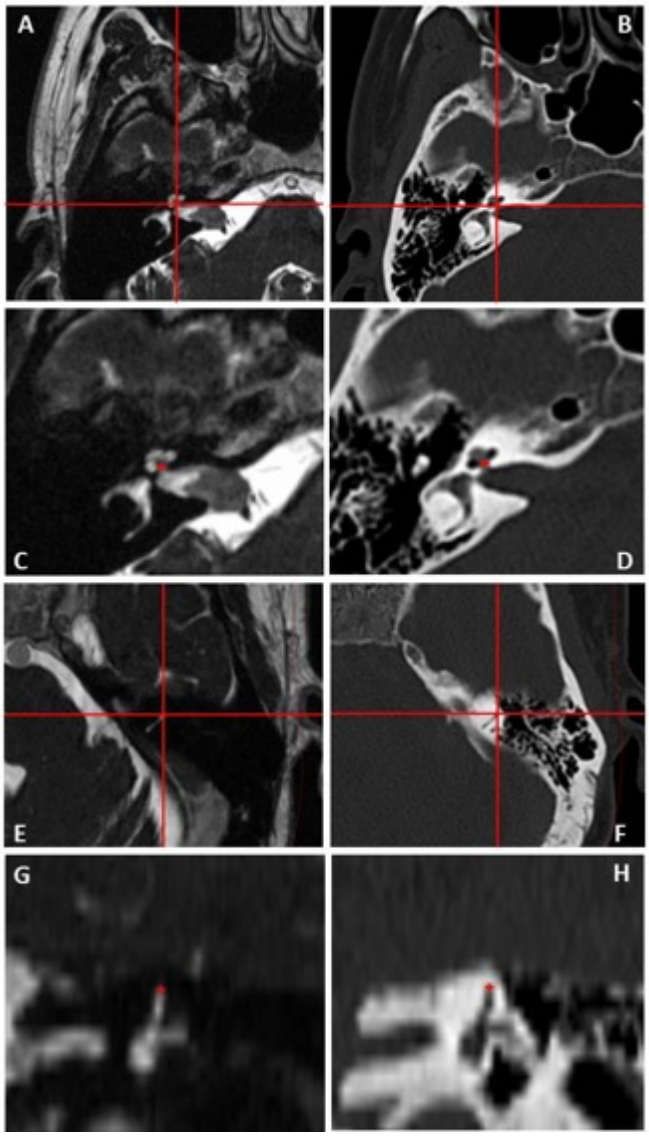

Figure 4.1. Landmarks used for frame stability evaluation. The landmarks as seen in the T2 weighted sequence of the pre-GKR MRI scan are showed in the left panel. The right panel shows the same landmarks in the bone window of the post-treatment CT scan. A-B: Right cochlear apertures are identified by the intersection of the lines. C-D: A detail shows the red cross on the landmark as measured for the study. E-F: Initial identification of the anterior post of the left superior semicircular canal in the axial plane (line intersection) and its summit as identified in the coronal plane (red cross; G-H).

4.3.4 Data analysis

The mean distance between the first and second session measurements by the same observer was used to evaluate intra-observer agreement. Inter-observer agreement was assessed comparing measurements between the observers for each landmark localization attempt.

The distance between two points in the Euclidian space was calculated using the equation below:

$$d(A,B) = \sqrt{(Ax - Bx)^2 + (Ay - By)^2 + (Az - Bz)^2} \quad (1)$$

Validation of the measurement method was performed with an independent group of subjects (n: 5) who had undergone both stereotactic MRI and CT imaging before GKR. CT scanning is not routinely used for radiosurgery planning in our centre but it is used selectively for targets near bone structures where target definition can be aided by CT imaging. This was the reason for the clinical stereotactic CT scan before GKR in these subjects and it provided an estimate of the overall variability of the evaluation method in terms of uncertainty of landmark localization between two different imaging techniques (negative controls). The mean time interval between the beginning of the MRI scan and the CT scan in this group was 37.8 min (14 - 73 min). As there were no treatment-related stresses applied to the frame between MRI and CT scanning in this group, it was assumed that no frame displacement had occurred in these patients.

The mean distance between the location of the landmarks in the MRI and CT scan was calculated and reported for each patient to combine multiple observations of the landmarks. The individual localization attempts were used for evaluation of differences between the groups and logarithmic transformation of the distance data was done to enable comparison between the groups using independent sample's t-test. Data analysis was performed using the Statistical Package for the Social Sciences (SPSS Statistics, Version 23. IBM Corp).

4.4 Results

The mean frame-on time defined as time difference between the beginning of the pre-GKR MRI and post-GKR CT scan in the study subjects was 157.8 minutes (89 - 298). Two patients in the study group, one of them undergoing GKR for AVM, had the CT fiducial indicator box accidentally misplaced at post-GKR CT scanning and this resulted in a considerable mismatch between the location of the landmarks in the MRI and CT scans in these two subjects (cases 13 and 17). As shown in Figure 4.2, the right posterior locating pin of the fiducial indicator box was not seated in the corresponding hole in the frame ring but it was displaced towards the midline allowing the box to rest on the frame, and the lateral clips to be secured, in an apparently normal position. The centre of the locating pin was misaligned by 7.5 mm from its normal position in both cases. This error was detected during definition of the CT scans in stereotactic space which yielded mean and maximum fiducial errors of 1.6 and 4.6 mm respectively. As expected, the discrepancy in the location of the landmarks between the scans was more evident on the right side and mainly affected the *x* axis. The mean distance between the location of the landmarks in the pre-treatment MRI and post-treatment CT in these two patients was 1.46 mm and the maximum difference noted was 2.24 mm. These two cases accidentally simulated the scenario of a frame displacement and they were used as a positive control group for comparison. They were therefore excluded from the main study group, which was composed of 38 patients.

The fiducial error estimates of definition of T2 weighted MRI and CT scans in the stereotactic space for the main study group are shown in Table 4.2. As expected, the mean fiducial error of MRI scans (0.44 mm) was slightly larger than for CT scans (0.26 mm). Measurement of the position of the four landmarks was successfully accomplished in all but two patients. These were a subject with an AVM whose left cochlea was not included in the scan and a patient with a left sided vestibular schwannoma who had undergone previous trans-labyrinthine excision of the tumour and the SSC was not visible.

Table 4.2. Fiducial error in stereotactic definition of MRI and CT scans for the main study group. The pre-treatment T2 weighted MRI scan and post-treatment CT scan (bone window) were independently defined in the stereotactic space using GammaPlan. Fiducial errors in the definition process for 38 patients included in the study group are summarized.

Study group (n:38)	**Pre-GKR MRI scan T2 weighted**	**Post-GKR CT scan bone window**
Mean error (95%CI) SD	0.44 mm (0.42 - 0.46) 0.06	0.26 mm (0.23 - 0.29) 0.09
Maximum error (95%CI) SD	1.09 mm (1.05 - 1.13) 0.13	0.71mm (0.63 - 0.79) 0.24

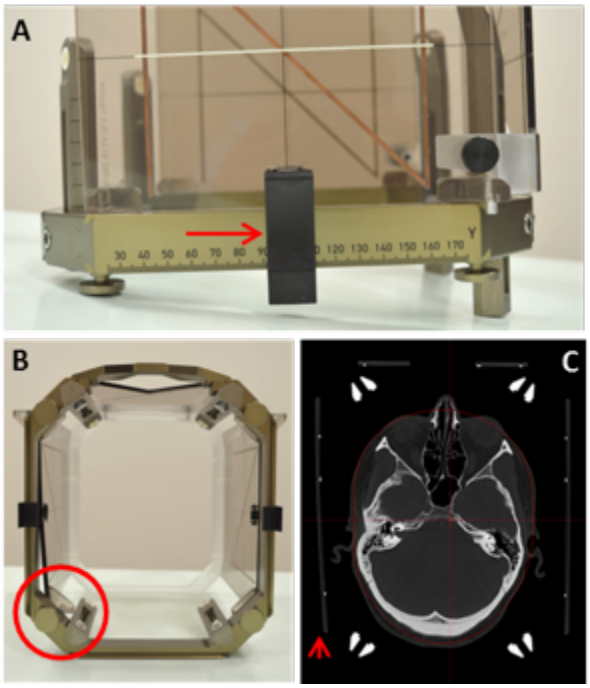

Figure 4.2. Fiducial indicator box accidentally misplaced at post-GKR CT scan. A. Lateral view of the stereotactic frame with the CT fiducial indicator box in an apparently normal position with the lateral clip adequately secured (red arrow). B. An inferior view of the frame shows the right posterior locating pin of the indicator box displaced towards the midline (red circle) that resulted in an erroneous position of the fiducials in the CT scan (C, arrowhead).

The total number of coordinate measurements was 4272 as follows: 45 (subjects) x 4 (landmarks) x 2 (observers) x 2 (repeated measurements) x 2 (MRI and CT scans) x 3 (x, y, z) - 48 coordinate measurements for the two missing landmarks as mentioned above. These measurements were obtained from three groups of patients, i.e., five subjects with both scans done before GKR and no plausible frame displacement (negative controls), two cases with misplaced indicator boxes at post-GKR CT simulating a frame displacement (positive controls) and the main group of patients under investigation who underwent MRI scan before and CT scan after GKR (study group: 38). Table 4.3 shows the estimates of variability between repeated measurements by the same observer on the same scans (intra-observer variability) and between the observers (inter-observer variability) in the three groups. Repeated measurements by the same observer on the same scans were consistent across the groups with a mean distance between the first and second measurement of 0.25 mm. These estimates were similar for measurements obtained from CT (0.25 mm; 95%CI: 0.23 - 0.27) and MRI scans (0.24 mm; 95%CI: 0.22 - 0.26), p = 0.3. The mean distance between measurements of the same landmark by different observers in the study group was higher at 0.59 mm (95%CI: 0.57 - 0.61).

Table 4.3. Intra-observer and inter-observer variability of the measurements. Negative controls: patients who underwent both MRI and CT scans before GKR; Positive controls: two patients with an accidentally misplaced fiducial indicator box at post-GKR CT scanning (simulating a frame displacement); Study group: main group of subjects under investigation who underwent MRI scanning before and CT imaging after GKR (n: 38); n: number of subjects; obs: number of observations.

	Intra-observer variability **mean distance, mm (95%CI)** **SD; max**	**Inter-observer variability** **mean distance, mm (95%CI)** **SD; max**
Negative controls n: 5; obs: 80	0.25 mm (0.22 - 0.29) 0.16; 0.70	0.41mm (0.34 - 0.47) 0.26; 1.14
Positive controls n: 2; obs: 32	0.21 mm (0.17 - 0.25) 0.12; 0.45	0.57 mm (0.47 - 0.67) 0.26; 1.14
Study group n:38; obs: 600	0.25 mm (0.23 - 0.26) 0.17; 1.14	0.59 mm (0.57 - 0.61) 0.27; 1.31

The difference between the location of the landmarks in the MRI and CT scans for the three groups is shown in Table 4.4. The distance observed in the negative control group (0.63 mm; 95%CI: 0.57 - 0.70; SD: 0.29) represents the overall consistency of the evaluation method and provides an estimate of the minimum displacement that could possibly be detected by the study. The positive control group with a mean distance between the location of the landmarks in the MRI and CT scans of 1.46 mm (maximum difference of 2.24 mm), demonstrates that the evaluation method is capable of detecting a discrepancy between the MRI and CT scans if there was one.

The mean distance between the location of the landmarks in the pre-GKR MRI and post-GKR CT scans for the study group was 0.71 mm (95%CI: 0.68 - 0.74; SD: 0.32). The mean difference for each individual patient was below 1 mm. The estimates of difference between the MRI and CT coordinate measurements in the study group were consistent across the landmarks, i.e., cochleae: 0.71 mm (95%CI: 0.67 - 0.75) vs. 0.70 mm (95%CI: 0.67 - 0.74) for the SSC measurements, $p = 0.99$.

There was no correlation between frame-on time and the difference between the MRI and CT coordinate measurements in the study group (Spearman's correlation coefficient: -0.03; $p = 0.4$) and this is shown in Figure 4.3 for each of the landmarks analysed.

The group of patients with AVM, who also underwent DSA and so were subject to longer frame-on times and additional frame stress events, showed slightly larger estimates of difference between the location of the landmarks compared to subjects with no additional imaging in the study group, 0.78 mm (95%CI: 0.72 - 0.84) vs. 0.69 mm (95%CI: 0.66 - 0.72), $p = 0.016$. This is however a minimal difference (0.1 mm) and the mean difference in landmark location for all AVM patients remained submillimetre.

Table 4.4. Distance (mm) between the location of the landmarks in the MRI and CT scans. The negative control group had both MRI and CT scans before GKR. The fiducial indicator box was accidentally misplaced at post-GKR CT scanning in two cases (positive controls), simulating a frame displacement. The study group underwent MRI scanning before and CT imaging after GKR (n: 38). Subjects in the AVM group also had DSA for radiosurgery planning which involves longer frame-on times and additional frame stress events.

Group	**Distance in landmark location MRI – CT** **mean distance, mm (95%CI)** **SD; max**
Negative controls n:5; obs: 80	0.63 (0.57 - 0.70) 0.29; 1.36
Positive controls n:2; obs: 32	1.46 (1.36 - 1.56) 0.28; 2.24
Study group n:38; obs: 600	0.71(0.68 - 0.74) 0.32; 1.76
Study group excluding AVM n: 30; obs: 476	0.69 (0.66 - 0.72) 0.31; 1.76
AVM only n:8; obs: 124	0.78 (0.72 - 0.84) 0.34; 1.75

n: number of subjects, obs: number of observations.

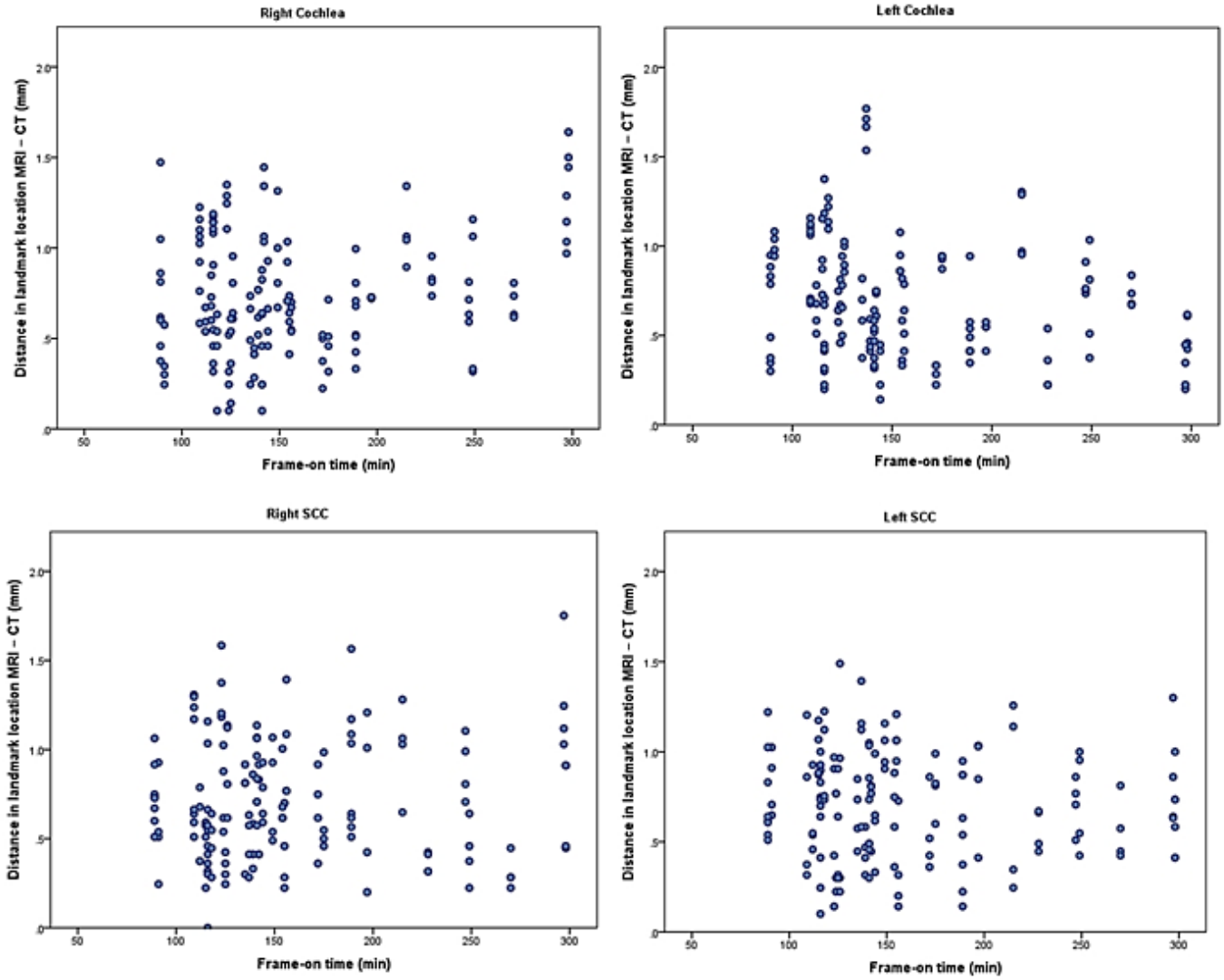

Figure 4.3. Difference between the MRI and CT coordinate measurements versus frame-on time in the study group for each of the landmarks analysed. No correlation is seen between the frame-on time and the estimated difference between the MRI and CT coordinate measurements for the cochlea and SCC bilaterally.

As shown in Figure 4.4 the distribution of the distance between the location of the landmarks in the MRI and CT scans for the negative control and the study groups are similar and no statistical difference was noted between these groups (p = 0.06). The maximum difference observed between the location of the landmarks in the MRI and CT scans for the negative control group was 1.36 mm. Outlier values in the study group above 1.5 mm were considered beyond the maximum uncertainty justifiable by the slice thickness and underwent further review.

Ten pairs of MRI-CT measurements in the study group, out of a total of six hundred, differed by more than 1.5 mm. Four of these outliers were observed in the left cochlea of a single patient by both observers on both occasions (case 33). This patient presented the maximum difference noted in the study group (1.76 mm) but no similar difference was noted in the measurements of the ipsilateral SSC or the contralateral landmarks. Similarly, three outliers were observed in the right cochlea of a second subject by both observers, in two occasions by one of them, but again no large difference was noted in the ipsilateral SSC or the contralateral landmarks (case 20). A thorough review of these datasets demonstrated a discrepancy between the MRI and CT imaging planes which resulted in an overestimation of the difference in the z axis, comparable to the 1.5 mm slice thickness. As shown in Figure 4.5, the CT slices bisected the cochlea at two levels, one closer to the top and the second closer to the bottom, rather than at the middle where the cochlear aperture would have been better visualized. This resulted in the landmark being measured at two different levels in the MRI and CT scans. The three remaining outliers were isolated inconsistencies measured by a single observer, in a single landmark and in three different patients (cases 22, 23 and 46). These were also detected in only one of the two measurements made by the same observer and were considered genuine observer errors.

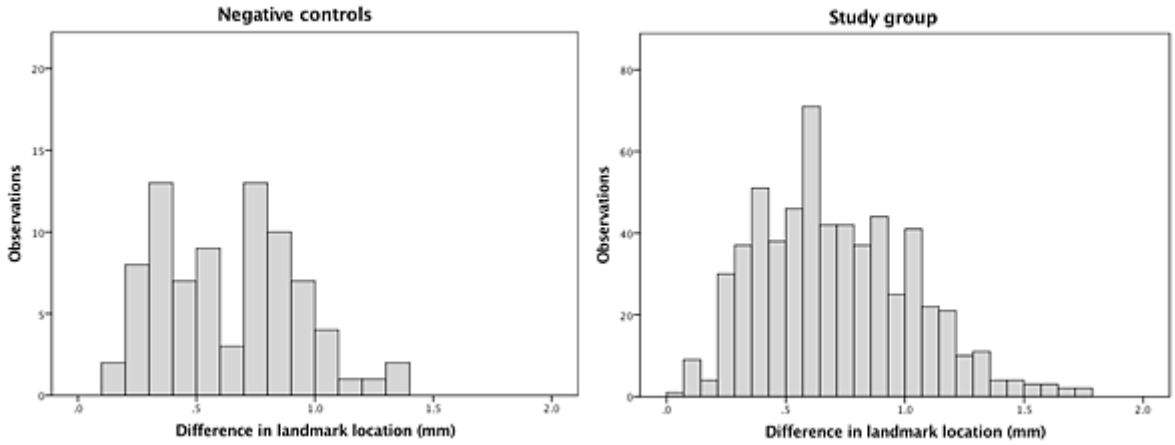

Figure 4.4. Distribution of the distance (mm) between the location of the landmarks in the MRI and CT scans for the negative controls and the main study group. Negative controls (left) underwent both MRI and CT scans before GKR. Study group (right) were main group of subjects under investigation who underwent pre-treatment MRI scanning and CT imaging after GKR.

4.5 Discussion

This study aimed to evaluate a commonly overlooked factor contributing to the global accuracy of GKR. It is the assumption that the stereotactic frame stays still during the treatment procedure and does not move. The location of four defined landmarks were measured in the planning MRI scan and compared to their observed position in a CT scan acquired immediately after treatment. If the stereotactic frame was completely stable and it was possible to measure the position of the landmarks in the two scans without any uncertainty, the difference between the first and second observations would have been zero. This was not the outcome of the study. A quantifiable difference of 0.71 mm (95%CI: 0.68 - 0.74; SD: 0.32) between the position of the landmarks in the pre-GKR MRI and the post-GKR CT scan was observed. This difference reflects the effect of three elements of the evaluation process i.e., the variability of the measurements within and between the observers, the uncertainty of the imaging techniques used for the study and a potential degree of frame displacement. These factors were quantified

in an independent group of subjects (negative controls) who underwent both scans before GKR with minimal time and frame stress events between them. The mean difference between the location of the landmarks in the MRI and CT scans in this group was 0.63 mm (95%CI: 0.57 - 0.70; SD: 0.29). This is considered to be the best estimate of values with no frame displacement under the research conditions and provides a threshold of minimum displacement that could have possibly been detected by our study.

The difference observed in the study group (0.71 mm; 95%CI: 0.68 - 0.74; SD: 0.32) was not statistically different to the overall uncertainty of the evaluation method as observed in the negative control group (0.63 mm; 95%CI: 0.57 - 0.70; SD: 0.29). It is not possible to assert that frame displacement was zero because the difference found in the study group is equivalent to the uncertainty of the measurement method. It is also not possible to estimate from the study how much of the submillimetre difference observed in the study group is potentially explained by frame displacement. It can, however, be confidently concluded that no systematic frame displacement larger than 0.71 mm occurred in the study group.

4.5.1 Intra and Inter-observer variability

The variability of the measurements in our study is one of the factors contributing to the overall uncertainty of the results. The mean distance between repeated measurements by the same observer was 0.25 mm and as expected a larger mean distance was noted between measurements by different observers (0.59 mm). These estimates reflect not only the individual skills of the observers but also the size and nature of the landmarks which should be sensitive to potential frame displacement but also reliably identifiable in the scans. The cochlear apertures and the summit of the anterior post of the SSC were thought to be good landmarks for the study because they are non-midline structures sensitive to potential rotational displacement of the frame, they are clearly visible in both CT and T2 weighted MRI scans and small enough in size for their location to be acceptably summarized by a single set of *x*, *y* and *z* coordinates. There is however a degree of

imprecision in using a single point to define the location of a three-dimensional structure.

The uncertainty of the coordinate measurements also derives from the fact that a landmark could be bisected by the scan slices at two different levels. The resultant discrepancy reflects the arbitrary quantization of the imaging planes rather than the exact position of the landmarks in the stereotactic system. The location of the SSC was measured in the coronal plane to minimise this source of error and also a consensus was reached between the observers in two cases where one of the cochlear apertures was bisected by two different slices. This however, applied only to measurements obtained from the same scan and it was not possible to adjust for slice misalignment when comparing the position of the cochlea (as measured in the axial plane) between two different scans. This error was particularly obvious in two of our study group patients where one of the cochleae was bisected at two levels by the post-GKR CT scans (Figure 4.5). This resulted in coordinate values being obtained from different anatomical structures due to suboptimal visualization of the landmark in the scans. The distance noted between these outlier observations was between 1.5 and 1.76 mm and this clearly reflects the slice thickness. No such difference was noted in the ipsilateral SSC of the same patients, which was measured in the coronal plane or the landmarks in the contralateral side. This reinforces the evidence that the outliers in our study are caused by the arbitrary slice misalignment between the scans rather than a displacement of the stereotactic frame. This would have been reduced if thinner slices were used for the imaging procedure. The coronal MRI and CT planes, reformatted from the axial images have an effective slice thickness of 0.47 mm (voxel dimensions: 0.47 x 0.47 x 1.5 mm) and this has a lesser effect for localisation of the SSC in the coronal plane. The cochleae, however, were not considered less suitable landmarks for comparison and their difference in apparent location between the MRI and CT scans was found to be comparable to the same estimates with the SCC (cochleae: 0.71 mm, 95%CI: 0.67 - 0.75 mm; SCC: 0.70 mm, 95%CI: 0.67 - 0.74 mm, $p = 0.99$).

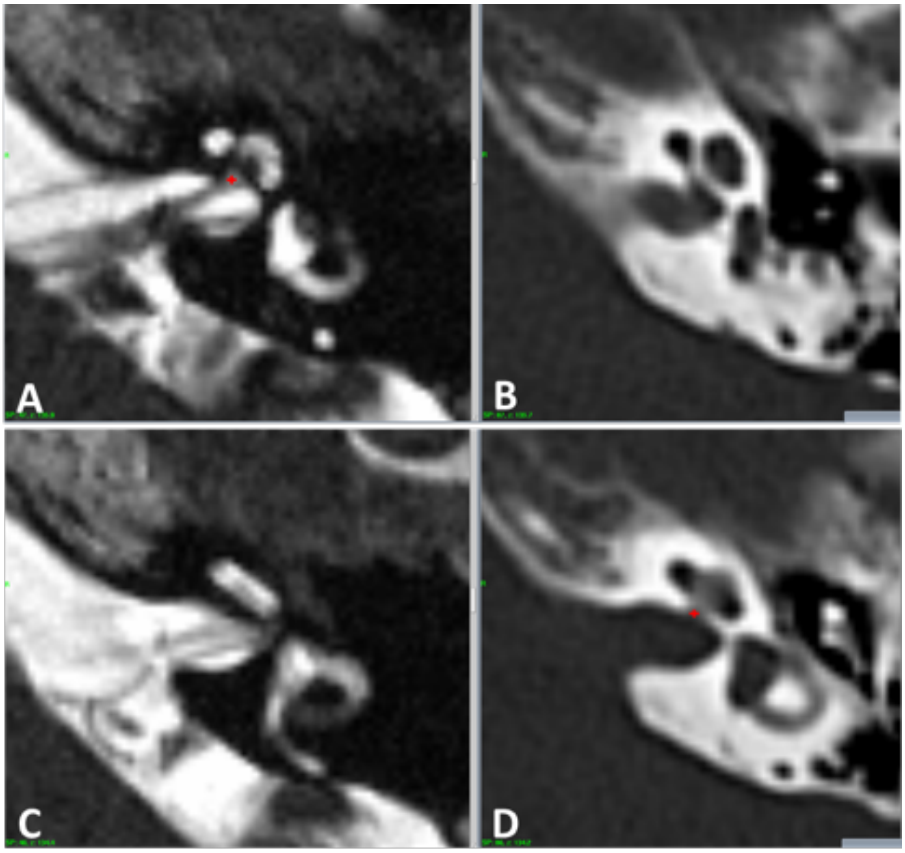

Figure 4.5. Discrepancy between MRI and CT imaging planes causing overestimation of the difference seen in the outliers (case 33). A. The red cross shows an acceptable coordinate measure of the location of the cochlea in the pre-GKR MRI scan (*x*, *y*, *z*: 127.1, 99.5, 135.9). The next MRI slice does not show the cochlear aperture (C). The images in the right show the cochlea bisected at two levels by the CT scan, one closer to the top (D) and the second closer to the bottom of the cochlea (B). The CT measurements for the study (*x*, *y*, *z*: 127.6, 99.5, 134.2) were taken from the superior slice (D) overestimating the difference in the *z* axis by the same magnitude as the slice thickness.

4.5.2 Localization uncertainty due to imaging techniques

The validity of the conclusions reached by this study rest on the assumption that it is possible to reliably identify the same landmarks in two different imaging techniques i.e., MRI and CT. Figure 4.1 demonstrates the high-quality visualization of the landmarks in both images. Nonetheless, technical factors inherent to the imaging technique will introduce some uncertainty to the localization coordinates. MRI distortion is the most significant of these factors and was recently characterised by Nakasawa et al. They demonstrated that the maximum absolute error of coordinates in each dimension using 1.5 T MRI and the Leksell G frame with titanium fixation screws is between 1 and 2 mm (Nakazawa et al, 2014d). This is considerably higher than the estimate of distortion of the MRI unit used in our study which was found to be a mean of 0.46 mm and a maximum of 0.88 mm using a GRID3D known target phantom (Modus Medical Devices Inc. London, Canada). For our CT scanner, a mean of 0.41 mm and a maximum of 0.70 mm was measured with the same phantom. Combining the errors for these two modalities in quadrature yields mean and maximum errors of 0.62 mm and 1.12 mm respectively. This mean error is remarkably close to the mean difference in the negative controls group, adding weight to our assumption that the negative controls group is a valid estimate of our uncertainties.

The uncertainty caused by imaging distortion contributes to the apparent differences in landmark positions seen between the MRI and CT scans in some cases where the same stereotactic point seems to show a slightly different anatomical position in the scans (Figure 4.6). This phenomenon has been described by Karlsson et al who reported a mismatch above 1.5 mm between two stereotactic MRI scans of the same subject and concluded it was the result of MRI distortion artefact (Karlsson et al, 2011). Pollock et al has also reported the importance of MRI distortion in stereotactic radiosurgery planning and sugested that imaging distortion could have partly caused some of their recurrent vestibular schwannomas to receive less than the prescribed dose to the entire tumour volume (Pollock et al, 2009). This is also relevant to our outlier measurements observed in

the cochlea where CT imaging is likely to better characterise the anatomy of the bony structure compared to MRI.

Further testing of the measurement method was possible in our study due to unintentional misplacement of the CT indicator box in two cases (positive controls). The simulated displacement was evidenced in the coordinate measurements as a mean difference between the position of the landmarks in the MRI and CT scans of 1.46 mm (95%CI: 1.36 - 1.56). The maximum discrepancy observed was 2.24 mm, which is considerably larger than the maximum observed difference in the study group. This error was effectively detected by GammaPlan (Elekta AB) and the planner was made aware of this through unusually high fiducial errors during the stereotactic definition of the CT scans. This would not have been the case if a real frame shift occurred because there is currently no mechanism in place to detect such a displacement throughout the treatment procedure. The development of the Leksell Gamma Knife and its integration with movement tracking and live image guidance systems in the recently launched Gamma Knife Icon is expected to address potential geometric inaccuracies throughout the treatment procedure (Ruschin et al, 2013).

The scenario of a misplaced indicator box is clearly geometrically simpler than a multiplane or rotational frame displacement but it can provide some understanding of the degree of error that would be added to a treatment if the stereotactic frame displaced. In the two cases with a misplaced indicator box in our study the right posterior locating pin of the fiducial indicator box was displaced 7.5 mm towards the midline and the maximum error of the scan definition process was 4.6 mm. However, the maximum discrepancy observed between the location of the landmarks in the MRI and CT scans was only 2.5 mm, considerably lower than the potential error in the system. This reduction of error is caused by a redistribution of the inaccuracies across the scans when they are defined in stereotactic space (Jones, 1993). Similar benign error redistribution effects could occur if the frame displaced under specific conditions such as axial rotation with a centrally located target and this study did not specifically address the issue of potential rotational displacement of the frame. Further understanding

of the effect of random geometrical uncertainties in the treatment procedure is needed to fully comprehend the clinical effect of potential frame displacement and also for evaluation and development of frameless radiosurgery systems (Schlesinger et al, 2012; Walton et al, 2002).

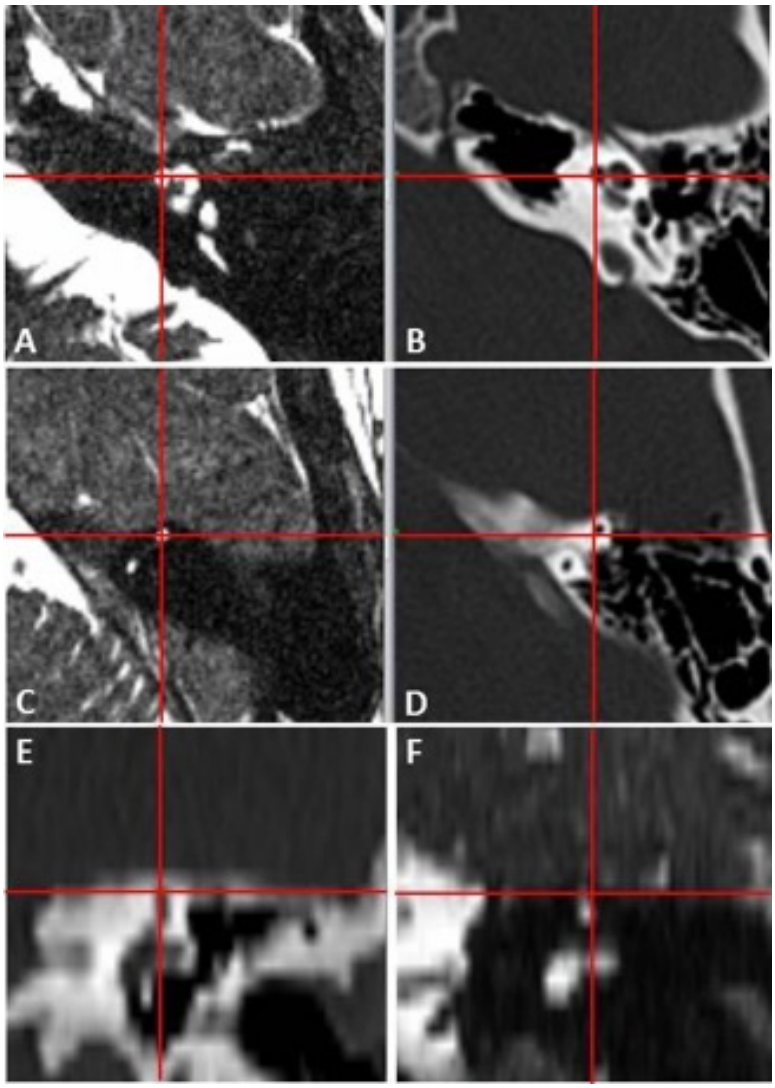

Figure 4.6. Submillimetre discrepancies between the location of the landmarks in the MRI and CT scans attributed to imaging distortion. The red lines cross in the centre of the cochlear canal at the most medial spiral turn in the pre-GKR MRI scan (A) but slightly off-centre in the post-GKR CT scan (B). Similar discrepancies between 0.5 and 1 mm were seen in the axial view (C and D) and coronal view (E and F) of the SCC (case 16).

4.5.3 Frame stability

Karlsson et al evaluated the stability of the Leksell frame in a group of 18 patients who underwent high-definition MRI scans before and after GKR. The reported mean distance between the average of repeated readings of the location of defined landmarks before and after GKR was 0.47 mm and it was concluded that the position of the stereotactic frame is stable throughout the treatment procedure (Karlsson et al, 2011). The difference reported by Karlsson et al is considerably lower than that observed in our study and this is explained by the methodological differences. The comparison between the pre and post-GKR scans in their study was done using the calculated mean of repeated observations (mean position of localization), rather than each individual localization attempt, and this could result in erroneously favourable outcomes (Maciunas et al, 1994). Also, we used a different imaging technique before and after GKR and the imaging slices were also thicker in our study (1.5 vs. 0.7 mm), which explains the increased uncertainty of our measurements.

The application accuracy of four commonly used stereotactic devices, including the Leksell frame, was challenged by Maciunas et al in an attempt to evaluate the total accuracy conveyed by the entire visualization, calculation and surgical systems working together (Maciunas et al, 1994). The study suggested a significant degree of error in the application accuracy of all the stereotactic instruments tested but failed to specifically address the question of stability of the frame itself. Their experiment compared the true location of a target in a phantom with the position reached by a needle tip if the target coordinates were set in the stereotactic arc system. This comparison was performed several times using different CT slice thickness and the mean error was found to be within 1 – 2 mm when 1 mm slices were used and within 2 – 3 mm with 4 mm slices. These estimates of inaccuracy are considerably larger than the observed mean difference in our study and only our outliers are somewhere near the best results by this group. This is probably due to the fact that the findings of the Maciunas study relied on the poor geometric accuracy of earlier generation CT scanners, which are now known to yield errors of a few mm (Yu et al, 2001). The experiment

designed by Maciunas et al cannot be used as evidence against the stability or accuracy of the Leksell G frame; however, it provides awareness of how slice thickness can influence the overall accuracy of stereotactic systems.

4.5.4. Effect of frame weight bearing on the stereotactic frame

The paper by Maciunas et al also claimed to evaluate the effect of frame weight-bearing on the accuracy of the stereotactic systems and concluded that a mean displacement of 1.62 mm occurs if a weighting of 25 Kg is added to the Leksell G frame. This is a significant weight unlikely to represent any clinical scenario and it is not possible to determine from the study report how the Leksell frame was fixed to the phantom's acrylic plastic base. Their results are more likely to reflect a technical fault on the specific experimental design rather than any clinically relevant instability of the frame. Nevertheless, the issue of frame weight bearing has not been fully addressed in the literature and our study provided the opportunity to compare a group of AVM patients, with additional frame stress events incurred in the process of DSA, and a group of subjects who were not exposed to these factors. The results demonstrated that the difference between the location of the landmarks in the pre- and post-treatment scans is slightly higher in the AVM patients, who were subject to longer frame-on times and additional frame stress events, compared to other subjects in the study group who underwent no additional imaging (0.78 mm vs. 0.69 mm; $p = 0.016$). The difference between these two groups, although very small in magnitude (0.1 mm), is statistically significant and it may be beneficial to reduce the number of frame stress events during the treatment procedure. This may also have implications for patients who are treated using trunnion fixation on Gamma Knife model B and C where patient frames are repeatedly stressed during docking for each isocenter.

4.6 Conclusions

A comprehensive study design involving repeated measurements of the landmarks in forty patients by two observers, along with validation of the evaluation method in an independent negative control group with no plausible frame displacement,

demonstrated that the observed difference in the study subjects is equivalent to the overall uncertainty of the evaluation method. This provides reliable and realistic evidence of submillimetre stability of the stereotactic frame throughout the treatment procedure.

5. Can Gamma Knife Radiosurgery for brain arteriovenous malformations be planned on triple Magnetic Resonance Angiography?

Rojas-Villabona, A., Sokolska, M., Solbach, T., Grieve, J., Rega, M., Torrealdea, F., Benedetta Pizzini, F., Suzuki, Y., Van Osch, M., De Vita, E., Biondetti, E., Shmueli, K., Atkinson, D., Murphy, M., Paddick, I., Golay, X., Kitchen, N. & Jager, R.

Under peer review for publication

5.1 Abstract

Introduction: GKR is a well-established minimally invasive treatment for selected cases of intracranial AVMs. State-of-the-art planning strategy involves intra-arterial Digital Subtraction Angiography (DSA) on the day of treatment for delineation of the radiosurgical target, as well as standard volumetric MRI scans. However, DSA is invasive and it carries a potential risk of peri-procedural complications. This study aims to evaluate whether a combination of three Magnetic Resonance Angiography sequences (triple-MRA), could be used as an alternative to DSA for delineation of brain AVMs for GKR targeting.

Methods: Fifteen patients undergoing DSA for targeting of GKR for brain AVMs also underwent triple-MRA including: 4D arterial spin labelling based angiography (ASL-MRA), high definition time-of-flight angiography (HD-TOF)

and contrast-enhanced time-resolved MRA (CE-MRA). ASL-MRA acquisition was individualised in each case based on the filling velocity of the AVM and for this reason, triple-MRA scanning time varied among patients between 19:05 and 25:33 minutes.

The arterial phase of the AVM nidus, excluding draining veins, was delineated on triple-MRA and volumetric post-contrast T1 and T2 weighted MRI by an interventional neuroradiologist and a consultant neurosurgeon (triple-MRA volume). This was achieved by including the areas shown to be part of the AVM nidus in all three MRA techniques as well as standard volumetric MR imaging. Triple-MRA volumes were compared to the AVM target delineated by the GKR clinical team for delivery of radiosurgery using the current planning paradigm, i.e. stereotactic DSA and volumetric MRI (DSA volume). Difference in size, degree of inclusion (DI) and concordance index (CcI) between DSA and triple-MRA volumes were calculated.

Results: The mean DSA volume was 3.89 ml (95%CI: 1.95 - 5.82 ml; median: 3.35 ml; range: 0.1 - 10.77 ml). AVM volumes delineated on triple-MRA were significantly smaller at 3.49 ml (95%CI: 1.77 - 5.2 ml; median: 2.88 ml; range: 0.09 - 9.89 ml), (p = 0.003), and were smaller than the DSA volume in all but once case (93%). The relative difference between DSA and triple-MRA volumes was on average 9.8% (95%CI: 5.6 - 13.9%; SD:7.14%; median: 10.5%; range: -7.3 - 18.7%).

DI of DSA volume in triple-MRA volume was on average 73.5% (95%CI: 71.2 - 76; median: 73%; range: 65 - 80%). The mean percentage of triple-MRA volume not included on DSA was 18% (95%CI: 14.7 - 21.3; median: 18.4%; range: 7 - 30%). The mean CcI was 0.63 (95%CI: 60.4 - 66.2; median: 0.63; range: 0.51 - 0.72).

Conclusion: The technical feasibility of using triple-MRA, instead of DSA, for delineation of brain AVMs for GKR targeting has been demonstrated. Target volumes obtained using triple-MRA are on average 10% smaller than AVM targets obtained with the standard DSA planning method and this can potentially

reduce the risk of ARE. The discrepancies observed between triple-MRA and DSA volumes are less than the inter-observer variability observed when an AVM target is delineated by different radiosurgical teams.

5.2 Introduction

GKR is a well-recognized non-invasive treatment option for selected cases of brain AVMs (Pollock et al, 2016; Starke et al, 2017). The treatment is aimed at eliminating the risk of intracranial haemorrhage by obliterating the AVM, with minimal injury to surrounding normal brain tissue (van Beijnum et al, 2011). This is achieved by stereotactically delivering a high and greatly localized radiation dose to the AVM nidus, which is the network of coiled and tortuous blood vessels that abnormally connect arteries and veins and cause arteriovenous shunting in AVMs (Leksell, 1983; Seymour et al, 2016). Obliteration after radiosurgery occurs gradually over a two to three years period and success rates between 65 and 85% have been reported (Hamm et al, 2008; Kano et al, 2012b; Koltz et al, 2013). GKR, like other forms of radiosurgery, relies on the quality and accuracy of imaging used for treatment planning and delivery. It is well accepted that higher obliteration rates and less complications are achieved when inclusion of the entire AVM nidus is accomplished and draining veins are excluded from the treatment volume (Safain et al, 2014).

Intra-arterial cerebral DSA has historically been the main imaging modality used for radiosurgery target delineation in AVM radiosurgery, and it is still considered the reference standard technique for AVM identification and characterisation (Pollock et al, 2017; Starke et al, 2017). Stereotactic DSA, which is performed on the day of treatment, alongside volumetric MR and/or CT imaging, enables high resolution, dynamic and vessel selective imaging of the cerebral vasculature (Seymour et al, 2016). However, DSA data integrated into the GKR planning system consist of two-dimensional (2D) projections in the coronal and sagittal planes and do not contain 3D information (Taschner et al, 2007). DSA also has a small but definite risk of neurological complications related to thromboembolic events. This lies between 0.3% and 2.63% per examination and is known to increase when multiple DSA procedures are performed, which is often the case in the AVM population (Dawkins et al, 2007; Fifi et al, 2009; Kaufmann et al, 2007; Leffers & Wagner, 2000). Silent embolic events are also found on diffusion weighted MRI in up to 23% of the patients after DSA (Bendszus et al, 1999) and

severe complications such as stroke with permanent disability (0.14%) and death (0.06%) have been reported (Kaufmann et al, 2007). In addition, DSA exposes both patients and medical staff to ionizing radiation, it carries the risk associated with injection of iodinated contrast agents and it is an unpleasant experience for patients due to pain, invasiveness and prolonged bed rest after the procedure (Fifi et al, 2009).

Several studies have previously attempted to use alternative techniques for AVM radiosurgery targeting with varying degrees of success (Amponsah et al, 2012; Bednarz et al, 2000; Buis et al, 2007; Hamm et al, 2008; Kang et al, 2014; Nagaraja et al, 2005; St George et al, 2002; Taschner et al, 2007). Time-of-flight angiography (TOF) has been shown to increase the accuracy of AVM radiosurgery targeting (Bednarz et al, 2000) and as a result some GKR units have added TOF to their planning algorithms as a complementary imaging modality to DSA. CT angiography has also been shown to aid DSA based radiosurgery planning; however, it potentiates the limitations of DSA by increasing exposure to ionising radiation and iodinated contrast agent and it is also heavily affected by metal or embolic material artefacts (Kang et al, 2014). A feasibility study was conducted to integrate 4D imaging, such as time resolved contrast-enhanced MR angiography (CE-MRA), into the GKR planning process but the quality of CE-MRA was thought to need further improvement to enable optimal planning of GKR without DSA (Taschner et al, 2007). None of the angiography techniques mentioned above has been shown to provide accurate delineation of AVM radiosurgical targets when used individually on their own. Thus, the potential improvement of GKR planning procedure by replacing DSA with less-invasive imaging is still to be accomplished.

The combination of multiple MRA sequences is an innovative strategy which has already shown promising results in AVM radiosurgery planning. Nagaraja et al found that in a group of 60 AVM patients, the maximum linear dimension and nidus volume delineated using a combination of static (post-contrast TOF) and dynamic (CE-MRA) magnetic resonance angiography techniques, correlated well with radiosurgical targets defined using the conventional DSA method (Nagaraja

et al, 2005). CE-MRA in this study, however, was used through visual inspection only and measurements of nidus volume were based solely on TOF angiography, due to the technical difficulties of integrating 4D data into radiosurgery planning algorithms. An MR angiography fusion technique with acceptable spatial accuracy has also been described to generate hybrid images of high-resolution contrast enhanced MRA and TOF (McGee et al, 2006). However, the contrast enhanced MRA sequence used in that study was not time-resolved and therefore DSA was still required for AVM characterisation and targeting.

More recently, we described triple-MRA which is the combined use of three MRA sequences including HD-TOF, time resolved CE-MRA and 4D ASL-MRA (Rojas Villabona et al, 2017). Triple-MRA was shown to consistently demonstrate/rule out residual AVMs in patients treated with GKR for brain AVMs compared to DSA and it can also be reliably used for characterisation of residual AVMs. The major accomplishment of using multiple MRA investigations is the combination of high temporal and spatial resolution, which are both necessary to appreciate the unpredictable blood flow dynamics of AVMs (Nagaraja et al, 2005; Taschner et al, 2007). The distinctive element of triple-MRA, in terms of sequences, is ASL-MRA which enables acquisition of dynamic cerebral angiography with temporal resolution comparable to that of DSA (100 - 200 ms) without the administration of contrast agents (Lindner et al, 2015; Suzuki et al, 2017; Wu et al, 2013). ASL-MRA has already been shown to be useful for non-invasive assessment of cerebral AVMs and it can provide dynamic information on flow and angio-architecture of AVMs which had not been previously possible using MRA (Fujima et al, 2016; Iryo et al, 2016).

This study aims to evaluate whether the combination of three MRA techniques, referred to as triple-MRA, could be used as an alternative to DSA for visualisation and delineation of brain AVMs for GKR targeting.

5.3 Methods

5.3.1 Patients

Fifteen consecutive adult patients undergoing DSA for targeting of GKR for brain AVMs at the National Hospital for Neurology and Neurosurgery between June 2015 and October 2016 were prospectively recruited. All participants gave written consent for a triple-MRA to be performed before GKR and the study was approved by the Queen Square research ethics committee (Appendix 3). The research pathway and image analysis framework used for radiosurgery target delineation with DSA and triple-MRA, are shown in the flow diagram in Figure 5.1.

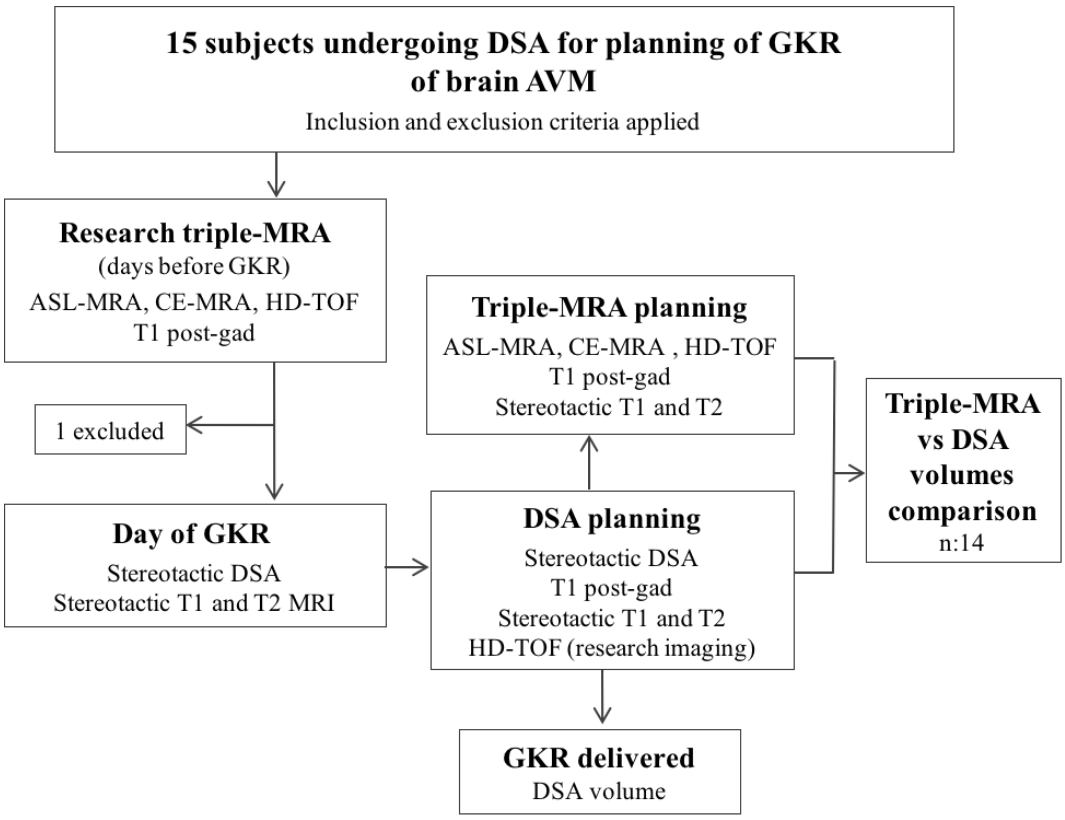

Figure 5.1. Research pathway and image analysis framework used for target delineation with DSA and triple-MRA. DSA volume is the radiosurgical target drawn for delivery of GKR using 2D projections of DSA together with post-contrast T1, TOF and T2 weighted MRI. Triple-MRA volume includes the areas shown to be part of the AVM nidus on triple-MRA, post-gad T1 and T2 weighted MRI.

Exclusion criteria included inability to tolerate MR imaging without sedation/anaesthesia, impaired renal function (eGFR < 30ml/min), inability to consent, pregnancy, allergy to gadolinium, contraindication to MRI (i.e., pacemakers, metallic implants, etc.) and history of endovascular coiling of cerebral aneurysms.

Table 5.1 shows the demographic details and AVM characteristics of the study subjects. Mean age was 38 years (range: 18 - 62) and 10 patients (66%) were female. Ten patients presented with intracranial bleeds, two with seizures and the AVM was incidentally found in three subjects. The lesions were Spetzler-Martin grade 1 and 2 in 43% of the cases, grade 3 in 42% of the patients and high-grade AVMs (4 and 5) were observed in 15% of them. Three patients had undergone partial glue embolization before GKR, one of them on two occasions, and none of them had undergone previous microsurgical excision.

Table 5.1. Demographic details and AVM characteristics of the study subjects.

Age mean (min - max)			38 y (18 - 62)
Female, n (%)			10 (66%)
AVM location, n		Frontal	3
		Parietal	2
		Occipital	4
		Temporal	3
		Basal ganglia	2
		Post fossa	1
Lateralisation, %		Right	53%
		Left	47%
Presentation, n (%)		Intracranial bleed	10 (66%)
		Seizures	2 (14%)
		Incidental	3 (20%)
SMS n: 14 one case excluded	**Size, %**	< 3 cm	71%
		3 - 6 cm	22%
		> 6 cm	7%
	Eloquence, %	Non-eloquent	35%
		Eloquent	65%
	Drainage, %	Superficial only	43%
		Deep	57%

5.3.2 Triple-MRA imaging protocol

Triple-MRA was acquired using a 32-channel Achieva 3.0 T MRI system (Philips Healthcare Systems, Best, The Netherlands). The protocol included ASL-MRA, CE-MRA and post-contrast HD-TOF and the scanning parameters are provided in Table 5.2. Triple-MRA was non-stereotactic (without a stereotactic frame) and performed before GKR. The median time between triple-MRA and GKR was 10 days (range, 2 – 87 days); it was more than 30 days in four patients.

ASL-MRA uses the same principle as ASL perfusion imaging: arterial blood water is magnetically labelled with a radiofrequency pulse proximal to the brain and it is used as an intrinsic contrast agent and flow tracer (Petersen et al, 2006). This is achieved by inverting the longitudinal magnetization of arterial water spins which changes the contrast properties of inflowing blood with respect to the surrounding tissue (Golay et al, 2005). The subtraction of an image with inverted blood spins (label) and without inversion (control) results in images of the inflowing blood only (Lindner et al, 2015). Under normal conditions, most labelled water is extracted at the capillary level into the tissue, giving rise to the parenchymal perfusion signal intensity for which ASL is better known (Petersen et al, 2006; Xu et al, 2010). The same principle, with an earlier acquisition -before the labelled water leaves the vasculature- and with a much higher resolution can be applied to obtain angiographic images with near zero background and inflow dynamics similar to DSA (Nakamura et al, 2012). ASL angiography with Echo Planar Imaging (EPI) enables fast dynamic acquisition of multiple phases per second with reasonable scanning times (Suzuki et al, 2017). This offers a high degree of flexibility in terms of temporal resolution which was exploited in our study for individualised timing of ASL-MRA (Figure 5.2). An ASL survey with EPI acceleration was used to characterise the filling velocity of the AVM in each individual case. The three time points best suited to show the arterial phase of the AVM nidus were then acquired with ASL-MRA which had less dynamic time points, better spatial resolution and pulsation artefact robustness (non-EPI). By reducing the number of dynamic points the labelled blood is less saturated during acquisition which prolongs the labelling effect and improves the SNR (Jensen-

Kondering et al, 2015). The ASL survey encompassed 8 dynamic phases with a temporal resolution of 200 ms. A 300 mm Signal Targeting with Alternating Radiofrequency (STAR) labelling slab was positioned below the imaging plane. A small (10 mm) axial slab including part of the AVM nidus was scanned in 54 seconds (Table 5.2). The size and position of the labelling slab used for the ASL survey remained unchanged for ASL-MRA acquisition to ensure the same transit time between the labelling slab and the AVM nidus. There was a significant degree of variability between patients in terms of optimal label delay which ranged from 200 - 800 ms (mean: 470 ms; SD: 212 ms) and phase interval, or time between dynamic frames, which ranged from 200 to 300 ms (mean: 236 ms). For this reason, ASL-MRA scanning time varied among patients from 5:58 to 12:24 min (mean: 8:46 min).

CE-MRA included 24 dynamic time points and was acquired using a 3D, T1 weighted, fast-field echo (FFE) sequence. A reference scan was acquired before contrast injection for subtraction of the stationary tissue and dynamic sampling was started at the same time as the injection. A manual IV bolus injection of 0.2mL/kg of Gadobenic acid 0.5M (MultiHance, Milan, Italy) was performed over an estimated time of 4 seconds followed by a saline flush of 20 ml. The fast dynamic acquisition used contrast-enhanced robust-timing angiography (CENTRA) and the keyhole method with 20% of the *k*-space collected per keyhole frame (Willinek et al, 2008). Sensitivity encoding (SENSE) was also used with a reduction factor of 4 in the phase-encoding direction and 2 in the slice-encoding direction resulting in a temporal resolution of 608 ms/phase. HD-TOF acquisition was started approximately 10 minutes after injection of gadolinium. It was based on a 3D-FFE acquisition with flow compensation and tilt-optimized non-saturated excitation (TONE) across the slab (Wrede et al, 2014). Four slabs covering 50mm in the cranio-caudal direction were obtained with parallel imaging, SENSE factor of 2. A 3D post-contrast T1 weighted MRI scan which is part of standard GKR planning was acquired alongside triple-MRA -to avoid double injection of contrast agent- using the following parameters: T1 FFE; acquisition matrix: 256 x 256; slice thickness: 1.5 mm, no overlap; voxel size: 0.82 x 0.82 x 1.5 mm.

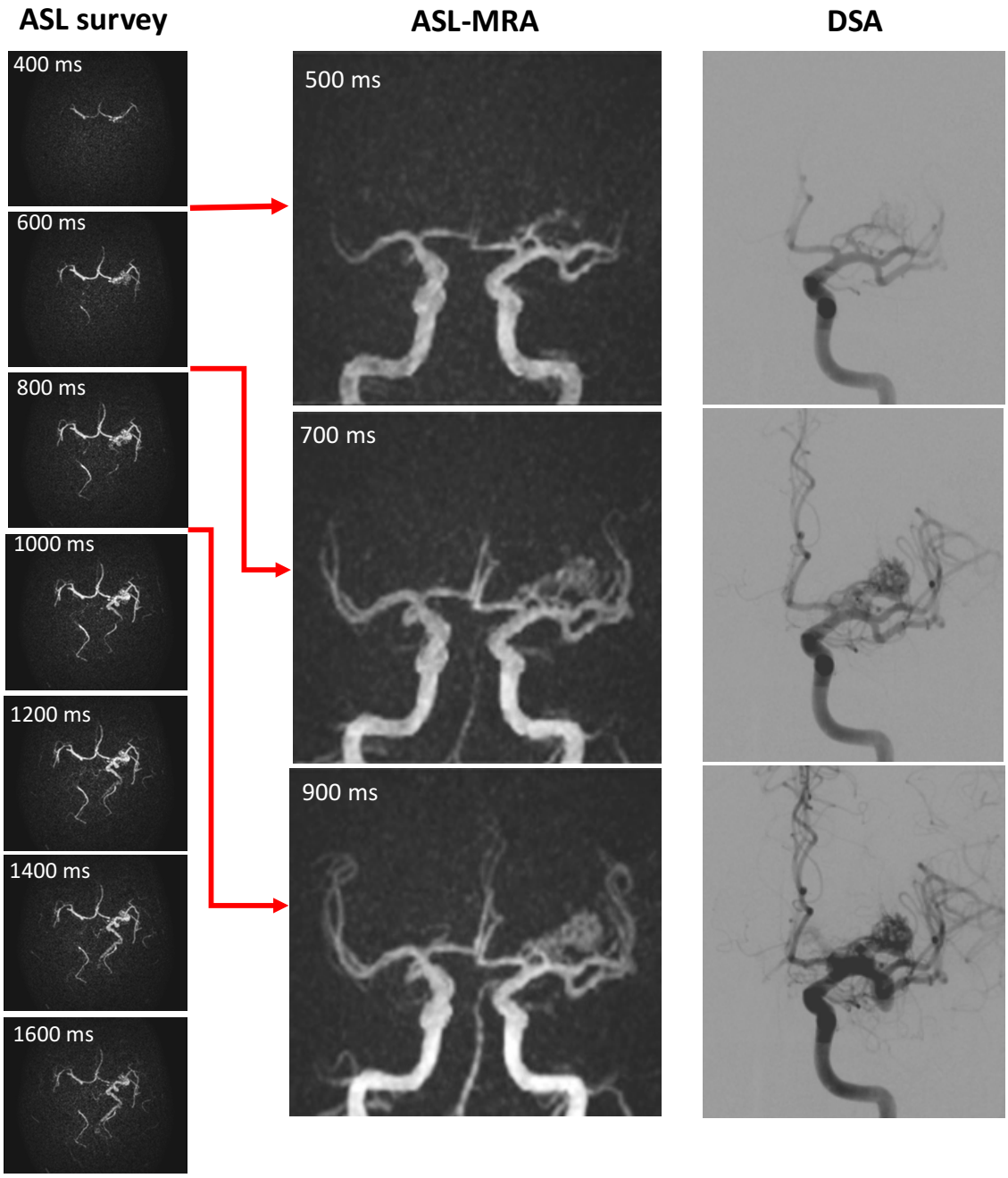

Figure 5.2. Representative example of the ASL survey developed to individualise timing of ASL-MRA. The ASL survey (left panel; temporal resolution: 200 ms; axial slab: 10 mm, acquisition time: 54 sec) enabled rapid characterisation of AVM filling velocity and the selection of three time points (500, 700 and 900 ms) in which the filling of the nidus is adequately visualised. The ASL-MRA acquisition is then limited to the selected time points (middle panel, AP MIP). The right panel shows the AP projection of DSA on the same patient for comparison.

Table 5.2. Triple-MRA scanning parameters.

Parameter	ASL survey	ASL-MRA	CE-MRA	HD-TOF
MRA type	Dynamic survey	Dynamic	Dynamic	Single time point
Scan duration (mins:sec)	0:54	5:58 - 12:24	3:19	08:54
Contrast				
Scan mode	3D	3D	3D	3D
Acquisition	T1 TFEPI	T1 TFE	T1 FFE	T1 FFE
T_R (ms)	12	4.5	3	25
T_E (ms)	5	2.5	1.1	3.45
Flip Angle (°)	10	10	25	25
Resolution				
FOV (RL x AP x CC, mm)	210 x 210 x 10	210 x 210 x 90	150 x 210 x 210	250 x 250 x 50
Acquisition	transversal	transversal	Sagittal	transversal
Slabs	1	1	1	4
Acquisition matrix	172 x 167 x 8	172 x 172 x 70	50 x 248 x 248	832 x 568 x 50
Acquired voxel size (mm)	1.22 x1.26 x1.3	1.22 x 1.22 x 1.3	3 x 0.85 x 0.85	0.3 x 0.44 x 1
Reconstruction matrix	256 x 256	256 x 256	288 x 288	1936 x 1936
Rec voxel size (mm)	0.82 x 0.82 x 0.65	0.82 x 0.82 x 0.65	1.5 x 0.73 x 0.73	0.13 x 0.13 x 0.5
Number of slices	8	140	100	100
SENSE factor	2.5	2.5	4/2	2
Dynamic acquisition				
Dynamic imaging mode	TFEPI	TFE	CENTRA keyhole	-
Number of phases	8	3	24	-
Phase interval (temporal resolution)	200	200 - 300 ms	608 ms	-
Label delay	200	200 - 800 ms	-	-
Contrast	-	-	Multihance 0.2ml/Kg	Post-contrast

5.3.3 DSA protocol and stereotactic MRI for GKR planning

The stereotactic method used at Queen Square Radiosurgery Centre has been described elsewhere (Rojas-Villabona et al, 2016a). Stereotactic DSA was performed under local anaesthesia using a biplane system (Artis zee Biplane, Siemens, Erlangen, Germany) and iodinated contrast agent (Iohexol 240 mg/ml, Omnipaque, GE Healthcare, Cork, Ireland). A femoral artery approach was used for selective contrast injection of one or several vessels known to supply the AVM. DSA was performed at a rate of 3-7 frames/second in standard orthogonal anteroposterior (AP) and lateral projections; oblique projections were acquired when deemed necessary. For GKR planning a thorough review of the DSA series by the interventional neuro-radiologist performing the procedure results in the selection of one or a few time points in the early arterial phase where the AVM nidus is optimally pictured. The AP and lateral X Ray projections of the selected time points are then imported into Leksell GammaPlan 10.1 (Elekta Instrument AB, Stockholm, Sweden) and defined into the stereotactic coordinates system, together with stereotactic T1 and T2 weighted MRI, for radiosurgery targeting.

Stereotactic 3D T1 and T2 weighted MRI were obtained on the day of GKR using a Magnetom Avanto 1.5 T MRI system (Siemens AG, Erlangen, Germany) with the following parameters. T1 weighted: FLASH; T2 weighted: CISS; acquisition matrix: 448 x 448; slice thickness: 1.5 mm, no overlap; FOV: 210 x 210 mm; voxel size: 0.47 x 0.47 x 1 mm. Stereotactic 3D T1 weighted MRI was obtained post-contrast in four cases in which triple-MRA had been performed more than 30 days before GKR. In the remaining cases, the T1 post-contrast scan acquired on the day of triple-MRA was used for planning of GKR by co-registering it to the non-contrast stereotactic scans obtained on the same day of GKR, using the co-registration tool in Leksell GammaPlan 10.1. TOF angiography is routinely used as a complementary imaging modality to DSA in many GKR centres around the world (Potts et al, 2014; Seymour et al, 2016). For this reason, HD-TOF was also co-registered with the stereotactic scans performed on the day of GKR and it was available to the radiosurgery team for target delineation alongside DSA. In summary, imaging used for delineation of a DSA based volume included:

stereotactic DSA, stereotactic T2 weighted and post-contrast T1 weighted MRI and HD-TOF (Figure 5.3).

The early arterial phase of the AVM nidus was delineated in consensus by the practising consultant neurosurgeon, the interventional neuroradiologist who performed the DSA procedure and a medical physicist using the delineation tool in Leksell GammaPlan 10.1. The resultant volume (DSA volume) was then used to develop a radiosurgery treatment plan which was then delivered with a Leksell Gamma Knife Perfexion (Elekta Instrument AB).

5.3.4 AVM target definition on triple-MRA

ASL-MRA, CE-MRA and HD-TOF data were transferred to the Brainlab Elements platform (Brainlab AG, Munich, Germany) for post-processing and triple-MRA target delineation. The volumetric datasets of all three ASL-MRA time points were individually co-registered with HD-TOF using Brainlab Merge Element (Brainlab AG). The quality of co-registration was validated using intracranial arteries as landmarks, namely, branches of the middle cerebral artery bilaterally, the pericallosal and marginal arteries superiorly and the basilar artery bifurcation. The overlap of these blood vessels in the individual pairs of datasets undergoing co-registration was visually assessed in all three orthogonal planes and co-registration ROIs were defined to improve the quality of co-registration where necessary. This applied to all co-registration steps performed in this study. Dynamic CE-MRA datasets were visually inspected (ARV) to select two time points that best depicted the AVM nidus, in a similar manner as DSA dynamic datasets are routinely reviewed to select a few DSA images that are incorporated into GKR planning. Volumetric datasets of selected CE-MRA time points were co-registered to HD-TOF and 360 degree of rotation Maximum Intensity Projections (MIPs) were generated for all three MRA sequences. In order to simulate the clinical scenario in which angiography is used alongside structural MRI for radiosurgery planning, the T1 post-contrast and T2 weighted MRI data were also imported into the Brainlab platform, co-registered to HD-TOF and used for triple-MRA volume delineation (Figure 5.3).

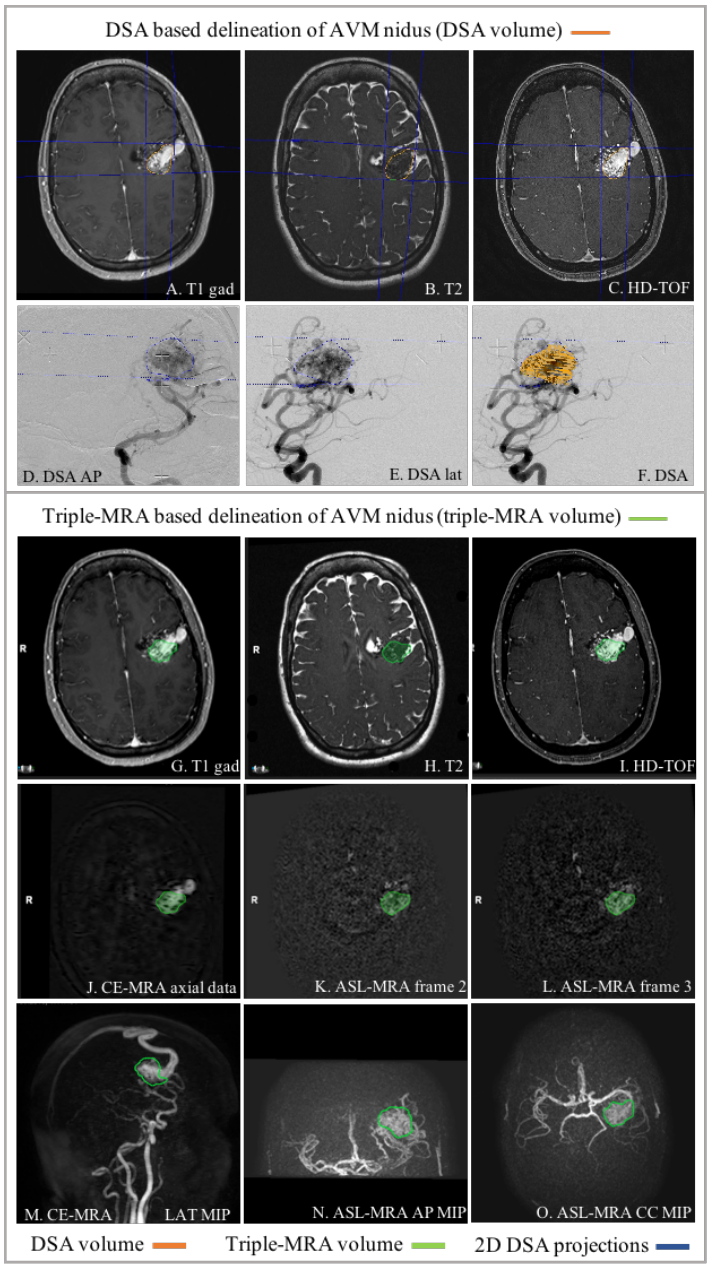

Figure 5.3. Imaging used for AVM delineation with the standard DSA based method and triple-MRA. Stereotactic DSA(D-F) together with standard volumetric MRI (top row) is the current reference standard for target delineation in AVM radiosurgery. The limits (blue lines) of an AVM ROI delineated on 2D DSA images (blue contour) are projected into volumetric MRI defining an area within which the AVM is contained. A 3D volume is then drawn within this area on volumetric scans (DSA volume, orange). Definition of an AVM volume on triple-MRA (bottom three rows) is based on co-registered MRA sequences: ASL MRA (K-L), CE-MRA (J) and HD-TOF (I) together with routine volumetric MRI. A 3D volume is drawn including areas shown to be part of the AVM nidus on all co-registered multimodality images and the resultant triple-MRA volume (green) is displayed on 360 degrees of freedom MIPs of the MRA sequences (bottom row).

Triple-MRA based volumes were delineated using the semi-automatic drawing tool SmartBrush Element (Brainlab AG) by including areas shown to be part of the AVM nidus on ASL-MRA, CE-MRA, HD-TOF, post-contrast T1 and T2 weighted MRI scans, excluding draining veins. This was done by an interventional neuroradiologist and a consultant neurosurgeon (TS and JG), both with more than 15 years of experience, who are radiosurgery practitioners at Queen Square and had not been involved with treatment planning of the patients recruited, except in two cases in which the consultant neurosurgeon (JG) was involved in delineation of both the DSA as well as the triple-MRA volumes.

The quality of triple-MRA was evaluated with regards to artefacts that could potentially affect the quality of AVM delineation. Vessel visualization was assessed for each MRA sequence using a five-point categorical scale (poor, fair, good, very good, excellent). Characterisation of AVMs on triple-MRA included Spetzler-Martin grading and identification of feeding arteries, abnormalities of the draining veins and associated aneurysms. The observer's level of confidence on their estimation of AVM nidus on triple-MRA was assessed using a three-point categorical scale (not entirely confident, confident, highly confident) by asking them how confident they would feel about delivering GKR based on triple-MRA volume.

5.3.5 Data analysis

Difference in size, degree of inclusion and concordance between DSA and triple-MRA volumes were calculated (Duan et al, 2014). Triple-MRA volumes were imported into Leksell GammaPlan 10.1 on format DICOM-RT structure using the HD-TOF dataset which was co-registered into the stereotactic system. This enabled both triple-MRA and DSA volumes to be defined in the same stereotactic space, and on common MRI datasets, for comparison. The percentage difference between DSA and triple-MRA volumes is reported. One-sample t-test was used to determine if the percentage difference between DSA and triple-MRA volumes was significantly different from 0. The percentage difference between DSA and triple-MRA volumes was further analysed using a Bland-Altman plot.

Comparison of volumes in terms of inclusion and concordance was performed off-line using MATLAB 9.2 (The MathWorks Inc, Natick, Massachusetts, USA). The DICOM-RT structures of both DSA and triple-MRA volumes were exported from GammaPlan and used to create separate masks on HD-TOF for computation. Degree of inclusion (DI) is the percentage of DSA volume (DSAv) included in triple-MRA volume (tMRAv) calculated using the equation below, where $\cap$ is the intersection between two volumes:

$$\mathrm{DI\ (DSAv\ in\ tMRAv)} = \left(\frac{\mathrm{DSAv}\ \cap\ \mathrm{tMRAv}}{\mathrm{DSAv}}\right) \times 100$$

The percentage of triple-MRA volume not included in DSA volume, termed degree of non-inclusion (DnI), is:

$$\mathrm{DnI\ (tMRAv\ not\ in\ DSAv)} = \left(1 - \frac{\mathrm{DSAv}\ \cap\ \mathrm{tMRAv}}{\mathrm{tMRAv}}\right) \times 100$$

The Concordance Index (CcI) of DSA and triple-MRA volumes is the ratio of the intersection to the union ($\cup$) of the two volumes, as described by Jaccard. The maximum value of CcI is 1 if the two volumes are identical, and the minimum value is 0 if the volumes are completely non-overlapping (Jaccard, 1912).

$$\mathrm{CcI} = \frac{\mathrm{DSAv}\ \cap\ \mathrm{tMRAv}}{\mathrm{DSAv}\ \cup\ \mathrm{tMRAv}}$$

Correlation between CcI and age, AVM volume, Spetzler-Martin grade and ASL-MRA phase interval were assessed with Spearman's rank correlation coefficient (rho). The effect of categorical variables (gender, previous bleeds, previous treatments, laterality, location, eloquence of the surrounding brain, drainage pattern and AVM density assessed on DSA as diffuse vs compact) on CcI was assessed using the non-parametric Mann-Whitney U test. Statistical analyses were performed using the Statistical Package for the Social Sciences (SPSS Statistics, Version 23. IBM Corp) and statistical significance was defined as a p value of < 0.05.

5.4 Results

All fifteen participants successfully underwent triple-MRA before the day of GKR. They also had stereotactic DSA for planning of radiosurgery, except one patient who declined GKR after triple-MRA had been acquired. This case was excluded and final statistical analysis includes 14 subjects. Total triple-MRA scanning time ranged from 19:05 to 25:33 min (mean: 21:53 min). It varied among patients due to individualised timing of ASL-MRA.

AVM target volumes obtained using the standard DSA method and triple-MRA are presented in Table 5.3. The mean DSA volume, drawn by the neurosurgical team for delivery of GKR using 2D projections of DSA into structural MRI, was 3.89 ml (95%CI: 1.95 - 5.82 ml; SD: 3.35 ml; median: 3.35 ml; range: 0.1 - 10.77 ml). AVM volumes delineated on triple-MRA were significantly smaller (p = 0.003). The mean triple-MRA volume was 3.49 ml (95%CI: 1.77 – 5.2 ml; SD: 2.97 ml; median: 2.88 ml; range: 0.09 - 9.89 ml) and was smaller than the DSA volume in all but one case (Figure 5.4). The relative difference between DSA and triple-MRA volumes was on average 9.8% (95%CI: 5.6 - 13.9%; SD:7.14%; median: 10.5%; range: -7.3 - 18.7%).

DI of DSA volume in triple-MRA volume was on average 73.5% (95%CI: 71.2 - 76%; SD: 4.1%; median: 73%; range: 65 - 80%). It was above 70% in all subjects except for case 9, in which a small difference between the volumes represented a high percentage discrepancy due to the very small size of the target (0.103 ml, Figure 5.5). The mean percentage of triple-MRA volume not included on DSA (DnI) was 18% (95%CI: 14.7 - 21.3%; SD: 5.7%; median: 18.4%; range: 7 - 30%). It was 20% or less in all subjects except for two cases (Table 5.3). One of these was case 9 (30%) for the same reason as stated above (Figure 5.5). The other case (26%) was the only subject in which triple-MRA volume (2.27 ml) was larger than DSA volume (2.10 ml). This was due to the inclusion on triple-MRA volume of an area in the medial aspect of the AVM nidus which appeared abnormal on triple-MRA, T1 post-gad and T2 but only slight and diffuse vasculature was seen on DSA (case 10, Figure 5.6).

Table 5.3. AVM target volumes obtained using the standard DSA method and triple-MRA. DSA volume is the radiosurgical target drawn by the clinical team for delivery of GKR using 2D projections of DSA into volumetric structural MRI. Triple-MRA volume includes all areas shown to be part of the AVM nidus on ASL-MRA, CE-MRA, HD-TOF and volumetric structural MRI. DI is the percentage of DSA volume included in triple-MRA volume. DnI is the percentage of triple-MRA volume not included in DSA volume. CcI is the ratio of the overlap to the union of the two volumes.

Case	DSA volume (ml)	Triple-MRA volume (ml)	Percentage difference (%)	DI (%)	DnI (%)	CcI
1	3.03	2.48	(-)18.3	76	7	0.72
2	8.73	7.21	(-)17.5	71	14	0.63
3	4.96	4.96	(-)0.05	79	20	0.65
4	0.56	0.51	(-)10.7	71	20	0.60
5	3.69	3.29	(-)10.4	71	20	0.60
6	5.87	5.14	(-)13.2	72	17	0.63
7	10.77	9.89	(-)8.2	78	15	0.69
8	1.32	1.07	(-)18.7	71	12	0.65
9	0.10	0.09	(-)8.1	65	30	0.51
10	2.10	2.27	7.3	80	26	0.62
11	0.23	0.21	(-)9.8	74	18	0.64
12	1.29	1.13	(-)12.7	71	19	0.61
13	4.20	4.00	(-)4.4	75	20	0.63
14	7.63	6.68	(-)12.4	76	13	0.69
Mean 95%CI	3.89 ml 1.95 – 5.82	3.49 ml 1.77 – 5.21	(-)9.8% (-)5.6 – (-)13.9	73.5% 71.2 – 76	18% 14 – 21	0.63 0.6 – 0.66
Median range	3.35 ml 0.1 – 10.77	2.88 ml 0.09 – 9.89	(-)10.5% (-)7.3 – 18.7	73% 65 – 80	18.4% 7 – 30	0.63 0.5 – 0.72

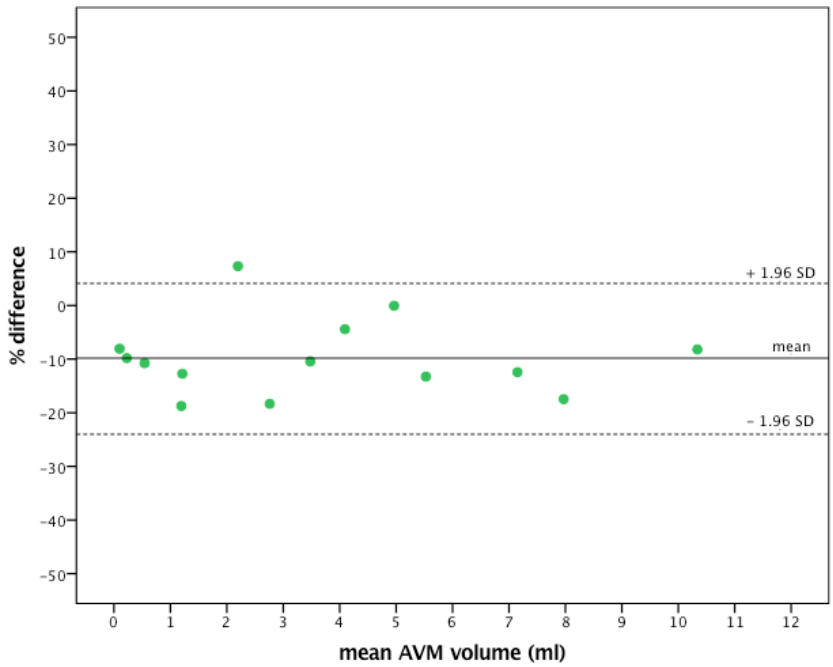

Figure 5.4. Bland-Altman plot of the difference between DSA and triple-MRA volumes.

The mean CcI was 0.63 (95%CI: 60.4 - 66.2; SD: 0.05; median: 0.63; range: 0.51-0.72). CcI was above 0.6 in all other cases but one in which the discrepancies described above also had a considerable effect on CcI (0.52, case 9). There was a weak correlation between CcI and AVM volume (rho = 0.54; p = 0.047). This was driven mainly by case 9 which was the smallest AVM and also had the lowest CcI in the group. Hence, the correlation was not seen if case 9 was excluded (rho=0.42; p = 0.15). There was no correlation between CcI and age (p = 0.83), Spetzler-Martin grade (p = 0.89) or ASL-MRA phase interval, the latter of which can be considered a surrogate for AVM filling velocity (p = 0.61). There was no difference on CcI between groups of gender (p = 0.45), previous bleeds (p = 0.45) or treatments (p = 0.09), laterality (p = 0.7), AVM location (p = 0.18), surrounding brain eloquence (p = 0.36), venous drainage pattern (p = 0.75) and AVM density assessed on DSA as diffuse vs compact (p = 0.5).

The AVM nidus was clearly identified on all three MRA techniques in all but two cases. In one case, the lesion was not seen on ASL-MRA due to the very superficial location in the posterior fossa, with the ASL labelled blood losing its tagging before reaching the AVM (case 12). In the other case, shown in Figure 5.3, it was not possible to visualize the AVM in CE-MRA because the acquisition did not include the arrival of gadolinium bolus due to accidental mistiming of the injection with respect to the dynamic acquisition. However, both lesions were well depicted by the other two MRA sequences, their results in terms of CcI were no different to the rest of the cases (p = 0.1) and this was thought to be of no consequence for drawing of triple-MRA volumes. Triple-MRA enabled Spetzler-Martin grading in all subjects. The main arterial feeder was identified with triple-MRA in all cases but one (case 9) due to the small size of the lesion and the overlapping of multiple small vessels on MIP of CE-MRA and ASL-MRA (volume: 0.103 ml; maximum diameter: 4 mm; Figure 5.5). Abnormalities of the draining veins including varicose dilatation or stenosis were identified in 6 subjects and intra-nidal aneurysms were seen in 3 cases. Both members of the triple-MRA planning team indicated they would feel highly confident delivering GKR based on triple-MRA volumes in 43% of the cases. The interventional neuroradiologist felt confident in the remaining 57% of the cases while the consultant neurosurgeon was confident in 43% and not entirely confident in 14% of them (two cases). One of these was the case in which ASL-MRA did not show the AVM nidus (case 12). The other was a large AVM (case 14) in which the nidus was not clearly visualized on ASL-MRA due to a number of greatly dilated veins being embedded in the nidus. Differences between DSA and triple-MRA volumes in these two cases were not significantly higher than the rest of the patients, p = 0.14 (Table 5.3).

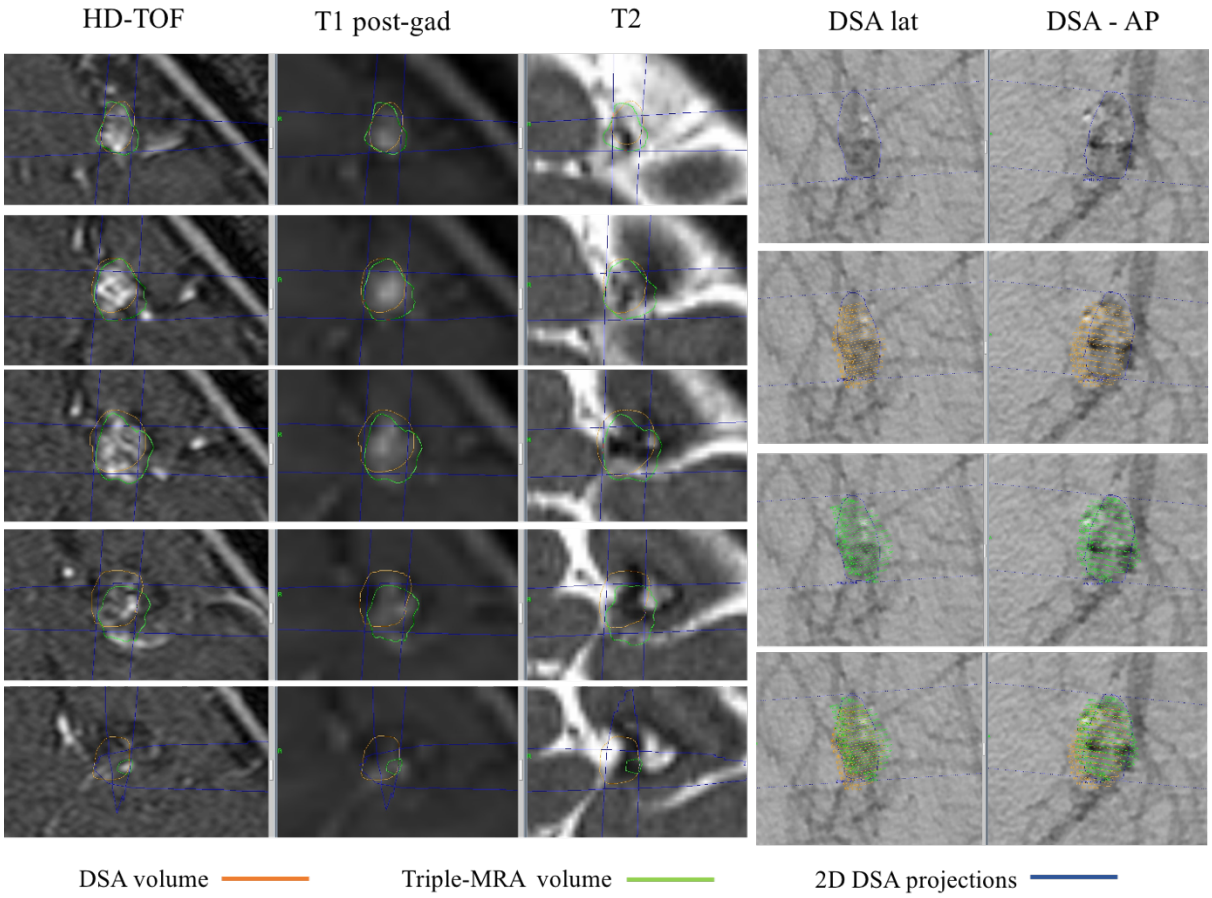

Figure 5.5. DSA and triple-MRA volumes in the case with the lowest DI and CcI. The DSA volume (orange) and triple-MRA volume (green) at five representative axial levels of the AVM in case 9 are shown on HD-TOF, T1 post-gad and T2 weighted MRI (first three columns from the left, respectively). The two volumes are also displayed on the lateral and AP projections of DSA (last two columns on the right). Triple-MRA volume seems to be more conformal than DSA volume with the AVM ROI delineated on 2D DSA images (blue contour). During a standard GKR planning session the limits of the AVM ROI delineated on 2D DSA are projected into volumetric MRI scans to define an area within which the AVM is contained.

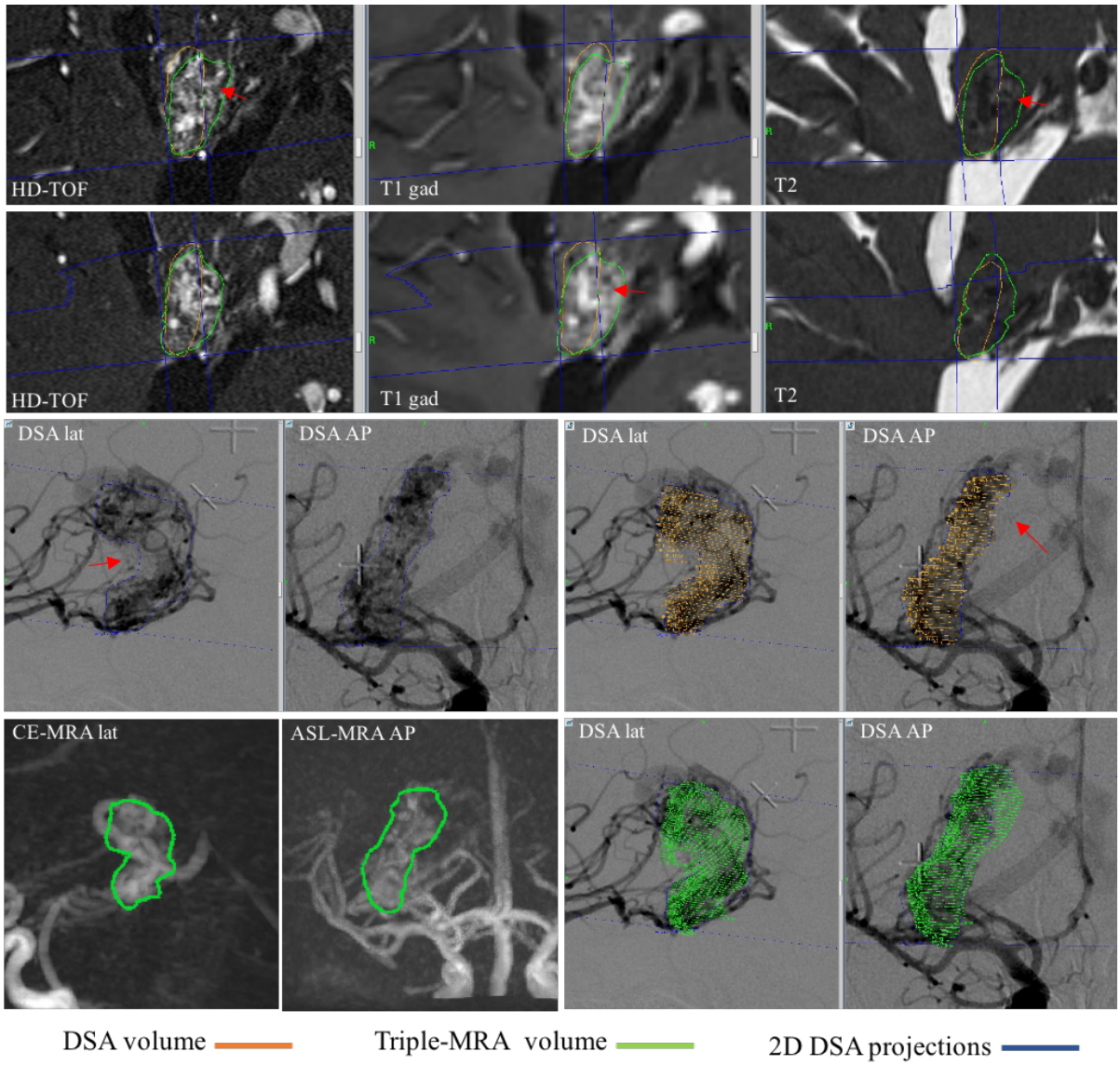

Figure 5.6. Case 10, in which triple-MRA volume was larger than DSA volume. The top two rows show representative axial levels of the area in the medial aspect of the AVM nidus which appeared abnormal (red arrows) on HD-TOF, T1 post-gad and T2 and therefore was included on triple-MRA volume (green). Only very slight and diffuse vasculature is noted in this area on DSA (third row) and this resulted on DSA volume (orange) being smaller than triple-MRA volume in this case. In the bottom row, triple-MRA volume is projected on lateral and AP MIPs of CE-MRA, ASL-MRA and DSA for comparative purposes.

5.5 Discussion

This study aimed to prospectively evaluate whether the combination of three MRA sequences, namely ASL-MRA, CE-MRA and HD-TOF, could be used as an alternative to DSA for visualisation and delineation of brain AVMs for GKR targeting. In a group of 14 patients undergoing GKR, the AVM nidus was delineated on triple-MRA and compared to the AVM target defined for GKR using the current planning paradigm, which is stereotactic intra-arterial DSA and volumetric MRI scans on the day of treatment (DSA volume). The use of DSA for AVM radiosurgery planning could be abandoned without reservations, if no difference whatsoever would have been detected between triple-MRA and DSA volumes. That was, however, not the outcome of the study. Triple-MRA volumes were on average 10% smaller than DSA volumes. The size difference between DSA and triple-MRA volumes was statistically significant and only in one case was triple-MRA volume larger than DSA volume (Figure 5.6). On average, 73.5% of DSA volume was included in triple-MRA volume and the mean CcI, which is the ratio of the intersection and the union of the two volumes, was 0.63.

The differences observed between triple-MRA and DSA volumes in terms of size and concordance could be the result of three elements of the evaluation process. First, the use of a different set of images for target delineation, i.e. true volumetric triple-MRA instead of projection based DSA, which is the subject of our study. Second, the degree of variability inherent to AVM radiosurgery planning, in particular inter-observer variability. This is most likely to affect estimates of concordance between the volume contours rather than systematically providing smaller volumes with one of the methods. However, this defines the best results that can be achieved within our study design, in terms of concordance between the two volumes, considering that DSA and triple-MRA volumes were delineated by two different radiosurgical teams. Third, the uncertainty or error of the co-registration procedures used to relay information from non-stereotactic images (triple-MRA) into the stereotactic GKR system.

The use of triple-MRA instead of DSA is likely to be the main contributor to the

finding of smaller target volumes when delineation is performed on triple-MRA. DSA provides only 2-dimensional projections of the AVM nidus and spatial information is lost because of dimensional reduction (Colombo et al, 2003). Volumes rendered from data with reduced dimensions are likely to be overestimated due to superimposition of feeding arteries and draining veins and difficulties in determining complex 3D variations on nidus geometry (Huang et al, 2017). Triple-MRA sequences, on the other hand, are all volumetric acquisitions which are thought to enable more refined delineation of complex 3D objects such as AVMs (Bednarz et al, 2000). Additionally, the dynamic information provided by triple-MRA is likely to improve target delineation by better differentiation of AVM components, particularly the distinction between nidus and draining veins (Taschner et al, 2007). This is not possible using TOF and standard structural MRI only and previous studies have reported that the lack of dynamic information in these techniques results in overestimation of the nidus (Buis et al, 2007; Huang et al, 2017). The combination of dynamic MR angiography with HD-TOF and structural MRI can overcome this issue by showing haemodynamic abnormalities specific to the nidus. ASL-MRA, for instance, can be used to reliably identify AV shunting which is an unequivocal and defining element of the AVM nidus. Because AVMs lack a capillary bed for water extraction to take place, and the labelled spins are shunted directly into the venous circulation with minimal transit time, signal intensity which is specific to an AV shunt and early draining veins can be obtained using ASL (Jang et al, 2014). This can effectively help exclude areas that do not have the characteristic flow abnormalities of the AVM nidus and therefore should not be included in the target volume, such as draining veins, hematoma, stagnated blood or neo-vascularisation tissue (Bednarz et al, 2000). ASL-MRA is also a very flexible technique that enables personalised image acquisition based on the individual characteristics of each patient. This is a well-recognised concept in DSA where different frame rates (3 to 7 time points/sec) are used depending on the filling velocity of the abnormality. To our knowledge, this is the first time individualised timing of MRA acquisition was used for imaging of brain AVMs (Figure 5.2). This has enabled us to account for differences in heart rate, blood flow and AVM filling velocity between patients which contributed to

better discrimination of the AVM nidus and the smaller target volumes found with triple-MRA.

In this study, triple-MRA volume was defined as areas shown to be part of the AVM nidus on ASL-MRA, CE-MRA, HD-TOF, post-contrast T1 and T2 weighted MRI scans, excluding draining veins. This means that only areas that were convincingly part of the nidus in all sequences were included. Under these conditions triple-MRA does not only pool the strengths of each MRA sequence but it also works as a multi-level evaluation system that results in the exclusion of areas which do not appear to be consistently part of the nidus. Therefore, decision making is not based on a single imaging modality but on several complementing sequences, which are individually better suited for assessment of specific aspects of an AVM. CE-MRA, for example, is the best sequence for the evaluation of draining veins. Figure 5.7 shows how CE-MRA can show the early filling of draining veins with a degree of detail that is not far from DSA. This is of great importance for planning of GKR of AVMs because radiosurgical targets can be overestimated by failing to identify and exclude the draining veins (Buis et al, 2007). As part of triple-MRA, this specific strength of CE-MRA complements the other MRA sequences, i.e., ASL-MRA and TOF. The former has adequate temporal resolution to enable depiction of the feeding arteries (Figure 5.8) and the latter has a higher spatial resolution but lacks the possibility to discriminate between arterial and venous vessels. Therefore, the more refined delineation of AVMs on triple-MRA results in smaller volumes compared to the traditional planning method based on DSA.

There is extensive evidence demonstrating that larger AVM volumes result in higher rates of both symptomatic and radiological ARE (Cohen-Inbar et al, 2015; Kano et al, 2017; Yen et al, 2013). The volume of tissue receiving 12 Gy or more is the factor that best correlates with the development of ARE (Flickinger et al, 2000). Therefore, tighter and more precise delineation of AVM radiosurgical targets is a desirable improvement for GKR (Guo et al, 1993; Moosa et al, 2014). In terms of obliteration rates, it is not possible to tell from our study if the 10% reduction in target size accomplished by using triple-MRA for delineation would

affect clinical outcomes. This is because triple-MRA volume in our study was obtained for comparison purposes only and GKR was delivered based on the standard planning method, i.e. DSA volume. The relatively similar response rate reported by GKR centres with different target delineation methods and levels of expertise suggests that small differences in target size are unlikely to result in reduced response rate (Kano et al, 2012b; Koltz et al, 2013; Starke et al, 2017). For instance, before CT and MRI were introduced, treatment planning for AVMs was based on DSA only and 3D delineation of radiosurgical targets was not used at all (Kemeny et al, 1989; Lunsford et al, 1991). However, their reported two-years obliteration rates of 70 - 80% were not different from modern GKR outcomes. Recent reports of patients treated with GKR using MRI only without DSA have showed no difference in obliteration rate (Amponsah et al, 2012) and contemporary groups that still do not delineate a radiosurgical target on their planning imaging also achieve similar results in terms of obliteration (Levrier et al, 2001). Differences in ARE have been noted between these groups, but response rates appear to be comparable between them. The improvement of GKR planning methods that took place over the last few decades with the introduction of CT and/or MRI for planning -alongside DSA- and the technical development of planning software, did not increase obliteration rates either. This strongly suggests that the 10% reduction in volume target that results from using triple-MRA instead of DSA is unlikely to compromise response rate but may result in less ARE.

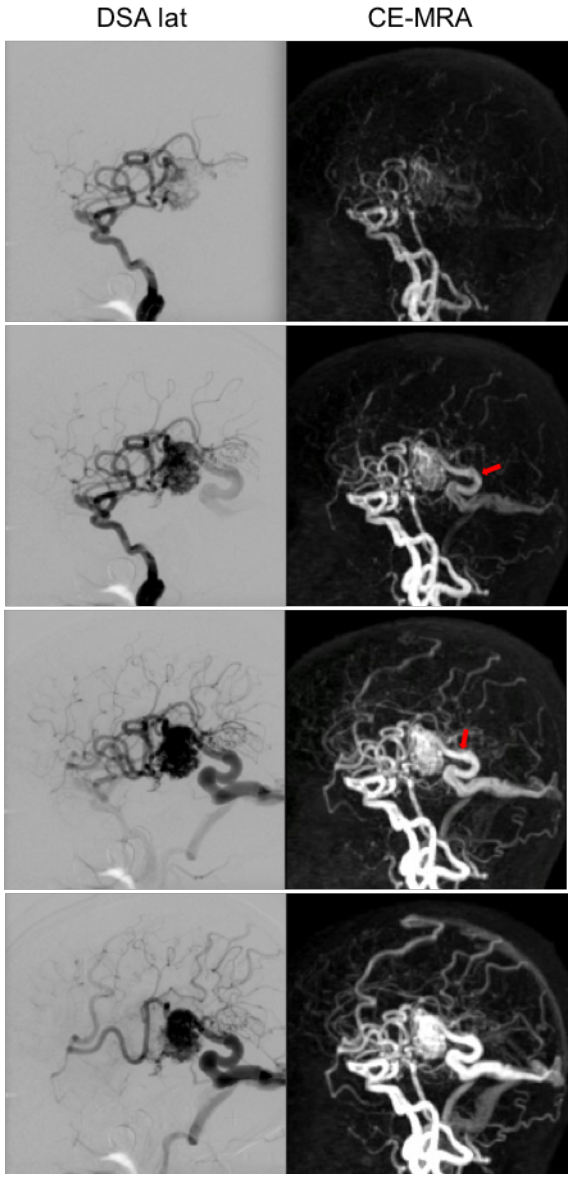

Figure 5.7. CE-MRA and DSA in a study subject with brain AVM. CE-MRA (right) has a temporal resolution of 600 ms and it can show the early filling of draining veins (red arrows) with a degree of detail that is not far from DSA (left).

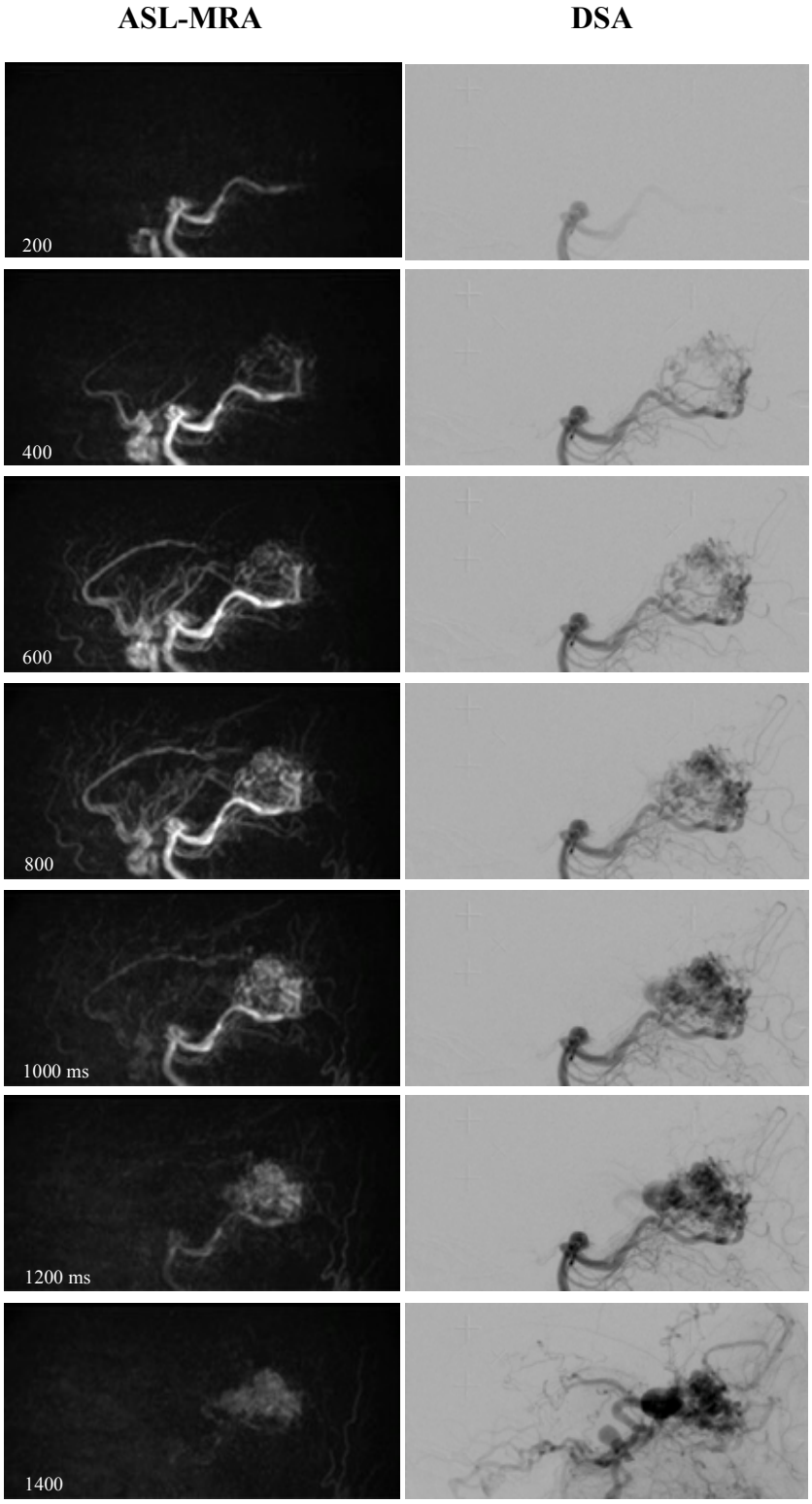

Figure 5.8. ASL-MRA and DSA in a patient with a brain AVM. The ASL-MRA (left) shows the arterial inflow phase with depiction of the AVM nidus and draining veins compared to DSA (right) with a temporal resolution of 200 ms in a study subject.

The differences between DSA and triple-MRA volumes in our study were not limited to size, however. There was also a degree of discrepancy between the contours which was quantified using DI (73.5%; range: 65 - 80%), DnI (18%; range: 7 - 30%) and CcI (0.63; range: 0.51 - 0.72). The fact that triple-MRA volumes are smaller than DSA volumes directly affects these parameters but this is more likely to be the result of the inter-observer variability inherent to AVM radiosurgery planning. In our study triple-MRA and DSA volumes were delineated by two different teams to avoid recall bias and it is not possible to quantify the degree of uncertainty that this could have added to the results. Inter-observer variability, which is a well-recognised issue in AVM radiosurgery and has been quantified elsewhere (Al-Shahi et al, 2002b; Buis et al, 2005; Sandstrom et al, 2014), is important for our study because it defines the best results that can be possibly achieved within our study design. Buis et al evaluated the extent of inter-observer variation in contouring AVMs on DSA in 31 patients who had undergone stereotactic radiosurgery. Six clinicians including two neuro-radiologists, two neurosurgeons and two radiation oncologists independently contoured the nidus on DSA. The reported ratio between the volumes of agreement and the corresponding encompassing volumes (CcI) for all possible pairs of observers was 0.45 ± 0.18 and it was below 0.6 in 76% of the cases. It dropped to 0.19 ± 0.14 when calculated for all six volumes together (Buis et al, 2005). In our study, concordance was considerably better and even our worst case, which is the only one with CcI below 0.6, did not show as poor a CcI as their average estimate. The estimates of inter-observer variability reported by the study above are based on AVM target volumes delineated by active radiosurgery practitioners and they reflect a degree of uncertainty which is already present in standard GKR practice. Sandstrom et al also studied the inter-observer variability of AVM delineation for GKR. The case of a 39-year-old male with a lateral frontal AVM was delineated by 14 observers including neurosurgeons, radiation oncologists and physicists from several GKR centres around the world (Sandstrom et al, 2014). Imaging provided for delineation included DSA, TOF, T1 post-contrast and T2 weighted MRI. The AVM target volumes produced by each observer were compared to a calculated average target (11.86 ml) which was

assumed to resemble the true target. They found that only 1.36 ml were common to all volumes and their union was as much as 27.2 ml. This resulted in a mean CcI of 0.63 (range: 0.24 to 0.81) for all pairs of observations. A mean DI of 78% (range: 11 - 93%) can also be inferred from their results. Although the minimum CcI and DI observed in our study (0.51 and 65%, respectively) are not as low as the ones reported by Sandstrom et al (0.24 and 11%, respectively), their average estimates are very similar to ours. It could, therefore, be argued that the discrepancies between DSA and triple-MRA volumes noted in our study are in effect the expected inter-observer variability rather than unsatisfactory performance of triple-MRA for AVM target delineation. Yet, delineation of AVMs on triple-MRA resulted in consistently smaller AVM volumes (10%) and this is directly reflected by estimates of inclusion and concordance. However, the differences in size between DSA and triple-MRA in our study volumes were nowhere as large as volume differences described by Sandstrom et al (3.48 – 21.05 ml) and even with this extra uncertainty, the contour discrepancy between DSA and triple-MRA volumes in our study was not bigger than the expected degree of inter-observer variability. If anything, concordance between triple-MRA and DSA volumes is better than the inter-observer variability reported by Buis et al using DSA.

Satisfactory delineation of AVM target volumes without the use of DSA has been previously suggested for selected AVM cases (Buis et al, 2007; Taschner et al, 2007; Yu et al, 2004). Yu et al assessed the feasibility of AVM delineation on MRI only for GKR and concluded that it was adequate for cases with non-diffuse and large non-embolised AVMs (Yu et al, 2004). Buis et al concluded that TOF angiography might be used as the sole imaging modality for radiosurgical treatment of AVMs < 3 ml if they were located in non-eloquent areas (Buis et al, 2007). Most GKR practitioners probably also remember cases of small, compact and non-eloquent AVMs which they felt could be accurately delineated and treated using MRI/MRA without a DSA. In our study, we did not identify any convincing variable affecting the quality of target delineation on triple-MRA. The case with the poorest concordance between triple-MRA and DSA volumes in our series was also the smallest and this resulted in a weak correlation between AVM

volume and CcI. We do not believe that triple-MRA volume in this case was inferior in quality compared to DSA volume and if anything, triple-MRA volume seemed to be more conformal with the AVM ROI delineated on 2D DSA images (Figure 5.5). The correlation between AVM volume and CcI in fact disappeared if that case was excluded from the analysis. A review of the case with the second most significant discrepancy between DSA and triple-MRA volumes also failed to reveal a specific factor to explain the differences (case 10). In this case triple-MRA volume was 0.17 ml larger than DSA volume (2.27 vs 2.10 ml) due to the inclusion of an area in the medial aspect of the AVM nidus which appeared abnormal on triple-MRA, T1 post-gad and T2 but only slight and diffuse abnormal vasculature is noted on DSA (Figure5.6). In this case, 80% of DSA volume was included on triple-MRA and CcI was still above 62%. Exactly what constitutes the AVM nidus in this case is open to interpretation but it is not unreasonable to say that these two volumes will most likely result in similar clinical outcomes.

Some of the studies mentioned above have also looked at the effect that AVM delineation without DSA has on treatment dosimetry (Bednarz et al, 2000; Buis et al, 2007). The original treatment plans developed using DSA were used as a reference for comparison and for this reason the results of these analyses mostly reflected the volumetric differences of the targets in question. The use of triple-MRA instead of DSA will still follow the current planning philosophy of delineating the margin of the vascular lesion and then working on conformal coverage. As a result, dosimetric variations should be proportional to volumetric differences. We are aware, however, that adequate treatment conformity (i.e., coverage, selectivity and conformity indices) can be more challenging to achieve if the target outline is less smooth, which can be the case of AVM volumes delineated using triple-MRA.

The use of triple-MRA as an alternative to DSA for AVM radiosurgery planning relies on the development of tools and software capable of integrating multimodality 4D data into the planning procedure. This is still to be accomplished and currently available software could be greatly improved by

implementing co-registration of dynamic sequences and by enabling the visualisation of delineated targets on 4D datasets such as CE-MRA and ASL-MRA. In our study, we relied on a series of co-registrations of the individual time points of the dynamic sequences, which is a potential source of uncertainty affecting the comparability of triple-MRA and DSA volumes. To minimise uncertainty, all co-registrations were validated using intracranial arteries as landmarks by assessing their overlap in all three orthogonal planes. Also, HD-TOF was used as a common dataset in all co-registration pairs, so that it worked as a central link between all sequences avoiding a chain of co-registrations with cumulative and transferable co-registration errors. Two critical co-registration procedures were performed. First, the co-registration between triple-MRA sequences to enable their combined use for delineation of triple-MRA volume. This was accomplished with Brainlab elements merging tool (multimodal rigid image registration with cranial distortion correction). The accuracy of co-registration quoted by the manufacturer is below 1 mm within the intracranial cavity for typical multimodality registrations (Brainlab, 2011; 2017). Second, the co-registration between non-stereotactic HD-TOF and stereotactic MRI which was performed to transfer triple-MRA volume to the stereotactic system. The use of triple-MRA for radiosurgery planning with currently available technology is based on this co-registration step which we performed using GammaPlan. Co-registration of non-stereotactic MRI or CT imaging has long been integrated into GKR planning. Diagnostic MRI taken prior to GKR is frequently used for treatment pre-planning and on the treatment day dose planning is completed by co-registering them with the stereotactic MRI or CT (with the frame). The geometrical accuracy of this procedure has been independently demonstrated in both phantom and clinical studies, using multi-modality co-registration, and the mean error of coordinates between images were consistently < 1 mm (Cernica et al, 2006; Nakazawa et al, 2014c). We selected HD-TOF to transfer triple-MRA into the GKR planning software because it has the best spatial resolution; however, it was co-registered to a different sequence dataset, i.e., a structural T1 weighted MRI scan. The quality of co-registration is known to improve if two datasets of the same kind are used (Nakazawa et al, 2014c). Therefore, if triple-

MRA is to be used in clinical practice two post-contrast T1 weighted MRI scans with the same spatial resolution (preferably submillimetre) should be used for this co-registration step. This was not possible in our study because of the ethical considerations of giving a second injection of gadolinium for research purposes within such a short period of time.

The use of triple-MRA for AVM radiosurgery adds freedom to the planning procedure by enabling the analysis of the AVM architecture in advance. This removes time constraints and team pressure that result from the frame being fitted to the patient while the treatment plan is developed using the traditional DSA based method. This also gives the opportunity to make arrangements for DSA in case triple-MRA images are deemed not optimal for targeting by the radiosurgical team. ASL-MRA and CE-MRA sequences have not yet been assessed and optimised for acquisition with the stereotactic Leksell frame G and distortion issues have been described with 3 T acquisitions using the stereotactic frame (Nakazawa et al, 2014d). For this reason, triple-MRA was performed before the day of GKR. We see as an advantage the opportunity to plan the treatment in advance; however, some radiosurgery planners may not be comfortable delivering GKR based on angiographic images not acquired on the same day of treatment. There is no reason why triple-MRA could not be performed on the same day, apart from limited time for triple-MRA post-processing and co-registration, but also structural remodelling of AVMs which is known to be a slow process is unlikely to significantly alter AVM structure over short periods of time (da Costa et al, 2009). We arbitrarily suggest that triple-MRA should be acquired within days, one week maximum before GKR unless the patient presents with symptoms suggestive of intracranial bleed in which case triple-MRA should be repeated.

In terms of aspects of the study that could be improved, the analysis of a larger number of subjects may have identified subgroups of patients, or AVM features, with extremes of concordance between DSA and triple-MRA volumes. This would have been useful for case selection in future phases of clinical implementation. For instance, previous embolization has been repeatedly described as a confounder on AVM target delineation but in our study

concordance between DSA and triple-MRA volumes in previously embolised patients was not significantly different from previously untreated cases. Our group, however, included only three patients with history of embolization and the performance of triple-MRA for planning of cases with previous embolization may need further attention. The quantification of accuracy of co-registration could have helped to establish how much of the observed discrepancy between triple-MRA and DSA volumes was caused by the use of different imaging techniques, as opposed to other technical factors. Inter-observer variability could have also been removed from our study design if both triple-MRA and DSA volumes were delineated by the same radiosurgical team. This, however, would have resulted in the introduction of recall bias which is more difficult to quantify and could have undermined the validity of the results. Potential improvements of the MRA sequences include the use of vessel selective acquisition of ASL-MRA which could help to avoid vessel superposition issues on MIP and improve characterisation of feeding patterns (Chng et al, 2008; Fujima et al, 2016; Lindner et al, 2015). The improved spatial resolution of HD-TOF in our study was achieved through a compromise between coverage and acquisition time and to this end FOV was reduced to 50 mm in the cranio-caudal direction. This may require altering for planning of large AVMs that are not fully covered by this tight FOV. The arrival of contrast agent was not detected by CE-MRA in one of the patients due to accidental mistiming of the manual gadolinium injection with respect to the dynamic acquisition. This could be improved by the use of an automatic injection pump which results in more consistent boluses and more reproducible injection rates. Future phases of clinical implementation should include thorough and long-term follow-up in order to ascertain if planning of GKR using triple-MRA instead of DSA affects treatment outcomes, i.e. obliteration rates and ARE.

The development of GKR as a treatment for brain AVMs was historically accomplished using DSA and the radiosurgical community have a very high level of confidence in DSA, which is still considered the reference standard method for treatment planning. This has contributed to the limited and hesitant use of MRA as an alternative to DSA in radiosurgery. For that reason, the members of the multidisciplinary team drawing AVM volumes on triple-MRA were asked how

confident they would feel about delivering GKR based on triple-MRA volume. Reassuringly, they stated that they would feel highly confident or confident delivering GKR based on triple-MRA volume in 100 and 86% of the cases (interventional radiologist and consultant neurosurgeon, respectively). This is an encouraging finding which can help promote the use of less invasive imaging methods for AVM patients.

5.6 Conclusions

The technical feasibility of using triple-MRA, instead of DSA, for visualisation and delineation of brain AVMs for GKR targeting has been demonstrated. Target volumes obtained using triple-MRA are on average 10% smaller than AVM targets obtained with the standard DSA planning method which can potentially reduce the risk of ARE. More than 70% of the volume identified as AVM nidus with the standard DSA planning method was also included in the triple-MRA volume. The discrepancies between triple-MRA and DSA volumes are less than the inter-observer variability observed when an AVM target is delineated by different radiosurgical teams.

6. Triple Magnetic Resonance Angiography (triple-MRA) for confirmation of obliteration following Gamma Knife radiosurgery for brain arteriovenous malformations.

Rojas Villabona, A., Benedetta Pizzini, F., Solbach, T., Sokolska, M., Ricciardi, G., Lemonis, C., De Vita, E., Suzuki, Y., Van Osch, M., Foroni, R., Montemezzi, S., Atkinson, Ciceri, E., Kitchen, N., Nicolato, A., Golay, X. & Jager, R.

Under peer review for publication

6.1 Abstract

Introduction: DSA is the reference standard for confirmation of obliteration following GKR of brain AVMs, due to suboptimal diagnostic accuracy of standard MR angiography. However, DSA is invasive and it carries a potential risk of complications. This study aims to evaluate whether a combination of three MRA sequences, referred to as triple-MRA, can be used as an alternative to DSA to confirm AVM obliteration following GKR and to characterise residual AVMs in case of incomplete response.

Methods: Thirty patients undergoing DSA for confirmation of obliteration following GKR for AVMs also underwent triple-MRA including ASL-MRA, HD-TOF and CE-MRA. The DSA and triple-MRA were independently and blindly

evaluated by two observers regarding the presence/absence of a residual AVM. The Spetzler-Martin grading system was used to grade residual lesions on both imaging modalities. Sensitivity, specificity, negative and positive predictive value of triple-MRA for confirmation of AVM obliteration are reported. Diagnostic accuracy of triple-MRA was evaluated using ROC curve analysis and kappa (*k*) coefficient was used to measure agreement between DSA and triple-MRA.

Results: Mean time between GKR and follow-up DSA/triple-MRA was 53 months (95%CI: 42 - 64; range: 22 - 168). One patient was excluded due to suboptimal imaging quality. Total triple-MRA scanning time was 18:11min. Triple-MRA demonstrated AVM obliteration in 20 patients and a residual AVM was detected in 9 subjects by both observers (obliteration rate: 69%). This was in complete agreement with the interpretation of DSA. Triple-MRA showed complete sensitivity and specificity for confirmation of obliteration with maximum positive and negative predictive value (100%). ROC analysis confirmed complete diagnostic accuracy with an area under the curve of 1 ($p < 0.001$) and kappa agreement between DSA and triple-MRA was 1 for both observers ($p < 0.001$).

All nine residual AVMs were identified by both observers on at least two MRA sequences. CE-MRA failed to show the residual lesion in two cases and ASL-MRA in one (false positive rate: 11% and 5%, respectively). There was complete agreement on size and drainage scores between triple-MRA and DSA for both observers in all residual lesions (kappa = 1; $p < 0.003$). Poor agreement was observed between eloquence scores on DSA and triple-MRA due to the limitations of DSA (2D) in terms of anatomical localization.

Conclusion: Triple-MRA consistently demonstrated/ruled out residual AVMs in patients who had undergone GKR for brain AVMs. It provides optimal sensitivity and specificity for confirmation of obliteration following GKR compared to DSA and it can also be reliably used for characterisation of residual AVMs.

6.2 Introduction

AVMs are congenital vascular abnormalities characterised by anomalous connections between arteries and veins leading to arteriovenous shunting through a network of coiled and tortuous vessels, the so-called nidus (Hernesniemi et al, 2008). Brain AVMs most commonly present with spontaneous intracranial haemorrhages and they are a potential source of neurological morbidity and mortality due to the life-long risk of bleeding if left untreated (1.5 - 4.0% per year) (da Costa et al, 2009; Stapf et al, 2006). GKR is a well-established minimally invasive treatment for selected patients with brain AVMs (Mohr et al, 2013; van Beijnum et al, 2011). It produces a detectable decrease in blood flow through the AVM nidus a few months after treatment which gradually progresses so that by two to three years approximately 75% of the AVMs are completely obliterated (Koltz et al, 2013). The risk of intracranial bleed persists until complete obliteration of the nidus is achieved and for this reason it is imperative to confirm AVM cure after treatment (Kano et al, 2013).

Intra-arterial DSA has been traditionally used for confirmation of obliteration following GKR and it is currently considered the reference standard for detection and characterization of AVMs, due to the limited spatial and temporal resolution of other vascular imaging techniques (Giesel et al, 2010; Khandanpour et al, 2013; Lee et al, 2015; Soize et al, 2014). Most GKR centres around the world use regular MRI and MRA for follow-up (every 6 or 12 months) but patients still undergo DSA to confirm cure a few years after treatment; usually once obliteration is suggested by MRI/MRA (Pollock et al, 2016; Starke et al, 2017). Although widely used, DSA conveys some risk of complications (Bendszus et al, 1999). Kaufmann et al reported the complication data of 19826 consecutive patients undergoing DSA from 1981 to 2003 and reported neurological complications in 522 examinations (2.63%). Twenty-seven of these (0.14%) were strokes with permanent disability, twelve deaths occurred (0.06%) and access site hematoma (4.2%) was the most common complication overall (Kaufmann et al, 2007). DSA also exposes both patients and medical staff to ionizing radiation and

it carries a risk associated with injection of iodinated contrast agents. Furthermore, it is an unpleasant experience for patients due to pain, invasiveness and prolonged bed rest after the procedure (Fifi et al, 2009). Finally, the cost associated with DSA examinations can also be significant.

The potential to improve follow-up procedures after GKR by using less invasive imaging methods has been described elsewhere and important attempts have been made using MRA as an alternative to DSA (Buis et al, 2012; Lee et al, 2015; Lim et al, 2012; Soize et al, 2014). Lee et al retrospectively reviewed the MRI and TOF MRA of 136 patients who had undergone GKR and reported a sensitivity of 76-85% and specificity of 89-95% compared to DSA (Lee et al, 2015). Similarly, poor results in terms of sensitivity had been previously published by Buis et al using 3D TOF only (Buis et al, 2012). Lim et al reported good sensitivity for confirmation of AVM obliteration (above 90%) using contrast-enhanced (CE) time-resolved MRA but the specificity fell short of 80% which was prospectively replicated by Soize et al (Lim et al, 2012; Soize et al, 2014). The studies above concluded that individually, TOF and CE-MRA have good diagnostic accuracy and their inclusion on standard follow-up protocols was supported; however, due to the suboptimal sensitivity and specificity they recommended that DSA should still be performed to confirm AVM obliteration.

MR vascular imaging has continued to develop with the optimisation of MRA sequences at higher field strengths and the combination of parallel imaging with intelligent sampling of the *k*-space, which has resulted in higher spatial resolution and sub-second temporal resolution (Chang et al, 2015; Hadizadeh et al, 2011). Also, the introduction of ASL based angiography has allowed the acquisition of time-resolved cerebral angiography with temporal resolution comparable to that of DSA (100 - 200 ms), without the administration of contrast agents (Lindner et al, 2015; Suzuki et al, 2017; Wu et al, 2013). ASL-MRA has already proved to be useful for non-invasive assessment of cerebral AVMs, providing dynamic information of flow and angio-architecture which had not been previously obtained with MRA (Fujima et al, 2016; Iryo et al, 2016).

None of currently available angiography sequences has been shown to reliably confirm/rule out the presence of residual AVMs in patients treated with GKR. They differ in terms of spatial and temporal resolution and rely on different contrast mechanisms to depict the unpredictable and heterogeneous structure and flow observed in AVMs. We hypothesise that the combined use of TOF, CE and ASL MRA results in optimal sensitivity and specificity for detection of residual AVMs. This study aims to evaluate whether the combination of these three MRA sequences, referred to as triple-MRA, can be reliably used as an alternative to DSA for confirmation of AVM obliteration after GKR and to characterise residual AVMs in cases with incomplete response.

6.3 Methods

6.3.1 Patients

Thirty consecutive adult patients undergoing DSA for confirmation of obliteration following GKR of brain AVMs at University Hospital of Verona between November 2014 and December 2016 were prospectively recruited. The decision to perform a follow-up DSA had been independently made by the clinical multidisciplinary team before recruitment and all participants gave written consent for a triple-MRA to be performed on the same day of DSA. The study was approved by London Queen Square Research Ethics Committee (UK) and Verona and Rovigo Ethics Committee for Clinical Research (Italy) (Appendix 4). Patients unable to tolerate MR imaging without sedation/anaesthesia and those with altered renal function (eGFR > 30 ml/min) were excluded. Inability to consent, pregnancy, history of allergic reaction to gadolinium based contrast agents and contraindication to MRI (i.e., pacemakers, metallic implants, etc.) were also exclusion criteria.

Table 6.1 shows the demographic details and AVM characteristics of the study subjects. The mean age was 37y (range: 18 - 69) and 66% of participants were female. The mean AVM volume at the time of GKR was 7.01 ml (range: 0.07 - 50.54; SD: 9.8) and the AVMs were well distributed across the head anatomy

with nine AVMs being located in the temporal lobe, six in the frontal lobe, six parietal and three occipital. Four were deep seated (basal ganglia or brainstem) and two were located in the posterior fossa. Ten patients (33.3%) had undergone glue embolization and 3 (10%) microsurgical resection before GKR. One of them had received GKR twice for the same AVM. No patients presented with intracranial bleeds or received further treatments after GKR.

Table 6.1. Demographic details and AVM characteristics of the study subjects.

Age mean (min - max)		37 y (18 - 69)
Female, %		66%
AVM location, n (%)	Temporal	9 (30%)
	Frontal	6 (20%)
	Parietal	6 (20%)
	Occipital	3 (10%)
	Basal ganglia/brainstem	4 (13%)
	Post fossa	2 (7%)
Lateralisation, %	Right	30%
	Left	70%
AVM volume mean (min - max)		7.01 ml (0.07 - 50.54)
GKR, mean (min - max)	Dose	17 Gy (11 - 22)
	Percentage isodose	50%
Mean time post-GKR (min - max)		53 mo (22 - 168)

6.3.2 MRA imaging

Triple-MRA included 4D ASL-MRA, HD-TOF and CE-MRA. They were acquired using an 8-channel head-coil on an Achieva 3.0 T MRI system (Philips Healthcare Systems, Best, The Netherlands) and the scanning parameters are shown in Table 6.2. Total triple-MRA scanning time was 18:11min.

ASL-MRA labelling was performed with the STAR method and a labelling slab of 300 mm positioned 20 mm below the imaging plane (Nakamura et al, 2012). The echo-planar imaging (EPI) acceleration method (Suzuki et al, 2017) enabled the acquisition of 8 dynamic phases with a temporal resolution of 200 ms and six

minutes' acquisition time. HD-TOF was based on a 3D T1 fast-field echo (FFE) acquisition (RF-spoiled, gradient echo) with flow compensation and TONE across the slab (Wrede et al, 2014). Four slabs covering 50 mm in the cranio-caudal direction were obtained with a parallel imaging SENSE factor of 2. CE-MRA included 24 dynamic sagittal acquisitions using a 3D, T1 weighted, FFE sequence. A reference scan was acquired before contrast injection for subtraction of the stationary tissue and dynamic sampling was started at the time as the injection. The fast dynamic acquisition used CENTRA and the keyhole method with 20% of the *k*-space collected per keyhole frame (Willinek et al, 2008). SENSE was employed with a reduction factor of 4 in the phase-encoding direction and 2 in the slice-encoding direction achieving a temporal resolution of 608 ms/phase. An intravenous injection of 0.1 ml/kg of Gadobutrol 1.0 mmol (Gadovist®; Bayer plc, UK) was given with an automated power injector at a flow rate of 3.5 ml/s and it was followed by 20 ml of normal saline flush injected at the same flow rate.

MIPs of the individual MRA sequences were generated in the orthogonal planes (anteroposterior, lateral and cranio-caudal) and transferred to OsiriX DICOM viewer 8.4 (Pixmeo Sarl, Switzerland) for assessment.

6.3.3 DSA imaging

DSA was performed under local anaesthesia using a AlluraXper biplane angiography system (Philips Healthcare Systems, Best, The Netherlands) and iodinated contrast agent (Iohexol, Omnipaque, 240 mg/ml). A femoral artery approach was used for selective contrast injection of one or several vessels known to supply the previously treated AVM. DSA was performed at a rate of 3-7 frames/second in standard anteroposterior, lateral and oblique projections, where necessary.

Table 6.2. Scanning parameters of triple-MRA sequences.

Parameter	ASL-MRA	HD-TOF	CE-MRA
MRA type	Dynamic	Single time point	Dynamic
Scan duration (min:sec)	5:58	08:54	3:19
Contrast			
Scan mode	3D	3D	3D
Acquisition	T1 TFEPI	T1 FFE	T1 FFE
T_R (ms)	12	25	3
T_E (ms)	5	3	1
Flip Angle	10	20	25
Resolution			
FOV (RL x AP x CC, mm)	210 x 210 x 90	250 x 250 x 50	150 x 210 x 210
Acquisition	transversal	transversal	sagittal
Slabs	1	4	1
Acquisition matrix	172 x 172 x 70	832 x 568 x 50	50 x 248 x 248
Acquired voxel size (mm)	1.22 x1.26 x 1.3	0.3 x 0.44 x 1	3 x 0.85 x 0.85
Reconstruction matrix	256 x 256	1936 x 1936	288 x 288
Rec voxel size (mm)	0.82 x 0.82 x 0.65	0.13 x 0.13 x 0.5	1.5 x 0.73 x 0.73
Number of slices	140	100	100
SENSE factor	2.5/1	2/1	4/2
Dynamic acquisition			
Dynamic imaging mode	TFEPI	-	CENTRA keyhole
Number of phases	8	-	24
Phase interval (temporal resolution)	200 ms	-	608 ms
Label delay	200 ms	-	-
Contrast	-	-	Gadovist 0.1ml/Kg IV pump injection: 3.5ml/sec

6.3.4 Data analysis

DSA and triple-MRA were evaluated by two independent observers regarding the presence/absence of a residual AVM (Appendix 5). The observers were a neuroradiologist with 13 years of experience (FBP) and an interventional neuro-radiologist with 15 years of clinical practice (TS). They were blinded to patient's demographics, date of examination, previous clinical assessment and reports. The anonymized DSA and triple-MRA examinations were randomly numbered and reviewed in different sessions to prevent reporting bias. In order to simulate the clinical scenario in which assessment of cerebral angiographies is aided by pre-existing knowledge of size and location of treated AVMs, the observers had access to anonymized images of the stereotactic DSA and post-contrast T1 MRI -performed on the day of GKR- for comparison with follow-up DSA and triple-MRA, respectively. Figure 6.1 shows a representative example of the datasets available to the observers for evaluation. The observers also reported which of the MRA sequences showed the lesion in cases with residual AVMs and this enabled the calculation of specificity and false positive rate for individual MRA sequences.

AVM obliteration was defined as the complete absence of a nidus and arteriovenous shunt (early-filling draining veins). The Spetzler-Martin grading system (size: < 3 cm, 3 - 6 cm and > 6 cm; venous drainage: deep vs superficial only; eloquence of adjacent brain: eloquent vs. non-eloquent) was used to grade residual lesions on both imaging modalities (Spetzler & Martin, 1986). Further characterisation of residual AVMs included the identification of feeding arteries and draining veins. The quality of triple-MRA was evaluated in regards to artefacts that could have affected the quality of radiological assessment. Vessel visualization was assessed for each MRA sequence using a five-point categorical scale (poor, fair, good, very good, excellent). The observer's level of confidence on their assessment of the absence/presence of a residual AVM on DSA and triple-MRA was reported using a three-point categorical scale (not entirely confident, confident, highly confident).

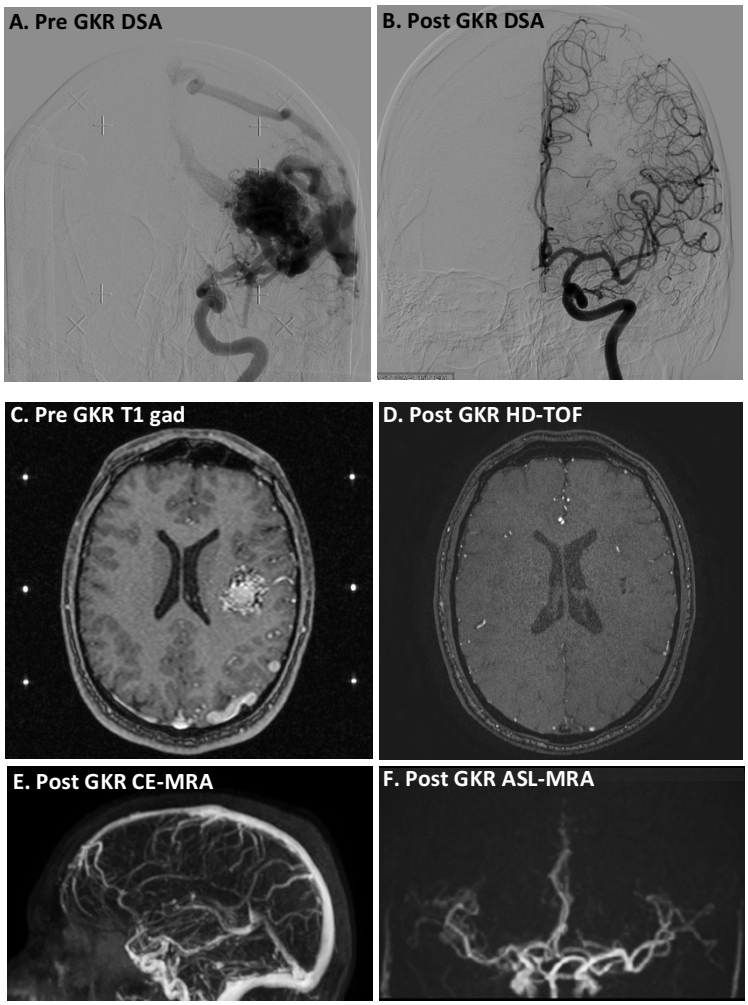

Figure 6.1. Representative example of DSA and triple-MRA datasets presented to the independent observers for review in a case with complete AVM obliteration. DSA (top row) and triple-MRA series (C-E) were reviewed in different sessions. The stereotactic DSA performed on the day of GKR (A, note fiducial crosses) was available to the observers and it served as an aid for the assessment of follow-up DSA (B). Similarly, the stereotactic T1 MRI with contrast (C, note stereotactic fiducial markers) was used as a guide for the evaluation of triple-MRA, which included HD-TOF (D), CE-MRA (E) and ASL-MRA (F). No residual nidus or AV shunt is noted in any of the post GKR images.

The sensitivity, specificity, negative predictive value (NPV) and positive predictive value (PPV) of triple-MRA for detection of AVM obliteration were calculated. Sensitivity was defined as the probability of confirming obliteration on triple-MRA among those cases demonstrating complete obliteration on DSA. Specificity was the probability of finding a residual AVM among those with a residual on DSA. PPV was the percentage of cases with complete obliteration on triple-MRA and in whom this was confirmed on DSA. NPV was the percentage of patients found to have a residual AVM on triple-MRA and in whom this was confirmed on DSA. Additionally, the diagnostic performance or accuracy of triple-MRA, as well as individual MRA sequences, to discriminate between patients with residual AVMs and complete obliteration was evaluated using Receiver Operating Characteristic (ROC) curve analysis (Metz, 2008). For interpretation of ROC analysis 1 is complete agreement while 0 denotes no agreement other than what would be expected by chance. Weighed Cohen's kappa (*k)* coefficient was calculated to measure agreement between DSA and triple-MRA for obliteration and Spetzler-Martin grade for each observer (Chng et al, 2008). *k* was interpreted as follows: $k \leq 0.20$ = poor; $k = 0.21$-0.40, fair; $k = 0.41$-0.60, moderate; $k = 0.61 - 0.80$, good; $k = 0.81 - 0.90$, very good; and $k \geq 0.91$, excellent (Machet et al, 2012). Statistical significance was defined as a p value of < 0.05 and analyses were performed using the Statistical Package for the Social Sciences (SPSS Statistics, Version 23. IBM Corp).

6.4 Results

6.4.1 Confirmation of AVM obliteration

The mean time between GKR and follow-up DSA/triple-MRA was 53 months (95%CI: 42-64; range: 22-168). In one case the AVM region of interest was not included in the HD-TOF field of view and arrival of contrast agent was not detected by CE-MRA due to mistiming of the gadolinium injection with respect to the dynamic acquisition. This case was excluded and final statistical analysis included 29 patients.

Triple-MRA demonstrated AVM obliteration in 20 patients and a residual AVM was detected in 9 subjects by both observers, which resulted in an obliteration rate of 69%. This was in complete agreement with both their own interpretation of DSA as well as the clinical reports produced by the interventional radiologist who performed the DSA procedure. Triple-MRA showed 100% sensitivity and specificity for confirmation of obliteration of brain AVMs with maximum positive and negative predictive value. ROC analysis demonstrated complete diagnostic accuracy of triple-MRA for confirmation of obliteration, with an area under the curve of 1, $p < 0.001$(Figure 6.2). The weighted Cohen's kappa coefficient for obliteration status between DSA and triple-MRA was 1 ($p < 0.001$) for both observers.

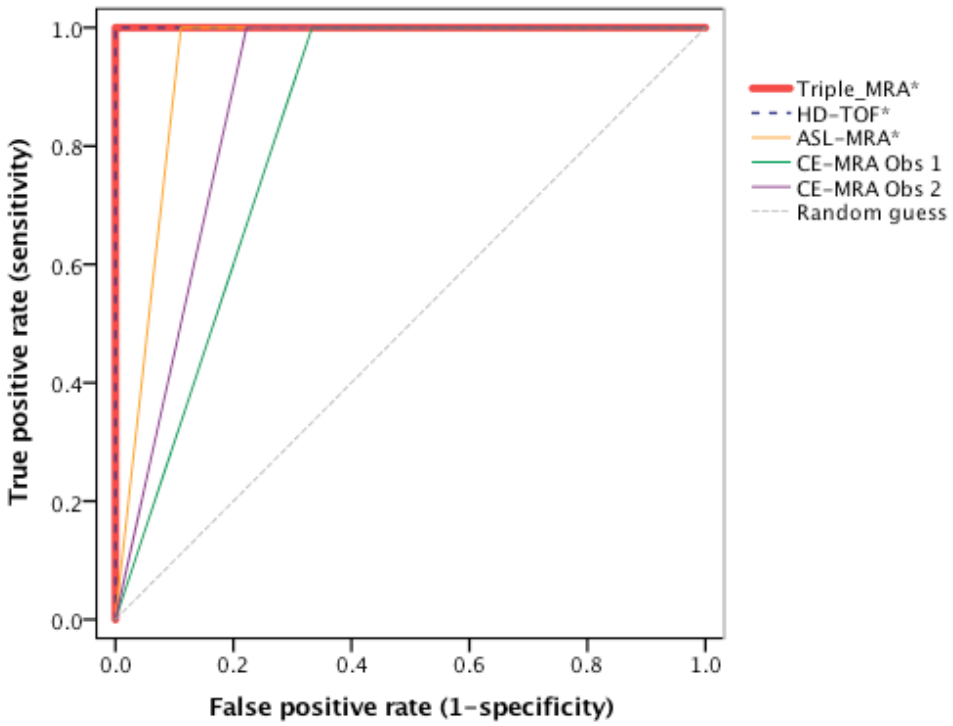

Figure 6.2. Diagnostic accuracy (ROC curve) of triple-MRA and individual MRA sequences for confirmation of AVM obliteration following GKR.

* Identical results/curve obtained for both observers.

Table 6.3 shows the interpretation of individual MRA sequences including their specificity, PPV and false positive rate. This is based on whether residual AVMs were visualised on individual MRA sequences during triple-MRA assessment rather than an entirely independent evaluation of each sequence. All residual AVMs were detected by both observers on HD-TOF which had the best specificity of all three MRA sequences. In two cases the residual lesion was detected on ASL-MRA and HD-TOF but not on CE-MRA due to the very small size of the residual lesion in one (6 mm, Figure 6.3) and the diffuse nature of the residual AVM nidus in the second case. In one patient, the residual AVM was identified in all three MRA sequences by one observer but it was reported as not detectable on CE-MRA by the other. This resulted on a 11-17% false positive rate for CE-MRA which also showed the lowest specificity of all three MRA sequences (67-78%). ASL-MRA failed to show the residual AVM in the case presented in Figure 6.4g. The ROC area under the curve for the MRA sequences, i.e., HD-TOF, ASL-MRA and CE-MRA, was 1, 0.94 and 0.83-0.89, respectively.

Table 6.3. Confirmation of obliteration with triple-MRA and DSA following GKR of brain AVMs.

	DSA/triple-MRA n: 29	**ASL-MRA n: 28[a]**	**HD-TOF n: 29**	**CE-MRA n: 24[b]**	
Observer	**1 and 2[c]**	**1 and 2[c]**	**1 and 2[c]**	**1**	**2**
Obliterated	20	20 (+1)[a]	20	18 (+5)[b]	17 (+5)[b]
Residual	9	8	9	6	7
Response rate	69%	71%	69%	75%	71%
Specificity	-	89%	100%	67%	78%
PPV	-	95%	100%	83%	89%
False positives n (rate)	-	1 (5%)	0	(3) 17%	(2) 11%

[a] ASL-MRA was not available in one patient in whom DSA showed complete obliteration.

[b] Arrival of contrast on CE-MRA was not depicted in 5 subjects, in whom DSA demonstrated complete obliteration, due to accidental mistiming of the gadolinium injection with respect to the dynamic acquisition.

[c] Same results obtained by both observers.

6.4.2 Characterisation of residual AVMs in cases of incomplete response

Table 6.4 shows the interpretation of DSA and triple-MRA regarding Spetzler-Martin grading of residual AVMs by both observers. The kappa coefficient -of agreement- between DSA and triple-MRA for Spetzler-Martin grade was 0.85 ($p < 0.001$) for the first observer and 0.55 ($p = 0.004$) for the second due to disagreements on the eloquence part of the grading system. There was complete agreement on size and drainage scores between triple-MRA and DSA for both observers in all nine residual lesions (kappa = 1; $p < 0.003$). Different eloquence scores on DSA and triple-MRA were noted in one case for the first observer (kappa = 0.78; $p < 0.016$) and in three cases for the second observer (kappa = 0.31; $p = 0.34$). This was the result of limited anatomical localization on DSA images (2D) compared to triple-MRA as follows. In the first case a residual AVM located on the left cerebellar peduncle was incorrectly considered as non-eloquent on DSA by the first observer. Observer 2 considered the left frontal residual AVM shown in Figure 6.3 and a residual lesion located in the right temporo-parietal lobe to be in eloquent areas on DSA but their assessment on triple-MRA demonstrated non-eloquent location. Also, a temporo-parietal residual AVM was considered to be non-eloquent on DSA by the second observer but triple-MRA demonstrated its eloquence (Wernicke's area). There was no difference on the assessment of eloquence of the affected brain using triple-MRA between the two observers in all cases.

Observer 1 identified a total of 14 feeding arteries and 13 draining veins both on DSA and triple-MRA. Observer two identified 17 feeding arteries and 15 draining veins on DSA but only 15 and 12 on triple-MRA, respectively (Table 6.4). The same blood vessel was identified by both observers as the main feeding artery on DSA and triple-MRA for eight out of nine residual AVMs. In one case, observer 1 named the superior cerebellar artery as the only feeder on DSA and the posterior cerebral artery on triple-MRA, while observer 2 named the same feeding vessels but in the opposite set of investigations, i.e. superior cerebellar artery on triple-MRA and posterior cerebral artery on DSA.

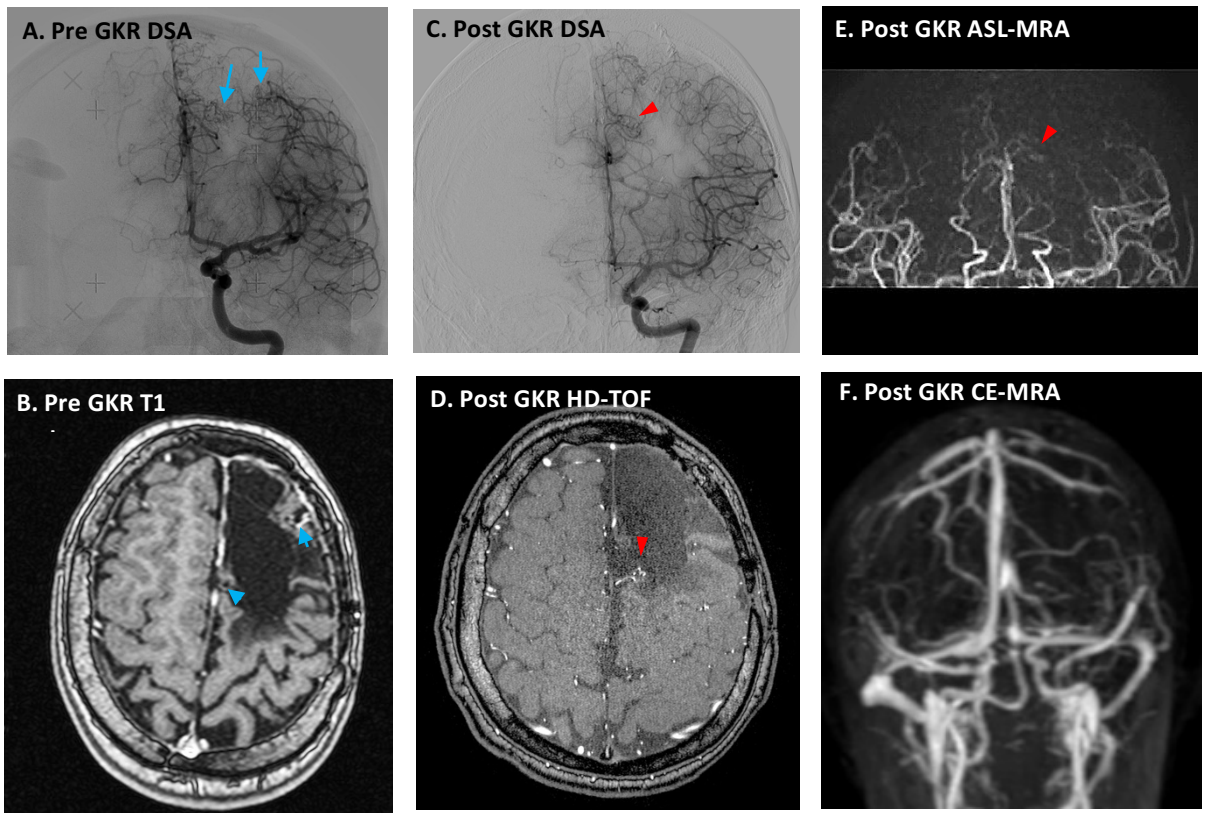

Figure 6.3. Representative case of confirmation of AVM obliteration using triple-MRA. The pre GKR DSA (A) and MRI (B) showed two AVM nidi (blue arrows) at the time of GKR in a patient with previous partial surgical excision of a ruptured AVM. The most lateral nidus is not identified in post GKR imaging; however, a residual of the most medial nidus (red arrow heads) is identified in post GKR HD-TOF (D) and ASL-MRA (E). These findings are confirmed by post GKR DSA (C). The small size of the lesion renders it not identifiable in the CE-MRA (F).

The characterisation of residual AVMs in terms of size, location and feeding/draining vessels relied on the combined use of all three MRA sequences. Figure 6.4 demonstrates how each of the sequences provided relevant details of the angio-architecture and flow dynamics of the nidus and enabled complete characterisation of the AVM in two representative cases. The location and size of the AVM nidus in the first case (right occipital residual AVM, 4A-D) are demonstrated on HD-TOF, while the dynamic MRA sequences confirmed blood supply from the middle meningeal artery (ASL-MRA) and venous drainage through the superficial system only (CE-MRA). The combination of three MRA sequences was also important in cases where one of them failed to show the residual AVM as shown in the second case in Figure 6.4e-h.

Table 6.4. Characterisation of residual AVMs using triple-MRA compared to DSA.

			Observer 1		Observer 2	
			DSA	**t-MRA**	**DSA**	**t-MRA**
SMS	**Size**	< 3 cm	7	7	7	7
		3-6 cm	2	2	2	2
		> 6 cm	-	-	-	-
	Drainage	Superficial only	5	5	5	5
		Deep	4	4	4	4
	Eloquence	Non-eloquent	5	4	3	4
		Eloquent	4	5	6	5
Feeding arteries			14	14	17	15
Draining veins			13	13	15	12

6.4.3 Image quality and reporting level of confidence

The most common issue affecting image quality was failure to depict the arrival of contrast agent on CE-MRA due to mistiming of the gadolinium injection with respect to the dynamic acquisition. This occurred in six cases but was found to significantly affect the quality of the radiological assessment only in one patient (excluded) in whom HD-TOF was also unsatisfactory due to the AVM region of interest not being included in the acquired volume. In the remaining five cases, the other two MRA sequences were optimal in terms of acquisition and image quality and they provided a good degree of confidence for confirmation of obliteration. ASL-MRA was not available in one patient due to a temporary failure of the scanner software. All cases with incomplete triple-MRA datasets (i.e. missing ASL-MRA or CE-MRA) were subjects in whom complete obliteration was demonstrated on DSA. A blood vessel doubling or "ghosting" artefact was observed on the ASL-MRA sequence in the majority of cases. This affected mainly the larger vessels of the circle of Willis and was more evident in the AP direction. This artefact was thought to be of no consequence for the quality of the radiological assessment. Minor motion artefacts were observed in two patients, affecting mainly the CE-MRA acquisition.

Vessel visualization on HD-TOF was reported as very good or excellent in 96 and 90% of the cases by observer 1 and 2, respectively. They also considered vessel visualisation to be good or very good in more than 90% of the patients for ASL-MRA and 80% for CE-MRA. There was no difference in the observer's level of confidence on the assessment of triple-MRA and DSA regarding the absence/presence of a residual AVM (Figure 6.5).

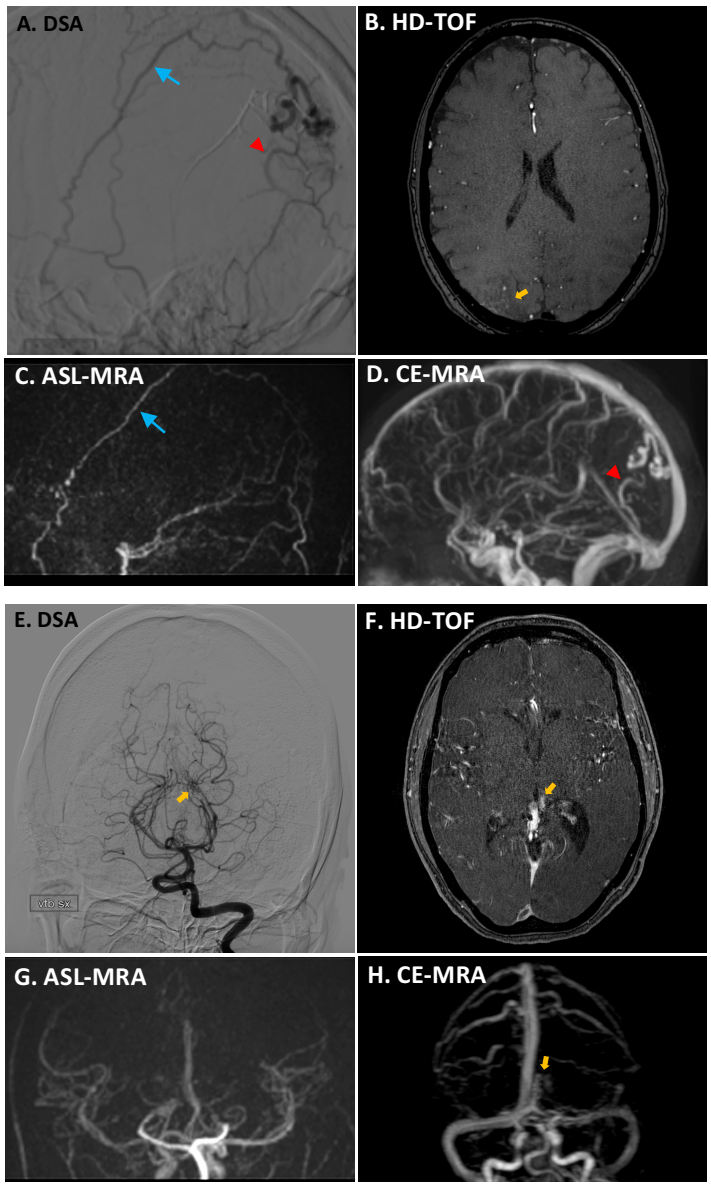

Figure 6.4. Combined use of three MRA sequences for identification and characterisation of residual AVMs in two representative cases. The DSA (A) and HD-TOF (B) of the first case demonstrates a residual < 3 cm in diameter AVM nidus (yellow arrow) located on the right occipital lobe. ASL-MRA (C) depicts the middle meningeal artery (blue arrow) feeding the AVM nidus while the superficial venous drainage (red arrowhead) is visualized on CE-MRA (D). In the second case (E-H), the identification of a small nidus (yellow arrow) on HD-TOF (F) and CE-MRA (H) provides convincing evidence of the presence of a residual AVM, despite this not being visible on ASL-MRA (G).

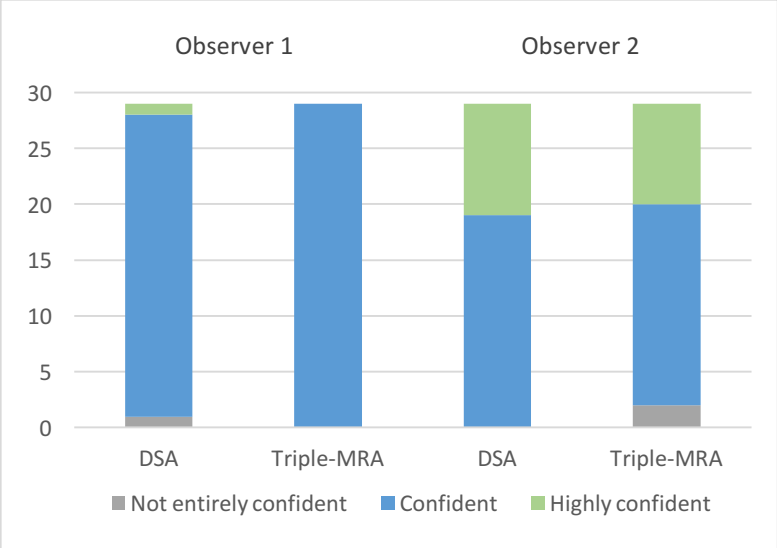

Figure 6.5. Observer's level of confidence on the assessment of triple-MRA and DSA regarding the absence/presence of a residual AVM.

6.5 Discussion

This work presents a detailed evaluation of triple-MRA for confirmation of obliteration of brain AVMs following GKR in comparison to DSA. The triple-MRA and DSA of 30 patients who attended follow-up imaging to confirm obliteration of brain AVMs following GKR, were blindly assessed by two independent observers. The combined use of ASL-MRA, CE-MRA and HD-TOF was shown to be a reliable method to confirm/rule out the presence of residual AVMs after radiosurgery. Triple-MRA showed maximal sensitivity and specificity, which makes this the first study demonstrating satisfactory diagnostic accuracy of MRA for confirmation of obliteration following GKR of brain AVMs compared to DSA. This study supports the use of triple-MRA as a first line modality for confirmation of obliteration following GKR which is of high clinical relevance, because triple-MRA can not only avoid unnecessary DSA examinations for patients with cured AVMs (69% in our study group) but it can also help rationalize its use in patients with residual AVMs, who may need further DSAs for embolization or repeated GKR.

The major accomplishment of triple-MRA is the combination of temporal and

spatial resolution, which are necessary to appreciate the dynamic characteristics of AVMs (Khandanpour et al, 2013). AVMs exhibit a high degree of heterogeneity in terms of angio-architecture and flow dynamics and even within the same lesion there may be dramatic and unpredictable differences in terms of vessel configuration and blood flow (Stapf et al, 2006). For this reason, AVMs are very difficult to characterise fully using a single MRA sequence. Previous studies have used individual MRA sequences, either TOF or CE-MRA along with structural MRI, in an attempt to image residual AVMs (Buis et al, 2012; Lee et al, 2015; Lim et al, 2012; Soize et al, 2014). These sequences, however, rely on contrast mechanisms which cannot by themselves account for all the possible variations in flow and velocity to optimally portray abnormal blood vessels in AVMs. If used independently they tend not to capture all the complexity and heterogeneity of shapes, sizes and velocities seen on AVMs. However, as it has been demonstrated in this study, in combination as triple-MRA they form a robust method to detect/rule out the presence of residual AVMs after GKR by reducing the chances of false positives and false negatives and by providing both structural and dynamic information of residual lesions to allow their characterization.

The use of multiple sequences for diagnostic purpose is common place in radiology and it is well accepted that information from multiple sources such as T1, T2 and contrast enhanced imaging may be required to achieve full diagnosis. The combination of several sequences or imaging techniques has proved to be even more valuable in vascular imaging where for instance a number of physiological parameters such as cerebral blood volume, cerebral blood flow and mean transit time are measured to understand the abnormalities of cerebral perfusion (Karonen et al, 2000; Kennan & Jäger, 2003). Dynamic contrast enhanced and dynamic susceptibility contrast MR perfusion imaging are also frequently used in combination to obtain these parameters which cannot be obtained using a single acquisition (Shin et al, 2014). CE-MRA and TOF angiography have been used in combination for follow-up of intracranial aneurysms treated by flow diverter and a combination of ASL-perfusion and CE-MRA is a promising strategy for non-invasive assessment of cerebral AVMs, providing functional information that so far has been gained only with DSA

(Kukuk et al, 2010; Shin et al, 2014).

We have demonstrated that triple-MRA is comparable to DSA for confirmation of obliteration following GKR, but of course this does not provide any evidence that triple-MRA is equivalent to DSA for other uses. In this study, the observers were aided by a very high index of suspicion because they were aware of the location of AVMs at treatment and therefore knew where to look for residual lesions. Triple-MRA assessment was designed to replicate the clinical scenario in which DSA examinations are reviewed specifically to confirm obliteration. Results might have been different if the observers had no indication of the potential findings or location.

A completely independent review of each MRA sequence to assess their ability to individually confirm AVM obliteration was not part of our study design. The observers simultaneously viewed all three MRA sequences but indicated subsequently which of them showed the residual AVMs (Appendix 5). Although HD-TOF (but not the other MRA sequences) was found to demonstrate the residual nidi in all DSA positive cases (specificity: 100%; NPV: 100%; no false positives), we cannot conclude that this would have been the case if HD-TOF had been the only MRA modality available. It might be tempting to argue that HD-TOF on its own is as good as DSA, or triple-MRA, due to the result of ROC area under the curve of 1. However, the combined assessment of all three MRA sequences is highly likely to have resulted in a degree of crossed reinforcement or reassurance of findings between the individual sequences. In fact, less than optimal sensitivity and specificity of TOF have been repeatedly demonstrated in previous studies (Buis et al, 2012; Lee et al, 2015) and this motivated the development of triple-MRA by combining multiple MRA sequences. Lee et al, for instance, studied a group of 136 patients who had undergone GKR and retrospectively reviewed their MRI and TOF. They reported that in 5-10% of the cases TOF showed apparent obliteration, although a residual AVM was found on DSA (false positives) (Lee et al, 2015). This is a recognised weakness of TOF and convincing explanations have been proposed for it. During a TOF acquisition, the static tissue is repeatedly excited with RF pulses reducing the steady-state

magnetization signal (signal saturation). Unsaturated blood flowing into the excited volume gives considerably more MR signal than the background tissue creating the blood-to-background contrast known as TOF (Bosmans et al, 1995). As a consequence, a slow flowing residual AVM -or parts of it- can pass undetected on TOF if blood passage through the nidus is not fast enough to give more signal than the background tissue. This is likely to be the case at late stages of blood vessel stenosis which occurs for AVM obliteration following radiosurgery (Schneider et al, 1997). The TOF effect is known to improve at higher magnetic field strength due to increase in the T_1 of static tissue which improves its saturation as well as the inherent increase in bulk magnetization (MacDonald & Frayne, 2015). Also, it has also been previously demonstrated that stronger magnetic fields result in visualisation of more and smaller blood vessels (Kang et al, 2009). Therefore, the use of a stronger magnetic field (3 T) in our study could partly explain the apparent improved performance of HD-TOF compared to previous studies which used 1.5 T magnets (Buis et al, 2012; Lee et al, 2015).

The limitations of TOF are not restricted to overestimation of the true obliteration rate. Buis et al retrospectively reviewed the TOF (1.5 T) and T2 weighted MRI of 120 patients after GKR to assess their ability to correctly determine nidus obliteration compared to DSA (Buis et al, 2012). They found that obliteration was demonstrated on DSA in 48% of the cases in which the AVM appeared to be patent on TOF (false negatives) and this resulted in very low sensitivity (0.52) and NPV (0.55-0.62). During a TOF acquisition, tissues with very short T_1s, such as hematoma or stagnated blood, might produce hyper-intense signal similar in appearance to residual AVMs which is likely to explain the reported rate of false negatives (Bednarz et al, 2000). Buis et al also found that a nidus size < 10 mm was a major limiting factor for reliable assessment of obliteration using TOF and a similar size threshold had been previously described with magnitude contrast MR angiography (Buis et al, 2012; Mukherji et al, 1995). This was not the case in our study where lesions as small as 6 mm (Figure 6.3d) and 8 mm (Figure 6.4f) were visualized adequately on HD-TOF. The higher spatial resolution of HD-TOF in our study (0.3 x 0.44 x 1 mm acquired voxels), directly resulting from the use

of higher field strength, is likely to have contributed to the improved AVM detection rate in our study. Although, some methodological issues in those studies could have also contributed to their poorer results. For instance, in the studies discussed above MRA and DSA were not acquired on the same day and a time interval of up to six months was noted between DSA and MRA in one of them (Buis et al, 2012). Also, we did not include in the assessment of obliteration a contrast enhanced T1 sequence which is known to cause underestimation of nidus obliteration due to contrast enhancement of scar tissue and post-radiosurgical changes (Lee et al, 2015; Warren et al, 2001). There are reasons to believe that our HD-TOF did provide better accuracy than the sequences used in previous studies but TOF angiography still lacks temporal information which is a major limitation that renders it inherently inadequate for the evaluation of dynamic abnormalities such as AVMs. It relies exclusively on visualisation of the AVM nidus for identification of AVMs, as opposed to dynamic MRA sequences which can demonstrate arteriovenous shunting (Figure 6.6), and by itself it is not suitable for characterisation of residual AVMs. Therefore, it is convenient to combine multiple MRA sequences including dynamic acquisitions such as CE and ASL-MRA.

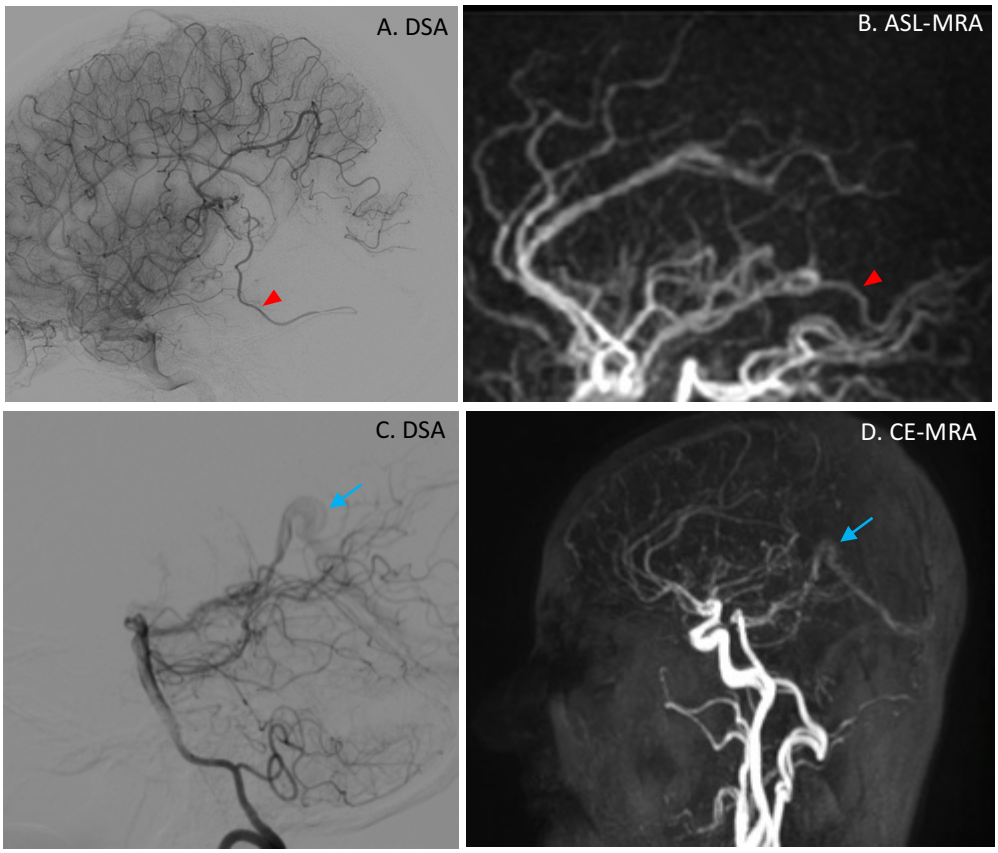

Figure 6.6. Identification of residual AV shunt using ASL-MRA and CE-MRA in two cases with residual AVMs after GKR. In the top row case, a residual AV shunt is demonstrated with ASL-MRA (B) by visualising an early filling draining vein (red arrow heads) which is also depicted by DSA (A). The CE-MRA of the second case (bottom row) shows the early filling of the straight sinus (blue arrows) confirming the presence of residual arteriovenous shunting (C).

Four-dimensional CE-MRA, also referred to as TRICKS, TWIST or TRAK, has been shown to have good accuracy for AVM detection and optimal agreement with DSA on nidus size and type of venous drainage (Machet et al, 2012). The main strength of CE-MRA for AVMs assessment after radiosurgery is the fact that it can depict AV shunting (Figure 6.6), which is relevant not only for the evaluation of AVM obliteration but also for characterisation of residual lesions. In our study, CE-MRA not only contributed to the cumulative evidence of triple-MRA for assessment of obliteration but it was also very important in the case in which the residual AVM was not visualized on ASL-MRA (Figure 6.4). The latter

demonstrates how the three sequences complement each other and the use of multiple acquisition methods increases the chances of AVM detection. Furthermore, although CE-MRA cannot depict all residual AVMs, it is very useful in cases with residual AV shunt/nidus because it enables the characterisation of residual lesions in terms of feeding arteries and draining veins. This was also the conclusion of previous studies that compared CE-MRA with DSA for confirmation of obliteration after radiosurgery (Lim et al, 2012; Soize et al, 2014). These studies reported diagnostic accuracy for detection of residual AVMs as opposed to confirmation of obliteration which was the objective of our study and the TOF papers mentioned above. This posed some difficulties for comparison between papers given that a positive result on CE-MRA studies (residual AVM present) was considered a negative result for us (no obliteration achieved). For this reason, the results by Soize et al and Lim et al have been re-termed to facilitate comparison.

Soize et al used SENSE in combination with Half-Fourier imaging, CENTRA and keyhole *k*-space filling to achieve a temporal resolution of 1.4 seconds per volume (Soize et al, 2014). They found that all the cases with no residual AVM on DSA also appeared to show complete obliteration on CE-MRA, i.e. no false negative cases, 100% sensitivity for obliteration and negative predictive value 100%. However, they also found a 15% false positives rate which was the result of residual AVMs visualized on DSA not showing up on CE-MRA (specificity: 73.7% and PPV: 78.3%). In our study group, at least two residual AVMs that were detected on DSA, HD-TOF and ASL-MRA were not visible on CE-MRA. The resultant false positive rate (11-17%), specificity (67-78%) and PPV (83-89%) are comparable to the estimates by Soize at al. Similar findings were reported by Lim et al who prospectively examined 35 patients with CE-MRA and found that in 13-15% of the cases in which CE-MRA demonstrated complete obliteration, there was actually a residual on DSA (false positive). The unseen nidi in previous studies were very small and they proposed that suboptimal spatial resolution was to account for this, along with heterogeneity of the nidus such as in cases with previous embolization. However, our false positives (residual AVMs not detected on CE-MRA) were not significantly smaller than the rest of the

lesions and two of them were actually above 1 cm in maximum diameter. This supports the hypothesis that heterogeneity of the nidus has an important role on detectability of AVMs on CE-MRA -and almost certainly other MRA sequences too. Our results and previous studies demonstrate that CE-MRA is useful for characterisation of residual AVMs and it is more reliable when a residual AVM is visualized (good negative predictive value and high sensitivity). This appears to complement TOF which lacks temporal resolution, and is therefore inadequate for characterisation of residual AVMs, but can more reliable confirm obliteration (very good positive predictive value and high specificity) (Buis et al, 2012; Lee et al, 2015). This again supports the combined use of more than one MRA sequence to detect and characterise residual AVMs.

In our study, the arrival of contrast agent was not detected by CE-MRA in an important number of cases (5) due to mistiming of the gadolinium injection with respect to the dynamic acquisition. Also, in a few cases the first dynamic phase showing arrival of gadolinium happened to show the bolus just before it reached the AVM nidus so that 600 ms later when the next phase was acquired, the contrast had already filled the nidus and it had shunted into the venous side with the arterial phase of the nidus not being depicted on its own. These issues demonstrate that CE-MRA on its own cannot consistently provide all the dynamic information required for complete characterisation of AVMs and an additional dynamic MRA sequence, such as ASL-MRA, is required if results comparable to DSA are to be obtained.

There are to date no studies using ASL-MRA for confirmation of obliteration after radiosurgery. A number of studies have used ASL-MRA and ASL perfusion for assessment of AVMs with promising results but its value compared to DSA is still to be fully established (Fujima et al, 2016; Iryo et al, 2016; Yu et al, 2012). ASL-MRA uses the same principles of ASL perfusion to acquire images of the vasculature. The arterial blood water is magnetically labelled with a radiofrequency pulse proximal to the brain and it is used as an intrinsic contrast agent and flow tracer (Petersen et al, 2014). This is achieved by inverting the longitudinal magnetization of arterial water spins which changes the contrast

properties of inflowing blood with respect to the surrounding tissue (Golay et al, 2005). The subtraction of an image with inverted blood spins (label) and without inversion (control) results in images of the inflowing blood only (Lindner et al, 2015). Under normal conditions, most labelled water is extracted at the capillary level into the tissue, giving rise to the parenchymal perfusion signal intensity for which ASL is better known (Petersen et al, 2006; Xu et al, 2010). The same principle, with an early acquisition -before the tagged water leaves the vasculature- is applied to obtain angiographic images with near zero background and inflow dynamics similar to DSA (Suzuki et al, 2017). The T1 recovery of labelled spins is shorter than capillary transit time and for this reason signal intensity is not normally seen within intracranial veins in ASL angiography (Kukuk et al, 2010). AVMs, however, lack a capillary bed for water extraction to take place, and the labelled spins are shunted into the venous circulation with minimal transit time, giving rise to a high signal intensity in the AVM draining veins on ASL (Jang et al, 2014). This makes of ASL-MRA an appealing technique for confirmation of obliteration because -by definition- any depicted venous signal is the result of AV shunting, which is an unequivocal and defining element of AVMs (Figure 6.6).

In our study ASL-MRA showed the AVM shunt or nidus in 89% of the cases with a residual AVM. It proved critical to the assessment of obliteration in two cases where CE-MRA failed to demonstrate the residual lesion (Figure 6.3) and provided important information on nidus size and number of feeding arteries. Fujima et al compared ASL-MRA with TOF and DSA of 12 AVM patients and also concluded that ASL-MRA was useful for the detection of feeding arteries and characterisation of the nidus structure (Fujima et al, 2016). ASL-MRA has a great potential in terms of temporal resolution and acquisitions as fast as less than 100 ms per frame have been described (Lindner et al, 2015). We used a temporal resolution of 200 ms per frame, which is very close to the maximum resolution used in DSA (133 ms). We found that at this resolution the filling of the nidus can be optimally depicted, with unequivocal identification of the shunt and feeding arteries (Figure 6.6). Nonetheless, as other individual MRA sequences, ASL-MRA is by itself unable to capture all the possible scenarios of size, flow and

velocity to reliably detect residual AVMs. This is evidenced by the occurrence of false positives in which ASL-MRA fails to show the residual nidus (Figure 6.4g). If used on its own, ASL-MRA would then overestimated response rate. Early studies using ASL-MRA on AVM patients have already observed that despite offering hemodynamic information with very good temporal resolution (50 – 100 ms) it is better used as a complement to existing angiography methods (Yu et al, 2012). Nonetheless, ASL-MRA is a rapidly evolving technique. It has been shown to be suitable for imaging of selective vascular territories (Dai et al, 2010; Hendrikse et al, 2004; Robson et al, 2010) and it is being applied to several cerebrovascular diseases (Jensen-Kondering et al, 2015). Furthermore, the timing of dynamic acquisition in ASL-MRA can be personalised for the individual characteristics of lesion of interest. This can be achieved by using a short ASL vascular survey to characterise AVM filling velocity so that time resolution in the final acquisition is tailored according to the flow patterns in each individual case (Rojas-Villabona et al, 2017).

The main limitation of our study is the relatively small sample size. The assessment of a larger number of patients could have improved the study power and external validity of the results. Further optimisation of HD-TOF can be achieved by acquiring it after contrast injection (Bosmans et al, 1995). Gadolinium based contrast agents reduce the T_1 of blood which enhances blood magnetisation recovery and improves the contrast between flowing blood and background tissues in this inherently T_1 weighted acquisition (Yang et al, 2002). This was not part of our scanning protocol but it should be considered in future applications of triple-MRA. There is also a great potential for improvement of triple-MRA by post-processing the individual datasets to generate a single product that incorporates the information provided by all three sequences. This ranges from simple co-registration and superposition of the dynamic sequences on HD-TOF to complex algorithms that look at signal in each sequence and weigh it or model it to correct for flow artefacts and compensate for the reduced spatial resolution of the dynamic sequences (McGee et al, 2006). This is still to be accomplished and developers should aim for more sophisticated 4D visualisation maps which enhance the visual experience and facilitate interpretation. In our

study, the aim was to demonstrate the principle that using three MRA sequences in combination is as good as DSA for confirmation of obliteration. Therefore, extended image post-processing which could have become a confounding factor was avoided.

Finally, it is important to observe that the development of GKR as a treatment for brain AVMs was historically accomplished using DSA and radiosurgery practitioners still rely on post-treatment DSAs to assess obliteration and to advise patients on their cure or need for further treatment. The radiosurgical community have, therefore, a very high level of confidence on DSA as the reference standard method for confirmation of obliteration. This has contributed to the limited and hesitant use of MRA as an alternative to DSA in radiosurgery. For that reason, we asked the observers how confident they were of their assessment of obliteration both on triple-MRA and DSA. Surprisingly, there was no difference on the level of confidence reported when making assessment on triple-MRA compared to DSA and this is an encouraging finding which should help promote the use of less invasive imaging methods for AVM patients.

6.6 Conclusions

Triple-MRA consistently demonstrated/ruled out residual AVMs in patients who had undergone GKR for brain AVMs compared to DSA. The combination of three MRA sequences provides optimal sensitivity and specificity for confirmation of obliteration following GKR and it can also be reliably used for characterisation of residual AVMs after radiosurgery.

7. Conclusions and future work

The work presented in this dissertation is the response to a series of technical and clinical challenges encountered during the first four years of operations in the Gamma Knife Centre at Queen Square. These challenges, which are common to most contemporary Gamma Knife centres, were prospectively addressed and practical solutions were developed for the questions they posed.

The study in **chapter 3** demonstrated that inhomogeneity correction with the convolution algorithm results in a considerable but consistent dose shift compared to the TMR 10 algorithm traditionally used for GKR. No significant difference in relative dose distribution was noted and it was concluded that a reduction of the prescription dose is necessary to obtain the same absolute dosimetric effect with the convolution algorithm. This specific recommendation is of good practical value for radiosurgery practitioners because it enables informed selection of the dosimetry algorithm for treatment. The clinical use of the convolution algorithm has not yet been reported on peer-reviewed publications and future research work should result in the delivery of convolution-planned GKR treatments. We have provided appropriate guidance on dose adjustments that are required if this is to be done. We have also recommended that special attention be given to cases with major CT artefacts around the target, where the convolution algorithm may not optimally simulate dose distributions. This is important for case selection in future implementation phases.

The stability of the Leksell frame G in GKR was reported in **chapter 4**. A comprehensive study design involving repeated measurements of landmarks by

two observers was developed to exploit imaging data that was primarily acquired for the convolution algorithm study. It is likely that this is the first time a group of 40 non-selected patients underwent stereotactic imaging at both the beginning and the end of a GKR procedure and, therefore, it was important to assess the stability of the frame in this group of patients. The study provided reliable and realistic evidence of submillimetre stability of the stereotactic frame throughout the treatment procedure which is important for evaluation and development of new frameless radiosurgery systems. The stability of patient fixation in GKR has recently gained importance with the introduction of the Leksell Gamma Knife Icon (Elekta AB), which enables frameless radiosurgery with the Gamma Knife by using a new frameless Patient Positioning System (PPS) along with a Cone-Beam CT (CBCT) system and an Intra Fraction Motion Management (IFMM) system (Zeverino et al, 2017). The clinical accuracy of the new Icon Gamma Knife needs to be independently assessed and the data provided by this study will be a useful reference for comparison.

The combination of multiple MRA sequences as triple-MRA is an innovative strategy which was developed to reduce the invasiveness of GKR of brain AVMs by optimising the treatment planning method, traditionally based on DSA (**Chapter 5**). The technical feasibility of using triple-MRA, instead of DSA, for visualisation and delineation of brain AVMs for GKR targeting has been demonstrated. Target volumes obtained using triple-MRA are on average 10% smaller than AVM targets obtained with the standard DSA planning method and this can potentially reduce the risk of AREs. The discrepancies between triple-MRA and DSA volumes were less than the inter-observer variability observed when an AVM target is delineated by different radiosurgical teams. The treatment planning method described here has laid the way for changing clinical practice in favour of the less invasive approach. Two opportunities are potentially available for further clinical implementation of this research work. First, a randomised clinical trial to assess blindly whether planning of GKR using triple-MRA instead of DSA affects treatment outcomes, i.e., obliteration rates and ARE. Second, a staged implementation of the new planning method by continuing to trial it initially on selected low risk cases (small, compact and non-eloquent AVMs) and,

subject to results, more complex cases at a later stage. The second option may be more convenient because it provides further insight into the technical suitability of triple-MRA for radiosurgery planning and gives more opportunity for continued development and optimisation. Either way, future phases of clinical implementation should include thorough and long-term follow-up of patients treated with GKR using triple-MRA only; this will help to ascertain the impact of the planning method on clinical outcomes.

The same principle of less invasive AVM imaging by combining several MRA sequences was used at the post-GKR stage, when a DSA is routinely performed to confirm AVM obliteration (**chapter 6**). Triple-MRA was found consistently to confirm or rule out residual AVMs in patients who have undergone GKR for brain AVMs, compared to DSA. Triple-MRA provides optimal sensitivity and specificity for confirmation of obliteration following GKR and it can also be reliably used for characterisation of residual AVMs after radiosurgery. The widespread use of triple-MRA as a first line for the assessment of obliteration after GKR (instead of DSA) can positively impact radiosurgery practice by avoiding unnecessary DSA examinations for patients with cured AVMs but also through rationalising its use in patients with residual AVMs, who may need further treatments. The subjects studied in this project were all recruited and scanned at the University Hospital of Verona and future efforts should focus on extending this work to other radiosurgery centres, including Queen Square, to be able to study a larger group of patients. Optimisation of the imaging protocol on other scanning systems (i.e., Siemens and GE) will also allow for a larger population of patients to be studied.

GKR is a rapidly evolving and changing discipline and accelerated progress has historically been triggered by technical developments such as the introduction of CT and MR imaging in the 1980s or, more recently, the incorporation of frameless radiosurgery in the new Gamma Knife model. This context is necessary to understand the relevance of the research presented in this thesis but most importantly in helping to guide future research activities. This thesis has explored the dosimetric differences between the new convolution algorithm and the

standard TMR 10, demonstrated the stability of the rigid stereotactic Leksell frame and described the use of triple-MRA for planning and follow-up of GKR of brain AVMs. Future work should, therefore, aim to make GKR more accurate and less invasive by deploying the convolution algorithm, comparing new frameless systems with traditional rigid fixation and by replacing DSA with triple-MRA for treatment planning and assessment of obliteration following GKR of brain AVMs.

References

Aarup, L. R., Nahum, A. E., Zacharatou, C., Juhler-Nottrup, T., Knoos, T., Nystrom, H., Specht, L., Wieslander, E. & Korreman, S. S. (2009) The effect of different lung densities on the accuracy of various radiotherapy dose calculation methods: implications for tumour coverage. *Radiother Oncol*, 91(3), 405-14.

Al-Shahi, R., Fang, J. S., Lewis, S. C. & Warlow, C. P. (2002a) Prevalence of adults with brain arteriovenous malformations: a community based study in Scotland using capture-recapture analysis. *J Neurol Neurosurg Psychiatry*, 73(5), 547-51.

Al-Shahi, R., Pal, N., Lewis, S. C., Bhattacharya, J. J., Sellar, R. J., Warlow, C. P. & Group, A. O. A. S. (2002b) Observer agreement in the angiographic assessment of arteriovenous malformations of the brain. *Stroke*, 33(6), 1501-8.

Allsop, M. J., Twiddy, M., Grant, H., Czoski-Murray, C., Mon-Williams, M., Mushtaq, F., Phillips, N., Zakrzewska, J. M. & Pavitt, S. (2015) Diagnosis, medication, and surgical management for patients with trigeminal neuralgia: a qualitative study. *Acta Neurochir (Wien)*, 157(11), 1925-33.

Alsop, D. C. & Detre, J. A. (1998) Multisection cerebral blood flow MR imaging with continuous arterial spin labeling. *Radiology*, 208(2), 410-6.

Amponsah, K., Ellis, T. L., Chan, M. D., Lovato, J. F., Bourland, J. D., deGuzman, A. F., Ekstrand, K. E., Munley, M. T., McMullen, K. P., Shaw, E. G. & Tatter, S. B. (2012) Retrospective analysis of imaging techniques for treatment

planning and monitoring of obliteration for gamma knife treatment of cerebral arteriovenous malformation. *Neurosurgery*, 71(4), 893-9.

Andrews, D. W., Scott, C. B., Sperduto, P. W., Flanders, A. E., Gaspar, L. E., Schell, M. C., Werner-Wasik, M., Demas, W., Ryu, J., Bahary, J. P., Souhami, L., Rotman, M., Mehta, M. P. & Curran, W. J., Jr. (2004) Whole brain radiation therapy with or without stereotactic radiosurgery boost for patients with one to three brain metastases: phase III results of the RTOG 9508 randomised trial. *Lancet*, 363(9422), 1665-72.

Aoyama, H., Shirato, H., Tago, M., Nakagawa, K., Toyoda, T., Hatano, K., Kenjyo, M., Oya, N., Hirota, S., Shioura, H., Kunieda, E., Inomata, T., Hayakawa, K., Katoh, N. & Kobashi, G. (2006) Stereotactic radiosurgery plus whole-brain radiation therapy vs stereotactic radiosurgery alone for treatment of brain metastases: a randomized controlled trial. *JAMA*, 295(21), 2483-91.

Aoyama, H., Tago, M., Kato, N., Toyoda, T., Kenjyo, M., Hirota, S., Shioura, H., Inomata, T., Kunieda, E., Hayakawa, K., Nakagawa, K., Kobashi, G. & Shirato, H. (2007) Neurocognitive function of patients with brain metastasis who received either whole brain radiotherapy plus stereotactic radiosurgery or radiosurgery alone. *Int J Radiat Oncol Biol Phys*, 68(5), 1388-95.

Arthurs, B. J., Fairbanks, R. K., Demakas, J. J., Lamoreaux, W. T., Giddings, N. A., Mackay, A. R., Cooke, B. S., Elaimy, A. L. & Lee, C. M. (2011) A review of treatment modalities for vestibular schwannoma. *Neurosurg Rev*, 34(3), 265-77; discussion 277-9.

Attia, A., Tatter, S. B., Weller, M., Marshall, K., Lovato, J. F., Bourland, J. D., Ellis, T. L., McMullen, K. P., Shaw, E. G. & Chan, M. D. (2012) CT-only planning for Gamma Knife radiosurgery in the treatment of trigeminal neuralgia: methodology and outcomes from a single institution. *J Med Imaging Radiat Oncol*, 56(4), 490-4.

Bambakidis, N. C., Cockroft, K. M., Hirsch, J. A., Connolly, E. S., Amin-Hanjani, S., Meyers, P. M. & Friedlander, R. M. (2014) The case against a randomized trial

of unruptured brain arteriovenous malformations: misinterpretation of a flawed study. *Stroke*, 45(9), 2808-10.

Banfill, K. E., Bownes, P. J., St Clair, S. E., Loughrey, C. & Hatfield, P. (2012) Stereotactic radiosurgery for the treatment of brain metastases: impact of cerebral disease burden on survival. *Br J Neurosurg*, 26(5), 674-8.

Bari, M. E., Forster, D. M., Kemeny, A. A., Walton, L., Hardy, D. & Anderson, J. R. (2002) Malignancy in a vestibular schwannoma. Report of a case with central neurofibromatosis, treated by both stereotactic radiosurgery and surgical excision, with a review of the literature. *Br J Neurosurg*, 16(3), 284-9.

Barnett, G. H., Linskey, M. E., Adler, J. R., Cozzens, J. W., Friedman, W. A., Heilbrun, M. P., Lunsford, L. D., Schulder, M., Sloan, A. E., Surgeons, A. A. o. N. & Force, C. o. N. S. W. C. S. R. T. (2007) Stereotactic radiosurgery--an organized neurosurgery-sanctioned definition. *J Neurosurg*, 106(1), 1-5.

Baschnagel, A. M., Cartier, J. L., Dreyer, J., Chen, P. Y., Pieper, D. R., Olson, R. E., Krauss, D. J., Maitz, A. H. & Grills, I. S. (2014) Trigeminal neuralgia pain relief after gamma knife stereotactic radiosurgery. *Clin Neurol Neurosurg*, 117, 107-11.

Bednarz, G., Downes, B., Werner-Wasik, M. & Rosenwasser, R. H. (2000) Combining stereotactic angiography and 3D time-of-flight magnetic resonance angiography in treatment planning for arteriovenous malformation radiosurgery. *Int J Radiat Oncol Biol Phys*, 46(5), 1149-54.

Bendszus, M., Koltzenburg, M., Burger, R., Warmuth-Metz, M., Hofmann, E. & Solymosi, L. (1999) Silent embolism in diagnostic cerebral angiography and neurointerventional procedures: a prospective study. *Lancet*, 354(9190), 1594-7.

Bentzen, S. M. (2006) Preventing or reducing late side effects of radiation therapy: radiobiology meets molecular pathology. *Nat Rev Cancer*, 6(9), 702-13.

Berkowitz, O., Kondziolka, D., Bissonette, D., Niranjan, A., Kano, H. & Lunsford, L. D. (2013) The evolution of a clinical registry during 25 years of

experience with Gamma Knife radiosurgery in Pittsburgh. *Neurosurg Focus*, 34(1), E4.

Bieri, O. & Scheffler, K. (2005) Flow compensation in balanced SSFP sequences. *Magn Reson Med*, 54(4), 901-7.

Bosmans, H., Marchal, G., Lukito, G., Yicheng, N., Wilms, G., Laub, G. & Baert, A. L. (1995) Time-of-flight MR angiography of the brain: comparison of acquisition techniques in healthy volunteers. *AJR Am J Roentgenol*, 164(1), 161-7.

Brainlab (2011) Clinical White Paper: iPLAN automatic image fusion.

Brainlab (2017) White paper: cranial distortion correction.

Breneman, J. C., Warnick, R. E., Albright, R. E., Kukiatinant, N., Shaw, J., Armin, D. & Tew, J. (1997) Stereotactic radiosurgery for the treatment of brain metastases. Results of a single institution series. *Cancer*, 79(3), 551-7.

Brenner, D. J. & Hall, E. J. (2007) Computed tomography--an increasing source of radiation exposure. *N Engl J Med*, 357(22), 2277-84.

Buis, D. R., Bot, J. C., Barkhof, F., Knol, D. L., Lagerwaard, F. J., Slotman, B. J., Vandertop, W. P. & van den Berg, R. (2012) The predictive value of 3D time-of-flight MR angiography in assessment of brain arteriovenous malformation obliteration after radiosurgery. *AJNR Am J Neuroradiol*, 33(2), 232-8.

Buis, D. R., Lagerwaard, F. J., Barkhof, F., Dirven, C. M., Lycklama, G. J., Meijer, O. W., van den Berg, R., Langendijk, H. A., Slotman, B. J. & Vandertop, W. P. (2005) Stereotactic radiosurgery for brain AVMs: role of interobserver variation in target definition on digital subtraction angiography. *Int J Radiat Oncol Biol Phys*, 62(1), 246-52.

Buis, D. R., Lagerwaard, F. J., Dirven, C. M., Barkhof, F., Knol, D. L., van den Berg, R., Slotman, B. J. & Vandertop, W. P. (2007) Delineation of brain AVMs

on MR-Angiography for the purpose of stereotactic radiosurgery. *Int J Radiat Oncol Biol Phys*, 67(1), 308-16.

Cernica, G., Wang, Z., Malhotra, H., de Boer, S. & Podgorsak, M. B. (2006) Investigation of gamma knife image registration errors resulting from misalignment between the patient and the imaging axis. *Med Phys*, 33(4), 941-3.

Chang, S. D., Lee, E., Sakamoto, G. T., Brown, N. P. & Adler, J. R., Jr. (2000) Stereotactic radiosurgery in patients with multiple brain metastases. *Neurosurg Focus*, 9(2), e3.

Chang, W., Wu, Y., Johnson, K., Loecher, M., Wieben, O., Edjlali, M., Oppenheim, C., Roca, P., Hald, J., Aagaard-Kienitz, B., Niemann, D., Mistretta, C. & Turski, P. (2015) Fast contrast-enhanced 4D MRA and 4D flow MRI using constrained reconstruction (HYPRFlow): potential applications for brain arteriovenous malformations. *AJNR Am J Neuroradiol*, 36(6), 1049-55.

Chng, S. M., Petersen, E. T., Zimine, I., Sitoh, Y. Y., Lim, C. C. & Golay, X. (2008) Territorial arterial spin labeling in the assessment of collateral circulation: comparison with digital subtraction angiography. *Stroke*, 39(12), 3248-54.

Chung, W. Y., Pan, D. H., Lee, C. C., Wu, H. M., Liu, K. D., Yen, Y. S., Guo, W. Y., Shiau, C. Y. & Shih, Y. H. (2010) Large vestibular schwannomas treated by Gamma Knife surgery: long-term outcomes. *J Neurosurg*, 113 Suppl, 112-21.

Cohen-Inbar, O., Lee, C. C., Xu, Z., Schlesinger, D. & Sheehan, J. P. (2015) A quantitative analysis of adverse radiation effects following Gamma Knife radiosurgery for arteriovenous malformations. *J Neurosurg*, 123(4), 945-53.

Colombo, F., Cavedon, C., Francescon, P., Casentini, L., Fornezza, U., Castellan, L., Causin, F. & Perini, S. (2003) Three-dimensional angiography for radiosurgical treatment planning for arteriovenous malformations. *J Neurosurg*, 98(3), 536-43.

Condra, K. S., Buatti, J. M., Mendenhall, W. M., Friedman, W. A., Marcus, R. B. & Rhoton, A. L. (1997) Benign meningiomas: primary treatment selection affects survival. *Int J Radiat Oncol Biol Phys*, 39(2), 427-36.

Constantinou, C., Harrington, J. C. & DeWerd, L. A. (1992) An electron density calibration phantom for CT-based treatment planning computers. *Med Phys*, 19(2), 325-7.

Counsell, C. E., Collie, D. A. & Grant, R. (1996) Incidence of intracranial tumours in the Lothian region of Scotland, 1989-90. *J Neurol Neurosurg Psychiatry*, 61(2), 143-50.

da Costa, L., Wallace, M. C., Ter Brugge, K. G., O'Kelly, C., Willinsky, R. A. & Tymianski, M. (2009) The natural history and predictive features of hemorrhage from brain arteriovenous malformations. *Stroke*, 40(1), 100-5.

Da Silva, A. N., Nagayama, K., Schlesinger, D. J. & Sheehan, J. P. (2009) Gamma Knife surgery for brain metastases from gastrointestinal cancer. *J Neurosurg*, 111(3), 423-30.

Dai, W., Robson, P. M., Shankaranarayanan, A. & Alsop, D. C. (2010) Modified pulsed continuous arterial spin labeling for labeling of a single artery. *Magn Reson Med*, 64(4), 975-82.

Dauer, L. T., Brooks, A. L., Hoel, D. G., Morgan, W. F., Stram, D. & Tran, P. (2010) Review and evaluation of updated research on the health effects associated with low-dose ionising radiation. *Radiat Prot Dosimetry*, 140(2), 103-36.

Dawkins, A. A., Evans, A. L., Wattam, J., Romanowski, C. A., Connolly, D. J., Hodgson, T. J. & Coley, S. C. (2007) Complications of cerebral angiography: a prospective analysis of 2,924 consecutive procedures. *Neuroradiology*, 49(9), 753-9.

Dhople, A. A., Adams, J. R., Maggio, W. W., Naqvi, S. A., Regine, W. F. & Kwok, Y. (2009) Long-term outcomes of Gamma Knife radiosurgery for classic

trigeminal neuralgia: implications of treatment and critical review of the literature. Clinical article. *J Neurosurg*, 111(2), 351-8.

Duan, Y. L., Li, J. B., Zhang, Y. J., Wang, W., Li, F. X., Sun, X. R., Guo, Y. L. & Shang, D. P. (2014) Comparison of primary target volumes delineated on four-dimensional CT and 18 F-FDG PET/CT of non-small-cell lung cancer. *Radiat Oncol*, 9, 182.

Eichler, A. F. & Loeffler, J. S. (2007) Multidisciplinary management of brain metastases. *Oncologist*, 12(7), 884-98.

Elekta (2011a) A new TMR algorithm in Leksell GammaPlan. Article No 1021357. July 20122. www.elekta.com.

Elekta (2011b) The Convolution algorithm in Leksell GammaPlan 10. Article No 018881-02. Sept 2011. www.elekta.com.

Fifi, J. T., Meyers, P. M., Lavine, S. D., Cox, V., Silverberg, L., Mangla, S. & Pile-Spellman, J. (2009) Complications of modern diagnostic cerebral angiography in an academic medical center. *J Vasc Interv Radiol*, 20(4), 442-7.

Flickinger, J. C., Kondziolka, D., Lunsford, L. D., Kassam, A., Phuong, L. K., Liscak, R. & Pollock, B. (2000) Development of a model to predict permanent symptomatic postradiosurgery injury for arteriovenous malformation patients. Arteriovenous Malformation Radiosurgery Study Group. *Int J Radiat Oncol Biol Phys*, 46(5), 1143-8.

Fujima, N., Osanai, T., Shimizu, Y., Yoshida, A., Harada, T., Nakayama, N., Kudo, K., Houkin, K. & Shirato, H. (2016) Utility of noncontrast-enhanced time-resolved four-dimensional MR angiography with a vessel-selective technique for intracranial arteriovenous malformations. *J Magn Reson Imaging*, 44(4), 834-45.

Giesel, F. L., Essig, M., Zabel-Du-Bois, A., Bock, M., von Tengg-Kobligk, H., Afshar-Omarei, A., Debus, J., Kauczor, H. U. & Krix, M. (2010) High-contrast computed tomographic angiography better detects residual intracranial

arteriovenous malformations in long-term follow-up after radiotherapy than 1.5-Tesla time-of-flight magnetic resonance angiography. *Acta Radiol*, 51(1), 64-70.

Golay, X., Petersen, E. T. & Hui, F. (2005) Pulsed star labeling of arterial regions (PULSAR): a robust regional perfusion technique for high field imaging. *Magn Reson Med*, 53(1), 15-21.

Guo, W. Y., Nordell, B., Karlsson, B., Söderman, M., Lindqvist, M., Ericson, K., Franck, A., Lax, I. & Lindquist, C. (1993) Target delineation in radiosurgery for cerebral arteriovenous malformations. Assessment of the value of stereotaxic MR imaging and MR angiography. *Acta Radiol*, 34(5), 457-63.

Hadizadeh, D. R., Gieseke, J., Beck, G., Geerts, L., Kukuk, G. M., Boström, A., Urbach, H., Schild, H. H. & Willinek, W. A. (2011) View-sharing in keyhole imaging: Partially compressed central k-space acquisition in time-resolved MRA at 3.0 T. *Eur J Radiol*, 80(2), 400-6.

Hadizadeh, D. R., von Falkenhausen, M., Gieseke, J., Meyer, B., Urbach, H., Hoogeveen, R., Schild, H. H. & Willinek, W. A. (2008) Cerebral arteriovenous malformation: Spetzler-Martin classification at subsecond-temporal-resolution four-dimensional MR angiography compared with that at DSA. *Radiology*, 246(1), 205-13.

Haider, C. R., Borisch, E. A., Glockner, J. F., Mostardi, P. M., Rossman, P. J., Young, P. M. & Riederer, S. J. (2010) Max CAPR: high-resolution 3D contrast-enhanced MR angiography with acquisition times under 5 seconds. *Magn Reson Med*, 64(4), 1171-81.

Hamm, K. D., Klisch, J., Surber, G., Kleinert, G., Eger, C. & Aschenbach, R. (2008) Special aspects of diagnostic imaging for radiosurgery of arteriovenous malformations. *Neurosurgery*, 62(5 Suppl), A44-52; discussion A52.

Hanssens, P., Karlsson, B., Yeo, T. T., Chou, N. & Beute, G. (2011) Detection of brain micrometastases by high-resolution stereotactic magnetic resonance imaging

and its impact on the timing of and risk for distant recurrences. *J Neurosurg*, 115(3), 499-504.

Harrison, G., Kano, H., Lunsford, L. D., Flickinger, J. C. & Kondziolka, D. (2016) Quantitative tumor volumetric responses after Gamma Knife radiosurgery for meningiomas. *J Neurosurg*, 124(1), 146-54.

Heck, B., Jess-Hempen, A., Kreiner, H. J., Schopgens, H. & Mack, A. (2007) Accuracy and stability of positioning in radiosurgery: long-term results of the Gamma Knife system. *Med Phys*, 34(4), 1487-95.

Helle, M., Norris, D. G., Rufer, S., Alfke, K., Jansen, O. & van Osch, M. J. (2010) Superselective pseudocontinuous arterial spin labeling. *Magn Reson Med*, 64(3), 777-86.

Helle, M., Rüfer, S., van Osch, M. J., Nabavi, A., Alfke, K., Norris, D. G. & Jansen, O. (2013) Superselective arterial spin labeling applied for flow territory mapping in various cerebrovascular diseases. *J Magn Reson Imaging*, 38(2), 496-503.

Hendrikse, J., van der Grond, J., Lu, H., van Zijl, P. C. & Golay, X. (2004) Flow territory mapping of the cerebral arteries with regional perfusion MRI. *Stroke*, 35(4), 882-7.

Hernesniemi, J. A., Dashti, R., Juvela, S., Vaart, K., Niemela, M. & Laakso, A. (2008) Natural history of brain arteriovenous malformations: a long-term follow-up study of risk of hemorrhage in 238 patients. *Neurosurgery*, 63(5), 823-9; discussion 829-31.

Hounsfield, G. N. (1976) Historical notes on computerized axial tomography. *J Can Assoc Radiol*, 27(3), 135-42.

Huang, Y. J., Hsu, S. W., Lee, T. F., Ho, J. T. & Chen, W. F. (2017) Consistency between Targets Delineated by Angiography, Computed Tomography, and Magnetic Resonance Imaging in Stereotactic Radiosurgery for Arteriovenous Malformation. *Stereotact Funct Neurosurg*, 95(4), 236-242.

IASP (1986) Classification of chronic pain. Descriptions of chronic pain syndromes and definitions of pain terms. Prepared by the International Association for the Study of Pain, Subcommittee on Taxonomy. *Pain Suppl*, 3, S1-226.

Iryo, Y., Hirai, T., Nakamura, M., Kawano, T., Kaku, Y., Ohmori, Y., Kai, Y., Azuma, M., Nishimura, S., Shigematsu, Y., Kitajima, M. & Yamashita, Y. (2016) Evaluation of Intracranial Arteriovenous Malformations With Four-Dimensional Arterial-Spin Labeling-Based 3-T Magnetic Resonance Angiography. *J Comput Assist Tomogr*, 40(2), 290-6.

Jaccard, P. (1912) The distribution of the flora in the alpine zone. *New Phytologist*, 11(2), 37-50.

Jang, J., Schmitt, P., Kim, B. Y., Choi, H. S., Jung, S. L., Ahn, K. J., Kim, I., Paek, M. & Kim, B. S. (2014) Non-contrast-enhanced 4D MR angiography with STAR spin labeling and variable flip angle sampling: a feasibility study for the assessment of Dural Arteriovenous Fistula. *Neuroradiology*, 56(4), 305-14.

Jensen-Kondering, U., Lindner, T., van Osch, M. J., Rohr, A., Jansen, O. & Helle, M. (2015) Superselective pseudo-continuous arterial spin labeling angiography. *Eur J Radiol*, 84(9), 1758-67.

Johnson, C. P., Haider, C. R., Borisch, E. A., Glockner, J. F. & Riederer, S. J. (2010) Time-resolved bolus-chase MR angiography with real-time triggering of table motion. *Magn Reson Med*, 64(3), 629-37.

Jones, A. P. (1993) Diagnostic imaging as a measuring device for stereotactic neurosurgery. *Physiol Meas*, 14(2), 91-112.

Kang, C. K., Park, C. W., Han, J. Y., Kim, S. H., Park, C. A., Kim, K. N., Hong, S. M., Kim, Y. B., Lee, K. H. & Cho, Z. H. (2009) Imaging and analysis of lenticulostriate arteries using 7.0-Tesla magnetic resonance angiography. *Magn Reson Med*, 61(1), 136-44.

Kang, J., Huang, J., Gailloud, P., Rigamonti, D., Lim, M., Bernard, V., Ehtiati, T. & Ford, E. C. (2014) Planning evaluation of C-arm cone beam CT angiography for target delineation in stereotactic radiation surgery of brain arteriovenous malformations. *Int J Radiat Oncol Biol Phys*, 90(2), 430-7.

Kano, H., Flickinger, J. C., Tonetti, D., Hsu, A., Yang, H. C., Flannery, T. J., Niranjan, A. & Lunsford, L. D. (2017) Estimating the Risks of Adverse Radiation Effects After Gamma Knife Radiosurgery for Arteriovenous Malformations. *Stroke*, 48(1), 84-90.

Kano, H., Kondziolka, D., Flickinger, J. C., Park, K. J., Iyer, A., Yang, H. C., Liu, X., Monaco, E. A., 3rd, Niranjan, A. & Lunsford, L. D. (2012a) Stereotactic radiosurgery for arteriovenous malformations after embolization: a case-control study. *J Neurosurg*, 117(2), 265-75.

Kano, H., Kondziolka, D., Flickinger, J. C., Park, K. J., Iyer, A., Yang, H. C., Liu, X., Monaco, E. A., 3rd, Niranjan, A. & Lunsford, L. D. (2013) Stereotactic radiosurgery after embolization for arteriovenous malformations. *Prog Neurol Surg*, 27, 89-96.

Kano, H., Kondziolka, D., Flickinger, J. C., Yang, H. C., Flannery, T. J., Awan, N. R., Niranjan, A., Novotny, J., Jr. & Lunsford, L. D. (2012b) Stereotactic radiosurgery for arteriovenous malformations, Part 3: outcome predictors and risks after repeat radiosurgery. *J Neurosurg*, 116(1), 21-32.

Karlsson, B., Hanssens, P., Wolff, R., Soderman, M., Lindquist, C. & Beute, G. (2009) Thirty years' experience with Gamma Knife surgery for metastases to the brain. *J Neurosurg*, 111(3), 449-57.

Karlsson, B., Kalend, A. & Martinez, R. (2011) Frame stability and anatomical QA in radiosurgery. *Acta Neurochir (Wien)*, 153(11), 2265-70.

Karonen, J. O., Liu, Y., Vanninen, R. L., Ostergaard, L., Kaarina Partanen, P. L., Vainio, P. A., Vanninen, E. J., Nuutinen, J., Roivainen, R., Soimakallio, S., Kuikka, J. T. & Aronen, H. J. (2000) Combined perfusion- and diffusion-

weighted MR imaging in acute ischemic stroke during the 1st week: a longitudinal study. *Radiology*, 217(3), 886-94.

Kaufmann, T. J., Huston, J., 3rd, Mandrekar, J. N., Schleck, C. D., Thielen, K. R. & Kallmes, D. F. (2007) Complications of diagnostic cerebral angiography: evaluation of 19,826 consecutive patients. *Radiology*, 243(3), 812-9.

Kemeny, A. A., Dias, P. S. & Forster, D. M. (1989) Results of stereotactic radiosurgery of arteriovenous malformations: an analysis of 52 cases. *J Neurol Neurosurg Psychiatry*, 52(5), 554-8.

Kennan, R. P. & Jäger, H. R. (2003) T2-and T2*-w DCE-MRI: blood perfusion and volume estimation using bolus tracking. *Quantitative MRI of the Brain. Measuring changes caused by disease*, 365-412.

Khalsa, S. S., Chinn, M., Krucoff, M. & Sherman, J. H. (2013) The role of stereotactic radiosurgery for multiple brain metastases in stable systemic disease: a review of the literature. *Acta Neurochir (Wien)*, 155(7), 1321-7; discussion 1327-8.

Khandanpour, N., Griffiths, P., Warren, D. & Hoggard, N. (2013) Prospective comparison of late 3T MRI with conventional angiography in evaluating the patency of cerebral arteriovenous malformations treated with stereotactic radiosurgery. *Neuroradiology*, 55(6), 683-7.

Koga, T., Shin, M. & Saito, N. (2010) Role of gamma knife radiosurgery in neurosurgery: past and future perspectives. *Neurol Med Chir (Tokyo)*, 50(9), 737-48.

Kohler, B. A., Ward, E., McCarthy, B. J., Schymura, M. J., Ries, L. A., Eheman, C., Jemal, A., Anderson, R. N., Ajani, U. A. & Edwards, B. K. (2011) Annual report to the nation on the status of cancer, 1975-2007, featuring tumors of the brain and other nervous system. *J Natl Cancer Inst*, 103(9), 714-36.

Koltz, M. T., Polifka, A. J., Saltos, A., Slawson, R. G., Kwok, Y., Aldrich, E. F. & Simard, J. M. (2013) Long-term outcome of Gamma Knife stereotactic

radiosurgery for arteriovenous malformations graded by the Spetzler-Martin classification. *J Neurosurg*, 118(1), 74-83.

Kondziolka, D., Zorro, O., Lobato-Polo, J., Kano, H., Flannery, T. J., Flickinger, J. C. & Lunsford, L. D. (2010) Gamma Knife stereotactic radiosurgery for idiopathic trigeminal neuralgia. *J Neurosurg*, 112(4), 758-65.

Koos, W. T., Day, J. D., Matula, C. & Levy, D. I. (1998) Neurotopographic considerations in the microsurgical treatment of small acoustic neurinomas. *J Neurosurg*, 88(3), 506-12.

Kopeinigg, D. & Bammer, R. (2014) Time-resolved angiography using inflow subtraction (TRAILS). *Magn Reson Med*, 72(3), 669-78.

Kukuk, G. M., Hadizadeh, D. R., Bostrom, A., Gieseke, J., Bergener, J., Nelles, M., Murtz, P., Urbach, H., Schild, H. H. & Willinek, W. A. (2010) Cerebral arteriovenous malformations at 3.0 T: intraindividual comparative study of 4D-MRA in combination with selective arterial spin labeling and digital subtraction angiography. *Invest Radiol*, 45(3), 126-32.

Langley, R. E., Stephens, R. J., Nankivell, M., Pugh, C., Moore, B., Navani, N., Wilson, P., Faivre-Finn, C., Barton, R., Parmar, M. K. & Mulvenna, P. M. (2013) Interim data from the Medical Research Council QUARTZ Trial: does whole brain radiotherapy affect the survival and quality of life of patients with brain metastases from non-small cell lung cancer? *Clin Oncol (R Coll Radiol)*, 25(3), e23-30.

Larsson, B., Leksell, L., Rexed, B., Sourander, P., Mair, W. & Andersson, B. (1958) The high-energy proton beam as a neurosurgical tool. *Nature*, 182(4644), 1222-3.

Le, T. T., Fischbein, N. J., André, J. B., Wijman, C., Rosenberg, J. & Zaharchuk, G. (2012) Identification of venous signal on arterial spin labeling improves diagnosis of dural arteriovenous fistulas and small arteriovenous malformations. *AJNR Am J Neuroradiol*, 33(1), 61-8.

Lee, C. C., Reardon, M. A., Ball, B. Z., Chen, C. J., Yen, C. P., Xu, Z., Wintermark, M. & Sheehan, J. (2015) The predictive value of magnetic resonance imaging in evaluating intracranial arteriovenous malformation obliteration after stereotactic radiosurgery. *J Neurosurg*, 123(1), 136-44.

Leffers, A. M. & Wagner, A. (2000) Neurologic complications of cerebral angiography. A retrospective study of complication rate and patient risk factors. *Acta Radiol*, 41(3), 204-10.

Leksell Gamma Knife Society, L. (2016) *Leksell Gamma Knife annual treatment statistics.*

Leksell, L. (1951) The stereotaxic method and radiosurgery of the brain. *Acta Chir Scand*, 102(4), 316-9.

Leksell, L. (1968) Cerebral radiosurgery. I. Gammathalanotomy in two cases of intractable pain. *Acta Chir Scand*, 134(8), 585-95.

Leksell, L. (1971) Sterotaxic radiosurgery in trigeminal neuralgia. *Acta Chir Scand*, 137(4), 311-4.

Leksell, L. (1983) Stereotactic radiosurgery. *J Neurol Neurosurg Psychiatry*, 46(9), 797-803.

Leksell, L. & Backlund, E. O. (1978) [Radiosurgical capsulotomy--a closed surgical method for psychiatric surgery]. *Lakartidningen*, 75(7), 546-7.

Leksell, L., Herner, T., Leksell, D., Persson, B. & Lindquist, C. (1985a) Visualisation of stereotactic radiolesions by nuclear magnetic resonance. *J Neurol Neurosurg Psychiatry*, 48(1), 19-20.

Leksell, L. & Jernberg, B. (1980) Stereotaxis and tomography. A technical note. *Acta Neurochir (Wien)*, 52(1-2), 1-7.

Leksell, L., Leksell, D. & Schwebel, J. (1985b) Stereotaxis and nuclear magnetic resonance. *J Neurol Neurosurg Psychiatry*, 48(1), 14-8.

Leksell, L., Meyerson, B. A. & Forster, D. M. (1972) Radiosurgical thalamotomy for intractable pain. *Confin Neurol*, 34(1), 264.

Levrier, O., Manera, L., Regis, J., Farnarier, P., Ruefenacht, D. & Raybaut, C. (2001) [Advances in the contributions of imaging to stereotaxic localization of cerebral arteriovenous malformations for radiosurgery]. *Neurochirurgie*, 47(2-3 Pt 2), 201-11.

Lim, H. K., Choi, C. G., Kim, S. M., Kim, J. L., Lee, D. H., Kim, S. J. & Suh, D. C. (2012) Detection of residual brain arteriovenous malformations after radiosurgery: diagnostic accuracy of contrast-enhanced four-dimensional MR angiography at 3.0 T. *Br J Radiol*, 85(1016), 1064-9.

Lindner, T., Jensen-Kondering, U., van Osch, M. J., Jansen, O. & Helle, M. (2015) 3D time-resolved vessel-selective angiography based on pseudo-continuous arterial spin labeling. *Magn Reson Imaging*, 33(6), 840-6.

Lindquist, C. & Paddick, I. (2007) The Leksell Gamma Knife Perfexion and comparisons with its predecessors. *Neurosurgery*, 61(3 Suppl), 130-40; discussion 140-1.

Linskey, M. E., Andrews, D. W., Asher, A. L., Burri, S. H., Kondziolka, D., Robinson, P. D., Ammirati, M., Cobbs, C. S., Gaspar, L. E., Loeffler, J. S., McDermott, M., Mehta, M. P., Mikkelsen, T., Olson, J. J., Paleologos, N. A., Patchell, R. A., Ryken, T. C. & Kalkanis, S. N. (2010) The role of stereotactic radiosurgery in the management of patients with newly diagnosed brain metastases: a systematic review and evidence-based clinical practice guideline. *J Neurooncol*, 96(1), 45-68.

Lippitz, B., Lindquist, C., Paddick, I., Peterson, D., O'Neill, K. & Beaney, R. (2014) Stereotactic radiosurgery in the treatment of brain metastases: the current evidence. *Cancer Treat Rev*, 40(1), 48-59.

Lipski, S. M., Hayashi, M., Chernov, M., Levivier, M. & Okada, Y. (2015) Modern Gamma Knife radiosurgery of vestibular schwannomas: treatment

concept, volumetric tumor response, and functional results. *Neurosurg Rev*, 38(2), 309-18; discussion 318.

Lu, W., Olivera, G. H., Chen, M. L., Reckwerdt, P. J. & Mackie, T. R. (2005) Accurate convolution/superposition for multi-resolution dose calculation using cumulative tabulated kernels. *Phys Med Biol*, 50(4), 655-80.

Lunsford, L. D., Flickinger, J., Lindner, G. & Maitz, A. (1989) Stereotactic radiosurgery of the brain using the first United States 201 cobalt-60 source gamma knife. *Neurosurgery*, 24(2), 151-9.

Lunsford, L. D., Kondziolka, D., Flickinger, J. C., Bissonette, D. J., Jungreis, C. A., Maitz, A. H., Horton, J. A. & Coffey, R. J. (1991) Stereotactic radiosurgery for arteriovenous malformations of the brain. *J Neurosurg*, 75(4), 512-24.

Lunsford, L. D., Niranjan, A., Kano, H. & Kondziolka, D. (2013) The technical evolution of gamma knife radiosurgery for arteriovenous malformations. *Prog Neurol Surg*, 27, 22-34.

Lustig, M., Donoho, D. & Pauly, J. M. (2007) Sparse MRI: The application of compressed sensing for rapid MR imaging. *Magn Reson Med*, 58(6), 1182-95.

MacDonald, M. E. & Frayne, R. (2015) Cerebrovascular MRI: a review of state-of-the-art approaches, methods and techniques. *NMR Biomed*, 28(7), 767-91.

Machet, A., Portefaix, C., Kadziolka, K., Robin, G., Lanoix, O. & Pierot, L. (2012) Brain arteriovenous malformation diagnosis: value of time-resolved contrast-enhanced MR angiography at 3.0T compared to DSA. *Neuroradiology*, 54(10), 1099-108.

Maciunas, R. J., Galloway, R. L., Jr. & Latimer, J. W. (1994) The application accuracy of stereotactic frames. *Neurosurgery*, 35(4), 682-94; discussion 694-5.

Mack, A., Czempiel, H., Kreiner, H. J., Durr, G. & Wowra, B. (2002) Quality assurance in stereotactic space. A system test for verifying the accuracy of aim in radiosurgery. *Med Phys*, 29(4), 561-8.

Mack, A., Weltz, D., Scheib, S. G., Wowra, B., Bottcher, H. & Seifert, V. (2006) Development of a 3-D convolution/superposition algorithm for precise dose calculation in the skull. *Australas Phys Eng Sci Med*, 29(1), 1-12.

Mamalui-Hunter, M., Jiang, T., Rich, K. M., Derdeyn, C. P. & Drzymala, R. E. (2011) Effect of liquid embolic agents on Gamma Knife surgery dosimetry for arteriovenous malformations. Clinical article. *J Neurosurg*, 115(2), 364-70.

Mansouri, A., Guha, D., Klironomos, G., Larjani, S., Zadeh, G. & Kondziolka, D. (2015a) Stereotactic radiosurgery for intracranial meningiomas: current concepts and future perspectives. *Neurosurgery*, 76(4), 362-71.

Mansouri, A., Larjani, S., Klironomos, G., Laperriere, N., Cusimano, M., Gentili, F., Schwartz, M. & Zadeh, G. (2015b) Predictors of response to Gamma Knife radiosurgery for intracranial meningiomas. *J Neurosurg*, 123(5), 1294-300.

Massager, N., Abeloos, L., Devriendt, D., Op de Beeck, M. & Levivier, M. (2007) Clinical evaluation of targeting accuracy of gamma knife radiosurgery in trigeminal neuralgia. *Int J Radiat Oncol Biol Phys*, 69(5), 1514-20.

Massager, N., Nissim, O., Murata, N., Devriendt, D., Desmedt, F., Vanderlinden, B., Regis, J. & Levivier, M. (2006) Effect of beam channel plugging on the outcome of gamma knife radiosurgery for trigeminal neuralgia. *Int J Radiat Oncol Biol Phys*, 65(4), 1200-5.

Matthies, C. & Samii, M. (1997) Management of 1000 vestibular schwannomas (acoustic neuromas): clinical presentation. *Neurosurgery*, 40(1), 1-9; discussion 9-10.

McGee, K. P., Ivanovic, V., Felmlee, J. P., Meyer, F. B., Pollock, B. E. & Huston, J. (2006) MR angiography fusion technique for treatment planning of intracranial arteriovenous malformations. *J Magn Reson Imaging*, 23(3), 361-9.

Metz, C. E. (2008) ROC analysis in medical imaging: a tutorial review of the literature. *Radiol Phys Technol*, 1(1), 2-12.

Mohr, J. P., Kejda-Scharler, J. & Pile-Spellman, J. (2013) Diagnosis and treatment of arteriovenous malformations. *Curr Neurol Neurosci Rep*, 13(2), 324.

Mohr, J. P., Parides, M. K., Stapf, C., Moquete, E., Moy, C. S., Overbey, J. R., Al-Shahi Salman, R., Vicaut, E., Young, W. L., Houdart, E., Cordonnier, C., Stefani, M. A., Hartmann, A., von Kummer, R., Biondi, A., Berkefeld, J., Klijn, C. J., Harkness, K., Libman, R., Barreau, X. & Moskowitz, A. J. (2014) Medical management with or without interventional therapy for unruptured brain arteriovenous malformations (ARUBA): a multicentre, non-blinded, randomised trial. *Lancet*, 383(9917), 614-21.

Moosa, S., Chen, C. J., Ding, D., Lee, C. C., Chivukula, S., Starke, R. M., Yen, C. P., Xu, Z. & Sheehan, J. P. (2014) Volume-staged versus dose-staged radiosurgery outcomes for large intracranial arteriovenous malformations. *Neurosurg Focus*, 37(3), E18.

Morris, Z., Whiteley, W. N., Longstreth, W. T., Jr., Weber, F., Lee, Y. C., Tsushima, Y., Alphs, H., Ladd, S. C., Warlow, C., Wardlaw, J. M. & Al-Shahi Salman, R. (2009) Incidental findings on brain magnetic resonance imaging: systematic review and meta-analysis. *BMJ*, 339, b3016.

Moskvin, V., Timmerman, R., DesRosiers, C., Randall, M., DesRosiers, P., Dittmer, P. & Papiez, L. (2004) Monte carlo simulation of the Leksell Gamma Knife: II. Effects of heterogeneous versus homogeneous media for stereotactic radiosurgery. *Phys Med Biol*, 49(21), 4879-95.

Mukherji, S. K., Quisling, R. G., Kubilis, P. S., Finn, J. P. & Friedman, W. A. (1995) Intracranial arteriovenous malformations: quantitative analysis of magnitude contrast MR angiography versus gradient-echo MR imaging versus conventional angiography. *Radiology*, 196(1), 187-93.

Myrseth, E., Pedersen, P. H., Møller, P. & Lund-Johansen, M. (2007) Treatment of vestibular schwannomas. Why, when and how? *Acta Neurochir (Wien)*, 149(7), 647-60; discussion 660.

Nagaraja, S., Capener, D., Coley, S. C., Lee, K. J., Wilkinson, I. D., Kemeny, A. A. & Griffiths, P. D. (2005) Brain arteriovenous malformations: measurement of nidal volume using a combination of static and dynamic magnetic resonance angiography techniques. *Neuroradiology*, 47(5), 387-92.

Nagy, G., Rowe, J. G., Radatz, M. W., Hodgson, T. J., Coley, S. C. & Kemeny, A. A. (2012) A historical analysis of single-stage γ knife radiosurgical treatment for large arteriovenous malformations: evolution and outcomes. *Acta Neurochir (Wien)*, 154(3), 383-94.

Nakamura, M., Yoneyama, M., Tabuchi, T., Takemura, A., Obara, M. & Sawano, S. (2012) Non-contrast time-resolved magnetic resonance angiography combining high resolution multiple phase echo planar imaging based signal targeting and alternating radiofrequency contrast inherent inflow enhanced multi phase angiography combining spatial resolution echo planar imaging based signal targeting and alternating radiofrequency in intracranial arteries. *Nihon Hoshasen Gijutsu Gakkai Zasshi*, 68(11), 1525-32.

Nakamura, M., Yoneyama, M., Tabuchi, T., Takemura, A., Obara, M., Tatsuno, S. & Sawano, S. (2013) Vessel-selective, non-contrast enhanced, time-resolved MR angiography with vessel-selective arterial spin labeling technique (CINEMA-SELECT) in intracranial arteries. *Radiol Phys Technol*, 6(2), 327-34.

Nakazawa, H., Komori, M., Mori, Y., Hagiwara, M., Shibamoto, Y., Tsugawa, T., Hashizume, C. & Kobayashi, T. (2014a) Effect of skull contours on dose calculations in Gamma Knife Perfexion stereotactic radiosurgery. *J Appl Clin Med Phys*, 15(2), 4603.

Nakazawa, H., Komori, M., Shibamoto, Y., Tsugawa, T., Mori, Y. & Kobayashi, T. (2014b) Dosimetric comparison of absolute and relative dose distributions between tissue maximum ratio and convolution algorithms for acoustic neurinoma plans in Gamma Knife radiosurgery. *Acta Neurochir (Wien)*, 156(8), 1483-9; discussion 1489.

Nakazawa, H., Mori, Y., Komori, M., Shibamoto, Y., Tsugawa, T., Kobayashi, T. & Hashizume, C. (2014c) Validation of accuracy in image co-registration with computed tomography and magnetic resonance imaging in Gamma Knife radiosurgery. *J Radiat Res*, 55(5), 924-33.

Nakazawa, H., Mori, Y., Yamamuro, O., Komori, M., Shibamoto, Y., Uchiyama, Y., Tsugawa, T. & Hagiwara, M. (2014d) Geometric accuracy of 3D coordinates of the Leksell stereotactic skull frame in 1.5 Tesla- and 3.0 Tesla-magnetic resonance imaging: a comparison of three different fixation screw materials. *J Radiat Res*, 55(6), 1184-91.

Novotny, J., Jr., Bhatnagar, J. P., Xu, Y. & Huq, M. S. (2014) Long-term stability of the Leksell Gamma Knife(R) Perfexion patient positioning system (PPS). *Med Phys*, 41(3), 031711.

Nurmikko, T. J. & Eldridge, P. R. (2001) Trigeminal neuralgia--pathophysiology, diagnosis and current treatment. *Br J Anaesth*, 87(1), 117-32.

Paddick, I. (2000) A simple scoring ratio to index the conformity of radiosurgical treatment plans. Technical note. *J Neurosurg*, 93 Suppl 3, 219-22.

Paddick, I. & Lippitz, B. (2006) A simple dose gradient measurement tool to complement the conformity index. *J Neurosurg*, 105 Suppl, 194-201.

Paddick, I. & Motti, E. (2013) Targeting and conformality in arteriovenous malformation radiosurgery. *Prog Neurol Surg*, 27, 35-48.

Park, H. S., Wang, E. H., Rutter, C. E., Corso, C. D., Chiang, V. L. & Yu, J. B. (2016) Changing practice patterns of Gamma Knife versus linear accelerator-based stereotactic radiosurgery for brain metastases in the US. *J Neurosurg*, 124(4), 1018-24.

Patel, R. R. & Mehta, M. P. (2007) Targeted therapy for brain metastases: improving the therapeutic ratio. *Clin Cancer Res*, 13(6), 1675-83.

Petersen, E. T., Zimine, I., Ho, Y.-C. L. & Golay, X. (2014) Non-invasive measurement of perfusion: a critical review of arterial spin labelling techniques. http://dx.doi.org/10.1259/bjr/67705974.

Petersen, E. T., Zimine, I., Ho, Y. C. & Golay, X. (2006) Non-invasive measurement of perfusion: a critical review of arterial spin labelling techniques. *Br J Radiol*, 79(944), 688-701.

Petti, P. L., Larson, D. A. & Kunwar, S. (2008) Use of hybrid shots in planning Perfexion Gamma Knife treatments for lesions close to critical structures. *J Neurosurg*, 109 Suppl, 34-40.

Pollock, B. E., Link, M. J. & Foote, R. L. (2009) Failure rate of contemporary low-dose radiosurgical technique for vestibular schwannoma. *J Neurosurg*, 111(4), 840-4.

Pollock, B. E., Link, M. J., Stafford, S. L., Garces, Y. I. & Foote, R. L. (2016) Stereotactic Radiosurgery for Arteriovenous Malformations: The Effect of Treatment Period on Patient Outcomes. *Neurosurgery*, 78(4), 499-509.

Pollock, B. E., Storlie, C. B., Link, M. J., Stafford, S. L., Garces, Y. I. & Foote, R. L. (2017) Comparative analysis of arteriovenous malformation grading scales in predicting outcomes after stereotactic radiosurgery. *J Neurosurg*, 126(3), 852-858.

Potts, M. B., Sheth, S. A., Louie, J., Smyth, M. D., Sneed, P. K., McDermott, M. W., Lawton, M. T., Young, W. L., Hetts, S. W., Fullerton, H. J. & Gupta, N. (2014) Stereotactic radiosurgery at a low marginal dose for the treatment of pediatric arteriovenous malformations: obliteration, complications, and functional outcomes. *J Neurosurg Pediatr*, 14(1), 1-11.

Regis, J., Metellus, P., Hayashi, M., Roussel, P., Donnet, A. & Bille-Turc, F. (2006) Prospective controlled trial of gamma knife surgery for essential trigeminal neuralgia. *J Neurosurg*, 104(6), 913-24.

Robson, P. M., Dai, W., Shankaranarayanan, A., Rofsky, N. M. & Alsop, D. C. (2010) Time-resolved vessel-selective digital subtraction MR angiography of the cerebral vasculature with arterial spin labeling. *Radiology*, 257(2), 507-15.

Rogers, C. L., Shetter, A. G., Fiedler, J. A., Smith, K. A., Han, P. P. & Speiser, B. L. (2000) Gamma knife radiosurgery for trigeminal neuralgia: the initial experience of The Barrow Neurological Institute. *Int J Radiat Oncol Biol Phys*, 47(4), 1013-9.

Rojas Villabona, A., Benedetta Pizzini, F., Solbach, T., Ricciardi, G., Sokolska, M., Lemonis, C., De Vita, E., Suzuki, Y., Van Osch, M., Foroni, R., Montemezzi, S., Atkinson, D., Longhi, M., Ciceri, E., Kitchen, N., Nicolato, A., Golay, X. & Jager, R. (2017) Triple Magnetic Resonance Angiography (Triple-MRA) for Confirmation of Obliteration Following Gamma Knife Radiosurgery for Arterial-Venous Malformations of the Brain, *Proceedings of the International Society for Magnetic Resonance in Medicine*. Honolulu, Hawaii, USA.

Rojas-Villabona, A., Miszkiel, K., Kitchen, N., Jäger, R. & Paddick, I. (2016a) Evaluation of the stability of the stereotactic Leksell Frame G in Gamma Knife radiosurgery. *J Appl Clin Med Phys*, 17(3), 5944.

Rojas-Villabona, A., Miszkiel, K., Kitchen, N., Jäger, R. & Paddick, I. (2016b) Evaluation of the stability of the stereotactic Leksell Frame G in Gamma Knife radiosurgery. *J Appl Clin Med Phys*, 17(3), 75-89.

Rojas-Villabona, A., Sokolska, M., De Vita, E., Murphy, M., Solbach, T., Grieve, J., Rangi, P., Suzuki, Y., Van Osch, M., Atkinson, D., Biondetti, E., Shmueli, K., Golay, X., Paddick, I., Kitchen, N. & Jager, R. (2017) Triple Magnetic Resonance Angiography (Triple-MRA) for Planning of Gamma Knife Radiosurgery of Brain Arteriovenous Malformations, *Proceedings of the International Society for Magnetic Resonance in Medicine*. Honolulu, Hawaii, USA.

Rubin, B. A., Brunswick, A., Riina, H. & Kondziolka, D. (2014) Advances in radiosurgery for arteriovenous malformations of the brain. *Neurosurgery*, 74 Suppl 1, S50-9.

Ruschin, M., Komljenovic, P. T., Ansell, S., Menard, C., Bootsma, G., Cho, Y. B., Chung, C. & Jaffray, D. (2013) Cone beam computed tomography image guidance system for a dedicated intracranial radiosurgery treatment unit. *Int J Radiat Oncol Biol Phys*, 85(1), 243-50.

Safain, M. G., Rahal, J. P., Raval, A., Rivard, M. J., Mignano, J. E., Wu, J. K. & Malek, A. M. (2014) Use of cone-beam computed tomography angiography in planning for gamma knife radiosurgery for arteriovenous malformations: a case series and early report. *Neurosurgery*, 74(6), 682-96.

Salvetti, D. J., Nagaraja, T. G., McNeill, I. T., Xu, Z. & Sheehan, J. (2013) Gamma Knife surgery for the treatment of 5 to 15 metastases to the brain: clinical article. *J Neurosurg*, 118(6), 1250-7.

Sandstrom, H., Nordstrom, H., Johansson, J., Kjall, P., Jokura, H. & Toma-Dasu, I. (2014) Variability in target delineation for cavernous sinus meningioma and anaplastic astrocytoma in stereotactic radiosurgery with Leksell Gamma Knife Perfexion. *Acta Neurochir (Wien)*, 156(12), 2303-12; discussion 2312-3.

Santacroce, A., Walier, M., Régis, J., Liščák, R., Motti, E., Lindquist, C., Kemeny, A., Kitz, K., Lippitz, B., Martínez Álvarez, R., Pedersen, P. H., Yomo, S., Lupidi, F., Dominikus, K., Blackburn, P., Mindermann, T., Bundschuh, O., van Eck, A. T., Fimmers, R. & Horstmann, G. A. (2012) Long-term tumor control of benign intracranial meningiomas after radiosurgery in a series of 4565 patients. *Neurosurgery*, 70(1), 32-9; discussion 39.

Schlesinger, D., Xu, Z., Taylor, F., Yen, C. P. & Sheehan, J. (2012) Interfraction and intrafraction performance of the Gamma Knife Extend system for patient positioning and immobilization. *J Neurosurg*, 117 Suppl, 217-24.

Schneider, B. F., Eberhard, D. A. & Steiner, L. E. (1997) Histopathology of arteriovenous malformations after gamma knife radiosurgery. *J Neurosurg*, 87(3), 352-7.

Schouten, L. J., Rutten, J., Huveneers, H. A. & Twijnstra, A. (2002) Incidence of brain metastases in a cohort of patients with carcinoma of the breast, colon, kidney, and lung and melanoma. *Cancer*, 94(10), 2698-705.

Sempau, J., Sánchez-Reyes, A., Salvat, F., ben Tahar, H. O., Jiang, S. B. & Fernández-Varea, J. M. (2001) Monte Carlo simulation of electron beams from an accelerator head using PENELOPE. *Phys Med Biol*, 46(4), 1163-86.

Seymour, Z. A., Sneed, P. K., Gupta, N., Lawton, M. T., Molinaro, A. M., Young, W., Dowd, C. F., Halbach, V. V., Higashida, R. T. & McDermott, M. W. (2016) Volume-staged radiosurgery for large arteriovenous malformations: an evolving paradigm. *J Neurosurg*, 124(1), 163-74.

Shaw, E., Kline, R., Gillin, M., Souhami, L., Hirschfeld, A., Dinapoli, R. & Martin, L. (1993) Radiation Therapy Oncology Group: radiosurgery quality assurance guidelines. *Int J Radiat Oncol Biol Phys*, 27(5), 1231-9.

Sheehan, J. P., Williams, B. J. & Yen, C. P. (2010) Stereotactic radiosurgery for WHO grade I meningiomas. *J Neurooncol*, 99(3), 407-16.

Sheehan, J. P., Yen, C. P., Lee, C. C. & Loeffler, J. S. (2014) Cranial stereotactic radiosurgery: current status of the initial paradigm shifter. *J Clin Oncol*, 32(26), 2836-46.

Shin, K. E., Ahn, K. J., Choi, H. S., Jung, S. L., Kim, B. S., Jeon, S. S. & Hong, Y. G. (2014) DCE and DSC MR perfusion imaging in the differentiation of recurrent tumour from treatment-related changes in patients with glioma. *Clin Radiol*, 69(6), e264-72.

Shrimpton, P. C., Hillier, M. C., Lewis, M. A. & Dunn, M. (2006) National survey of doses from CT in the UK: 2003. *Br J Radiol*, 79(948), 968-80.

Shtraus, N., Schifter, D., Corn, B. W., Maimon, S., Alani, S., Frolov, V., Matceyevsky, D. & Kanner, A. A. (2010) Radiosurgical treatment planning of AVM following embolization with Onyx: possible dosage error in treatment planning can be averted. *J Neurooncol*, 98(2), 271-6.

Simon, S. L., Douglas, P., Baltuch, G. H. & Jaggi, J. L. (2005) Error analysis of MRI and leksell stereotactic frame target localization in deep brain stimulation surgery. *Stereotact Funct Neurosurg*, 83(1), 1-5.

Soize, S., Bouquigny, F., Kadziolka, K., Portefaix, C. & Pierot, L. (2014) Value of 4D MR angiography at 3T compared with DSA for the follow-up of treated brain arteriovenous malformation. *AJNR Am J Neuroradiol*, 35(10), 1903-9.

Spetzler, R. F. & Martin, N. A. (1986) A proposed grading system for arteriovenous malformations. *J Neurosurg*, 65(4), 476-83.

St George, E. J., Butler, P. & Plowman, P. N. (2002) Can magnetic resonance imaging alone accurately define the arteriovenous nidus for gamma knife radiosurgery? *J Neurosurg*, 97(5 Suppl), 464-70.

Stapf, C., Labovitz, D. L., Sciacca, R. R., Mast, H., Mohr, J. P. & Sacco, R. L. (2002) Incidence of adult brain arteriovenous malformation hemorrhage in a prospective population-based stroke survey. *Cerebrovasc Dis*, 13(1), 43-6.

Stapf, C., Mast, H., Sciacca, R. R., Choi, J. H., Khaw, A. V., Connolly, E. S., Pile-Spellman, J. & Mohr, J. P. (2006) Predictors of hemorrhage in patients with untreated brain arteriovenous malformation. *Neurology*, 66(9), 1350-5.

Starke, R. M., Kano, H., Ding, D., Lee, J. Y., Mathieu, D., Whitesell, J., Pierce, J. T., Huang, P. P., Kondziolka, D., Yen, C. P., Feliciano, C., Rodgriguez-Mercado, R., Almodovar, L., Pieper, D. R., Grills, I. S., Silva, D., Abbassy, M., Missios, S., Barnett, G. H., Lunsford, L. D. & Sheehan, J. P. (2017) Stereotactic radiosurgery for cerebral arteriovenous malformations: evaluation of long-term outcomes in a multicenter cohort. *J Neurosurg*, 126(1), 36-44.

Steiner, L., Leksell, L., Greitz, T., Forster, D. M. & Backlund, E. O. (1972) Stereotaxic radiosurgery for cerebral arteriovenous malformations. Report of a case. *Acta Chir Scand*, 138(5), 459-64.

Suzuki, Y., Fujima, N., Ogino, T., Meakin, J. A., Suwa, A., Sugimori, H., Van Cauteren, M. & van Osch, M. J. (2017) Acceleration of ASL-based time-resolved

MR angiography by acquisition of control and labeled images in the same shot (ACTRESS). *Magn Reson Med*.

Suzuki, Y., Teeuwisse, M. & Schmid, S. (2014) Improving 4D pCASL angiography by combining Hadamard time-encoding with Look-Locker readout. *Proc. Intl. Soc. Mag. Reson. Med.*

Swan, J. S., Carroll, T. J., Kennell, T. W., Heisey, D. M., Korosec, F. R., Frayne, R., Mistretta, C. A. & Grist, T. M. (2002) Time-resolved three-dimensional contrast-enhanced MR angiography of the peripheral vessels. *Radiology*, 225(1), 43-52.

Taschner, C. A., Gieseke, J., Le Thuc, V., Rachdi, H., Reyns, N., Gauvrit, J. Y. & Leclerc, X. (2008) Intracranial arteriovenous malformation: time-resolved contrast-enhanced MR angiography with combination of parallel imaging, keyhole acquisition, and k-space sampling techniques at 1.5 T. *Radiology*, 246(3), 871-9.

Taschner, C. A., Le Thuc, V., Reyns, N., Gieseke, J., Gauvrit, J. Y., Pruvo, J. P. & Leclerc, X. (2007) Gamma Knife surgery for arteriovenous malformations in the brain: integration of time-resolved contrast-enhanced magnetic resonance angiography into dosimetry planning. Technical note. *J Neurosurg*, 107(4), 854-9.

Teksam, M., McKinney, A., Casey, S., Asis, M., Kieffer, S. & Truwit, C. L. (2004) Multi-section CT angiography for detection of cerebral aneurysms. *AJNR Am J Neuroradiol*, 25(9), 1485-92.

Tsao, M. N., Lloyd, N., Wong, R. K., Chow, E., Rakovitch, E., Laperriere, N., Xu, W. & Sahgal, A. (2012) Whole brain radiotherapy for the treatment of newly diagnosed multiple brain metastases. *Cochrane Database Syst Rev*, 4, CD003869.

United Nations Scientific Committee on the Effects of Atomic Radiation. Sources and effects of ionizing radiation (2000) Vol 1, Chapter Vol. 1: Sources. New York, NY: United Nations Publishing; 2000.:

van Beijnum, J., van der Worp, H. B., Buis, D. R., Al-Shahi Salman, R., Kappelle, L. J., Rinkel, G. J., van der Sprenkel, J. W., Vandertop, W. P., Algra, A. & Klijn, C. J. (2011) Treatment of brain arteriovenous malformations: a systematic review and meta-analysis. *JAMA*, 306(18), 2011-9.

Vanderstraeten, B., Reynaert, N., Paelinck, L., Madani, I., De Wagter, C., De Gersem, W., De Neve, W. & Thierens, H. (2006) Accuracy of patient dose calculation for lung IMRT: A comparison of Monte Carlo, convolution/superposition, and pencil beam computations. *Med Phys*, 33(9), 3149-58.

Verheul, J. B., Hanssens, P. E., Lie, S. T., Leenstra, S., Piersma, H. & Beute, G. N. (2010) Gamma Knife surgery for trigeminal neuralgia: a review of 450 consecutive cases. *J Neurosurg*, 113 Suppl, 160-7.

Wall, B. F. & Hart, D. (1997) Revised radiation doses for typical X-ray examinations. Report on a recent review of doses to patients from medical X-ray examinations in the UK by NRPB. National Radiological Protection Board. *Br J Radiol*, 70(833), 437-9.

Walton, L., Bomford, C. K. & Ramsden, D. (1987) The Sheffield stereotactic radiosurgery unit: physical characteristics and principles of operation. *Br J Radiol*, 60(717), 897-906.

Walton, L., Hampshire, A., Brownett, C., Soanes, T., Vaughan, P., Rowe, J., Radatz, M. & Kemeny, A. (2002) Rotational movements of the automatic positioning system under load and their significance for patient treatments. *J Neurosurg*, 97(5 Suppl), 569-73.

Warren, D. J., Hoggard, N., Walton, L., Radatz, M. W., Kemeny, A. A., Forster, D. M., Wilkinson, I. D. & Griffiths, P. D. (2001) Cerebral arteriovenous malformations: comparison of novel magnetic resonance angiographic techniques and conventional catheter angiography. *Neurosurgery*, 48(5), 973-82; discussion 982-3.

Willinek, W. A., Hadizadeh, D. R., von Falkenhausen, M., Urbach, H., Hoogeveen, R., Schild, H. H. & Gieseke, J. (2008) 4D time-resolved MR angiography with keyhole (4D-TRAK): more than 60 times accelerated MRA using a combination of CENTRA, keyhole, and SENSE at 3.0T. *J Magn Reson Imaging*, 27(6), 1455-60.

Wrede, K. H., Johst, S., Dammann, P., Özkan, N., Mönninghoff, C., Kraemer, M., Maderwald, S., Ladd, M. E., Sure, U., Umutlu, L. & Schlamann, M. (2014) Improved cerebral time-of-flight magnetic resonance angiography at 7 Tesla--feasibility study and preliminary results using optimized venous saturation pulses. *PLoS One*, 9(9), e106697.

Wright, G., Bownes, P. & Reiner, B. (2011) A comparison of four skull models for independent dose calculations for Gamma Knife PERFEXION. *Med Phys*, 38(2), 884-90.

Wu, H., Block, W. F., Turski, P. A., Mistretta, C. A., Rusinak, D. J., Wu, Y. & Johnson, K. M. (2013) Noncontrast dynamic 3D intracranial MR angiography using pseudo-continuous arterial spin labeling (PCASL) and accelerated 3D radial acquisition. *J Magn Reson Imaging*.

Wu, W. C., Fernández-Seara, M., Detre, J. A., Wehrli, F. W. & Wang, J. (2007) A theoretical and experimental investigation of the tagging efficiency of pseudocontinuous arterial spin labeling. *Magn Reson Med*, 58(5), 1020-7.

Wu, X., Ting, J. Y., Markoe, A. M., Landy, H. J., Fiedler, J. A. & Russell, J. (1996) Stereotactic dose computation and plan optimization using the convolution theorem. I. Dose computation. *Stereotact Funct Neurosurg*, 66 Suppl 1, 302-8.

Xu, A. Y., Bhatnagar, J., Bednarz, G., Niranjan, A., Flickinger, J., Lunsford, L. D. & Huq, M. S. (2014) Dose differences between the three dose calculation algorithms in Leksell GammaPlan. *J Appl Clin Med Phys*, 15(5), 4844.

Xu, A. Y., Bhatnagar, J., Bednarz, G., Niranjan, A., Kondziolka, D., Flickinger, J., Lunsford, L. D. & Huq, M. S. (2015) Gamma Knife radiosurgery with CT image-based dose calculation. *J Appl Clin Med Phys*, 16(6), 5530.

Xu, G., Rowley, H. A., Wu, G., Alsop, D. C., Shankaranarayanan, A., Dowling, M., Christian, B. T., Oakes, T. R. & Johnson, S. C. (2010) Reliability and precision of pseudo-continuous arterial spin labeling perfusion MRI on 3.0 T and comparison with 15O-water PET in elderly subjects at risk for Alzheimer's disease. *NMR Biomed*, 23(3), 286-93.

Yamakami, I., Uchino, Y., Kobayashi, E. & Yamaura, A. (2003) Conservative management, gamma-knife radiosurgery, and microsurgery for acoustic neurinomas: a systematic review of outcome and risk of three therapeutic options. *Neurol Res*, 25(7), 682-90.

Yan, L., Wang, S., Zhuo, Y., Wolf, R. L., Stiefel, M. F., An, J., Ye, Y., Zhang, Q., Melhem, E. R. & Wang, D. J. (2010) Unenhanced dynamic MR angiography: high spatial and temporal resolution by using true FISP-based spin tagging with alternating radiofrequency. *Radiology*, 256(1), 270-9.

Yang, J. J., Hill, M. D., Morrish, W. F., Hudon, M. E., Barber, P. A., Demchuk, A. M., Sevick, R. J. & Frayne, R. (2002) Comparison of pre- and postcontrast 3D time-of-flight MR angiography for the evaluation of distal intracranial branch occlusions in acute ischemic stroke. *AJNR Am J Neuroradiol*, 23(4), 557-67.

Yen, C. P., Matsumoto, J. A., Wintermark, M., Schwyzer, L., Evans, A. J., Jensen, M. E., Shaffrey, M. E. & Sheehan, J. P. (2013) Radiation-induced imaging changes following Gamma Knife surgery for cerebral arteriovenous malformations. *J Neurosurg*, 118(1), 63-73.

Yoshimoto, Y. (2005) Systematic review of the natural history of vestibular schwannoma. *J Neurosurg*, 103(1), 59-63.

Yu, C., Apuzzo, M. L., Zee, C. S. & Petrovich, Z. (2001) A phantom study of the geometric accuracy of computed tomographic and magnetic resonance imaging

stereotactic localization with the Leksell stereotactic system. *Neurosurgery*, 48(5), 1092-8; discussion 1098-9.

Yu, C., Petrovich, Z., Apuzzo, M. L., Zelman, V. & Giannotta, S. L. (2004) Study of magnetic resonance imaging-based arteriovenous malformation delineation without conventional angiography. *Neurosurgery*, 54(5), 1104-; discussion 1108-10.

Yu, S., Yan, L., Yao, Y., Wang, S., Yang, M., Wang, B., Zhuo, Y., Ai, L., Miao, X., Zhao, J. & Wang, D. J. (2012) Noncontrast dynamic MRA in intracranial arteriovenous malformation (AVM), comparison with time of flight (TOF) and digital subtraction angiography (DSA). *Magn Reson Imaging*, 30(6), 869-77.

Zakrzewska, J. M. (2002) Diagnosis and differential diagnosis of trigeminal neuralgia. *Clin J Pain*, 18(1), 14-21.

Zakrzewska, J. M. & Coakham, H. B. (2012) Microvascular decompression for trigeminal neuralgia: update. *Curr Opin Neurol*, 25(3), 296-301.

Zimm, S., Wampler, G. L., Stablein, D., Hazra, T. & Young, H. F. (1981) Intracerebral metastases in solid-tumor patients: natural history and results of treatment. *Cancer*, 48(2), 384-94.

Appendices

Appendix 1. Confirmation of ethical opinion for the convolution project.

Health Research Authority
NRES Committee London - Queen Square
HRA Head Office
Skipton House
80 London Road
London
SE1 6LH

Telephone: 020 7972 2567
Facsimile: 020 7972 2592

20 August 2013

Mr Neil/NK Kitchen
Head of Division of Neurosurgery, Consultant Neurosurgeon,
University College London Hospitals NHS Foundation Trust
National Hospital for Neurology and Neurosuegery
Queen Square
London, WC1N 3BG

Dear Mr Kitchen

Study title:	**EVALUATION OF DOSIMETRIC DIFFERENCES BETWEEN THE TMR 10 AND CONVOLUTION ALGORITHM FOR GAMMA KNIFE RADIOSURGERY PLANNING**
REC reference:	**13/LO/0851**
IRAS project ID:	**128269**

Thank you for your letter of 29 July 2013, responding to the Committee's request for further information on the above research and submitting revised documentation.

The further information has been considered on behalf of the Committee by the Chair.

We plan to publish your research summary wording for the above study on the NRES website, together with your contact details, unless you expressly withhold permission to do so. Publication will be no earlier than three months from the date of this favourable opinion letter. Should you wish to provide a substitute contact point, require further information, or wish to withhold permission to publish, please contact the Co-ordinator Mrs Nischinth Cherodian, NRESCommittee.SECoast-BrightonandSussex@nhs.net.

Confirmation of ethical opinion

On behalf of the Committee, I am pleased to confirm a favourable ethical opinion for the above research on the basis described in the application form, protocol and supporting documentation as revised, subject to the conditions specified below.

Ethical review of research sites

NHS sites

The favourable opinion applies to all NHS sites taking part in the study, subject to management permission being obtained from the NHS/HSC R&D office prior to the start of the study (see "Conditions of the favourable opinion" below).

Non-NHS sites

Conditions of the favourable opinion

The favourable opinion is subject to the following conditions being met prior to the start of the study.

Management permission or approval must be obtained from each host organisation prior to the start of the study at the site concerned.

Management permission ("R&D approval") should be sought from all NHS organisations involved in the study in accordance with NHS research governance arrangements.

Guidance on applying for NHS permission for research is available in the Integrated Research Application System or at http://www.rdforum.nhs.uk.

Where a NHS organisation's role in the study is limited to identifying and referring potential participants to research sites ("participant identification centre"), guidance should be sought from the R&D office on the information it requires to give permission for this activity.

For non-NHS sites, site management permission should be obtained in accordance with the procedures of the relevant host organisation.

Sponsors are not required to notify the Committee of approvals from host organisations

It is the responsibility of the sponsor to ensure that all the conditions are complied with before the start of the study or its initiation at a particular site (as applicable).

Approved documents

The final list of documents reviewed and approved by the Committee is as follows:

Document	*Version*	*Date*
Investigator CV - Neil David Kitchen		
Letter from Sponsor		07 May 2013
Other: Evidence of insurance - insurance confirmation letter and insurance contract		
Participant Consent Form: 1.4		15 July 2013
Participant Information Sheet	1.4	15 July 2013
Protocol	1.6	29 July 2013
REC application - 128269/454637/1/610		17 May 2013
Response to Request for Further Information		29 July 2013

Statement of compliance

The Committee is constituted in accordance with the Governance Arrangements for Research Ethics Committees and complies fully with the Standard Operating Procedures for Research Ethics Committees in the UK.

After ethical review

Reporting requirements

The attached document *"After ethical review – guidance for researchers"* gives detailed guidance on reporting requirements for studies with a favourable opinion, including:

- Notifying substantial amendments
- Adding new sites and investigators
- Notification of serious breaches of the protocol
- Progress and safety reports
- Notifying the end of the study

The NRES website also provides guidance on these topics, which is updated in the light of changes in reporting requirements or procedures.

Feedback

You are invited to give your view of the service that you have received from the National Research Ethics Service and the application procedure. If you wish to make your views known please use the feedback form available on the website.

Further information is available at National Research Ethics Service website > After Review

13/LO/0851	**Please quote this number on all correspondence**

We are pleased to welcome researchers and R & D staff at our NRES committee members' training days – see details at http://www.hra.nhs.uk/hra-training/

With the Committee's best wishes for the success of this project.

Yours sincerely

pp

Dr Yogi Amin
Chair

Email:NRESCommittee.London-Queensquare@nhs.net

Enclosures: "After ethical review – guidance for researchers"

Copy to: *Mrs Suzanne Binks, Joint Research Office (Part of the Research Support Centre)*

Appendix 2. Ethical considerations of the convolution project.

As submitted to the Queen Square Ethics Committee on 29th July 2013.

This study will be conducted in full conformance with principles of the "Declaration of Helsinki", Good Clinical Practice (GCP) and the UK regulations for research in humans. The research protocol will not modify the treatment that patients should receive by any means. Apart from the potential benefit for the patient to have a more accurate dose calculation method for future GKR, there is not any other direct benefit from participation in the study. The results of this study are very likely to positively impact the quality of dose calculation method for future patients receiving treatment in the QSRC.

The main risk associated with participation in this study is the radiation exposure by an additional CT scan. The radiation received by an adult from a CT scan of the head has been estimated to be 2 mSv (95%CI: 0.9-3.0mSv)(Wall & Hart, 1997). This was confirmed in 2003 by a review of patient doses from CT examinations in over a quarter of all UK scanners (Shrimpton et al, 2006). For comparison, it is several orders of magnitude less than the patients will be receiving from their GKR. In addition, all of us receive about 3 mSv of radiation exposure to natural background radiation every year (UN, 2000). The dose involved in a head CT scan is considered to be a relatively small dose and the risks associated to it are minimal and too small to allow epidemiological detection. Estimates of risk from x-ray exposure have a broad range of statistical uncertainty, and there is controversy regarding the effects from very low doses like the one used in CT scans. The most important of these risks is a 0.01% higher mortality by radiation induced cancer (Brenner & Hall, 2007). The risk of heritable mutations leading to genetically associated diseases in offspring is thought to be very small to observe for radiation doses of the magnitude that are associated with CT procedures(Dauer et al, 2010).

A CT scan of the head is a procedure considered clinically safe and acceptable. It is not an indispensable part of pre-treatment imaging for GKR in the UK;

however, many centres around the world have included stereotactic CT scan of the head as routine for all patients undergoing GKR. Also, it is the imaging technique used on patients unable to undergo MRI scanning (Attia et al, 2012). Handling of this ethical issue is of paramount importance for the research team. Therefore, the scanning sequence has been set up to minimize the radiation received by the patient and the acquisition includes the use of the CARE Dose 4D Automatic exposure Control system, which allows acquisition of images with the required quality giving the lowest possible radiation.

Patients will be counselled on radiation exposure risks, including information about larger radiation-induced cancer mortality and heritable mutations risks, they will be given time to think and discuss about the risk involved by participation. Subjects will be entirely free to decide their involvement in research and they will be able to withdraw at any time without giving any reason.

Personal identifiable information will be adequately handled to minimize the risks of confidentiality aggression. Photographs obtained as part of the research participation will be immediately transferred to the Gamma Knife registry workstation where they will be stored and used only for research purposes. They will be safely stored in the Gamma Knife premises together with the project master file and no third party will have access to these records. Only anonymised information will be removed from the Gamma Knife premises for analysis. Written consent will be taken to use anonymised images or information of treatment plans in scientific conferences or paired reviewed scientific journals.

There is not any conflict of interest to be declared for the study.

Appendix 3. Confirmation of ethical opinion for the study on triple-MRA for planning of GKR for brain AVMs.

NHS
Health Research Authority
National Research Ethics Service

NRES Committee London - Queen Square
HRA NRES Centre Manchester
Barlow House
3rd Floor
4 Minshull Street
Manchester
M1 3DZ

Telephone: 0161 625 7816
Fax: 0161 625 7299

20 January 2015

Dr Rolf Jager
8-11 Queen Square
London, UK
Queen Square, London, UK.
WC1 N3BG

Dear Dr Jager

Study title:	**Optimization of magnetic resonance vascular imaging for planning and follow up of Gamma Knife Radiosurgery for brain arteriovenous malformations**
REC reference:	**15/LO/0033**
Protocol number:	**v 1.1 - 23/10/2014**
IRAS project ID:	**155348**

The Research Ethics Committee reviewed the above application at the meeting held on 15 January 2015. The Committee thank Dr Villabona for attending the meeting to discuss the application.

We plan to publish your research summary wording for the above study on the HRA website, together with your contact details. Publication will be no earlier than three months from the date of this favourable opinion letter. The expectation is that this information will be published for all studies that receive an ethical opinion but should you wish to provide a substitute contact point, wish to make a request to defer, or require further information, please contact the REC Manager Miss Rachel Heron, nrescommittee.london-queensquare@nhs.net. Under very limited circumstances (e.g. for student research which has received an unfavourable opinion), it may be possible to grant an exemption to the publication of the study.

Ethical opinion

The members of the Committee present gave a favourable ethical opinion of the above research on the basis described in the application form, protocol and supporting documentation, subject to the conditions specified below.

Conditions of the favourable opinion

The favourable opinion is subject to the following conditions being met prior to the start of the study.

1) Participant Information:
   a) The study was a feasibility study. This should be made clear on the participant information.
   b) Contact details for the student should be added.
2) Consent forms: in Section 9 of the consent form for follow-up patients, the phrase 'do I have to have gamma knife surgery?' is redundant as patients would have already had surgery. This should be removed.

You should notify the REC in writing once all conditions have been met (except for site approvals from host organisations) and provide copies of any revised documentation with updated version numbers. The REC will acknowledge receipt and provide a final list of the approved documentation for the study, which can be made available to host organisations to facilitate their permission for the study. Failure to provide the final versions to the REC may cause delay in obtaining permissions.

Management permission or approval must be obtained from each host organisation prior to the start of the study at the site concerned.

Management permission ("R&D approval") should be sought from all NHS organisations involved in the study in accordance with NHS research governance arrangements.

Guidance on applying for NHS permission for research is available in the Integrated Research Application System or at http://www.rdforum.nhs.uk.

Where a NHS organisation's role in the study is limited to identifying and referring potential participants to research sites ("participant identification centre"), guidance should be sought from the R&D office on the information it requires to give permission for this activity.

For non-NHS sites, site management permission should be obtained in accordance with the procedures of the relevant host organisation.

Sponsors are not required to notify the Committee of approvals from host organisations.

Registration of Clinical Trials

All clinical trials (defined as the first four categories on the IRAS filter page) must be registered on a publically accessible database. This should be before the first participant is recruited but no later than 6 weeks after recruitment of the first participant.

There is no requirement to separately notify the REC but you should do so at the earliest opportunity e.g. when submitting an amendment. We will audit the registration details as part of the annual progress reporting process.

To ensure transparency in research, we strongly recommend that all research is registered but for non-clinical trials this is not currently mandatory.

If a sponsor wishes to request a deferral for study registration within the required timeframe, they should contact hra.studyregistration@nhs.net. The expectation is that all clinical trials will be registered, however, in exceptional circumstances non registration may be

permissible with prior agreement from NRES. Guidance on where to register is provided on the HRA website.

It is the responsibility of the sponsor to ensure that all the conditions are complied with before the start of the study or its initiation at a particular site (as applicable).

Ethical review of research sites

NHS Sites

The favourable opinion applies to all NHS sites taking part in the study taking part in the study, subject to management permission being obtained from the NHS/HSC R&D office prior to the start of the study (see "Conditions of the favourable opinion" below).

Non NHS sites

The Committee has not yet completed any site-specific assessment(s) (SSA) for the non-NHS research site(s) taking part in this study. The favourable opinion does not therefore apply to any non-NHS site at present. I will write to you again as soon as an SSA application(s) has been reviewed. In the meantime no study procedures should be initiated at non-NHS sites.

Summary of discussion at the meeting

Social or scientific value; scientific design and conduct of the study

The Committee agreed that the study had scientific value. The design was difficult to follow due to the technical language used throughout the application. It was not clear whether the comparison between conventional angio and MRA was qualitative or quantitative.

Dr Villabona elaborated that the team would look at the MRA and MRI scans and use a software tool to draw around the tumour (AVM) on a computer screen, looking at the volume and location. Following treatment as normal, they would again draw the lesion. They would then evaluate the treatment, and a score would be given for residual lesion.

The Committee enquired if the MRA results would be used for surgical planning.

Dr Villabona confirmed that this would not happen during the trial.

Favourable risk benefit ratio; anticipated benefit/risks for research participants (present and future)

There were no direct benefits to participants in the study.

The Committee noted that the care pathway was altered to prevent the need to administer the contrast agent more than once. The MRI was usually carried out on the day of the surgery, but here was being carried out before the surgery, with a possible gap of 1 month between MRI and surgery. The Committee asked if there would be a need to administer an additional dose of contrast agent to any patient.

Dr Villabona advised that this would only happen if the treatment had to be delayed, and this would be extremely unlikely. He advised that the MRI could be carried out up to a month in advance and still be used for planning.

The Committee asked if patients in the follow-up part of the study would be asked to have an extra MRI as this was not part of routine care at follow up.

Dr Villabona advised that patients would have an MRI every 6 months at follow-up, and at 2 year the patient could be recalled for an angiogram. The researchers would then try to use the scan which had already been done.

The Committee asked if it would be possible for a patient to go through the study twice. *Dr Villabona advised that this would be ideal, but not possible within the timescale of the study.*

Informed consent process and the adequacy and completeness of participant information

The Committee asked for a clarification of the consent process.

Dr Villabona advised that patients would receive a telephone call from the research team at the time of the decision to give the treatment. Consent for the research would not be given on the day of the blood test, which was the day patients consented to the treatment, but at a later date. Patients would have a week to decide whether to participate.

The Committee approved these arrangements.

The Committee noted that the Patient Information Sheet had contact details for the Chief Investigator but not the student, and should include both.

The Committee advised Dr Villabona that minor points relating to the consent form and participant information would be outlined in a letter.

Documents reviewed

The documents reviewed at the meeting were:

Document	*Version*	*Date*
Evidence of Sponsor insurance or indemnity (non NHS Sponsors only) [140791 Insurance Confirmation Letter 04.12.14]	04/12/2014	04 December 2014
IRAS Checklist XML [Checklist_11122014]		11 December 2014
Other [UCL 2014-15 Insurance Certificate]	2014-15	14 July 2014
Other [Academic_supervisor_letter_04122014]	04122014	04 December 2014
Participant consent form [Consent_form_CCA_for_GK_planning]	v1.1	04 December 2014
Participant consent form [Consent_form_CCA_for_response_evaluation_after_GKR]	v2.1	04 December 2014
Participant information sheet (PIS) [PIS_CCA_for_GK_planning]	v2.1	04 December 2014
Participant information sheet (PIS) [PIS_CCA_for_response_evaluation_after_GKR]	v3.1	04 December 2014
REC Application Form [REC_Form_11122014]		11 December 2014
REC Application Form [REC_Form_11122014]		11 December 2014
Referee's report or other scientific critique report [peer_review_verona_01_11_14]	01/11/2014	01 November 2014
Research protocol or project proposal [optimization_MRA_for_GK_of_brain_AVM_Research_protocol_]	v1.2	09 December 2014
Summary CV for Chief Investigator (CI)	v1.1	01 January 2013
Summary CV for student [CV_Villabona_v1.1_07.06.2013]	v1.1	07 June 2013

Summary, synopsis or diagram (flowchart) of protocol in non-technical language [Research_flowchart_MRA_for_GK_v.1.1_04122014]	v 1.1	23 October 2014

Membership of the Committee

The members of the Ethics Committee who were present at the meeting are listed on the attached sheet.

Mrs Claire Reynolds declared that she had worked with the researchers on this study as she used to be employed in the same department; however she was not involved with this particular study. The Committee was happy for her to take part in the discussion.

After ethical review

Reporting requirements

The attached document "After ethical review – guidance for researchers" gives detailed guidance on reporting requirements for studies with a favourable opinion, including:

- Notifying substantial amendments
- Adding new sites and investigators
- Notification of serious breaches of the protocol
- Progress and safety reports
- Notifying the end of the study

The NRES website also provides guidance on these topics, which is updated in the light of changes in reporting requirements or procedures.

User Feedback

The Health Research Authority is continually striving to provide a high quality service to all applicants and sponsors. You are invited to give your view of the service you have received and the application procedure. If you wish to make your views known please use the feedback form available on the HRA website: http://www.hra.nhs.uk/about-the-hra/governance/quality-assurance/

HRA Training

We are pleased to welcome researchers and R&D staff at our training days – see details at http://www.hra.nhs.uk/hra-training/

15/LO/0033	**Please quote this number on all correspondence**

With the Committee's best wishes for the success of this project.

Yours sincerely

Signed on behalf of
Dr Yogi Amin
Chair

E-mail: nrescommittee.london-queensquare@nhs.net

A Research Ethics Committee established by the Health Research Authority

Enclosures: List of names and professions of members who were present at the meeting and those who submitted written comments

"After ethical review – guidance for researchers"

Copy to: Mrs Tabitha/TK Kavoi

Dr Alvaro Villabona

A Research Ethics Committee established by the Health Research Authority

Appendix 4. Confirmation of ethical opinion for the study on triple-MRA for confirmation of obliteration following GKR of brain AVMs.

AZIENDA OSPEDALIERA UNIVERSITARIA INTEGRATA
VERONA
(D.Lgs. n. 517/1999 - Art. 3 L.R.Veneto n. 18/2009)

DIPARTIMENTO DIREZIONE MEDICA OSPEDALIERA E FARMACIA

COMITATO ETICO PER LA SPERIMENTAZIONE CLINICA
DELLE PROVINCE DI VERONA E ROVIGO

UFFICIO DI SEGRETERIA TECNICO-SCIENTIFICA DEL COMITATO ETICO
c/o SERVIZIO DI FARMACIA
Borgo Trento - P.le A. Stefani, 1 - 37126 Verona - Tel. 045 8123236 - Fax 045 8123177
e-mail: comitatoetico.veronarovigo@ospedaleuniverona.it
PEC: *comitatoetico.aoui.vr@pecveneto.it*

Prot. n. 13258 *del* 18/03/2015

Dr.ssa Pizzini Francesca
Neuroradiologia d. O.
OCM

Prof. Piovan Enrico
Neuroradiologia d. O.
OCM

Nucleo Ricerca Clinica AOUI di Verona
c/o Ufficio Supporto alla Ricerca e Biostatistica
OCM

Oggetto: Studio Clinico: "Optimization of magnetic resonance vascular imaging for planning and follow up of Gamma Knife Radiosurgery for brain arteriovenous malformations." – Codice Protocollo MRA Angioraphy

In riferimento alla richiesta di autorizzazione dello studio in oggetto, si trasmettono le decisioni del Comitato Etico per la Sperimentazione Clinica delle Province di Verona e Rovigo riunitosi in data **11/03/2015**.

Si rammenta che per l'attivazione della sperimentazione è necessario attendere:
1. ove previsto, la ricezione dell'autorizzazione della propria Amministrazione

Cordialmente.

Il Responsabile dell'Ufficio di Segreteria del CESC
Dr.ssa Anna Fratucello

Sperimentazione Prog. **454CESC**

N. prog. 454CESC 3

I sopraindicati componenti del Comitato dichiarano di astenersi dal pronunciarsi su quelle sperimentazioni per le quali possa sussistere un conflitto di interessi di tipo diretto o indiretto.

Verona, 11/03/2015

D'Ordine del Presidente del Comitato Etico delle Province di Verona e Rovigo
L'Ufficio di Segreteria
Dott.ssa Anna Fratucello

Appendix 5. Evaluation forms used for assessment of DSA and triple-MRA.

MR vascular imaging for planning and follow up of GKR for brain AVM

EVALUATION SHEET

Confirmation of obliteration after GKR

Research case number: Evaluator:

Institution: London/Verona Review date:

B. CONVENTIONAL CATHETER ANGIOGRAPHY

For the second part of the assessment, please answer the questions based in the information from the DSA **ONLY**.

Examination date: _ _ / _ _/ _ _ _ _

1. Can you detect a vascular abnormality in the DSA?

   Yes *No*

   If "No", please go to question 11 and do not answer questions 2- 10.

2. If "Yes", what is the abnormality?

   ……

3. Where is it located?

   ……

4. Regarding the Spetzler-Martin Grade for the AVM, please complete the table below:

Parameter		***Score***
Approximate lesion volume	Assume the lesion is ellipsoid (a x b x c /2)	
Size of AVM (nidus max diameter)	Small < 3 cm	1
	Medium 3 - 6 cm	2
	Large > 6 cm	3
Eloquence of adjacent brain (brainstem, thalamus, hypothalamus, cerebellar peduncles, sensorimotor, language, and primary visual cortices)	Non eloquent	0
	Eloquent	1
Pattern of venous drainage	Superficial only	0
	Deep	1
Total		

MR vascular imaging for planning and follow up of GKR for brain AVM

5. How many feeding arteries can you identify? (please give a number)

   a. Cortical: ……. b. Deep/perforating: ……. C. Infratentorial: …….

6. What is the main arterial feeder?

   ……

7. How many draining veins can you identify? (please give a number)

   a. Deep: ……. b. Superficial: …….

8. Can you detect any abnormality of the draining veins?

   a. Stenosis b. Varices C. Dilated D.None

9. Can you detect any aneurism associated to this abnormality?

   No *Pre-nidal* *nidal* *post-nidal*

10. Can you observe an extra-nidal arterial-venous fistula in this DSA examination?

    Yes *No*

11. How confident are you of this assessment?

    Not entirely confident *Confident* *Highly confident*

MR vascular imaging for planning and follow up of GKR for brain AVM

EVALUATION SHEET
Confirmation of obliteration after GKR

Research case number: Evaluator:

Institution: London/Verona Review date:

A. MR ANGIOGRAPHY

Please review the MR angiography examinations **ONLY** and answer the following questions:

Examination date: _ _ / _ _/ _ _ _ _
Sequences available: ……

1. Is there any kind of artefact in the images that would affect the quality of your radiological assessment?

   Yes *No*

2. What do you think about the quality of the vessels' representation in the examinations below?

	Poor	***Fair***	***Good***	***Very good***	***Excellent***
TOF					
4D ASL angio					
CE angio					

3. Can you detect a vascular abnormality in these scans?

   Yes *No*

   If "No", please go to question 15 and do not answer questions 4- 14.

4. If "Yes", what is the abnormality?

   ……

5. Where is it located?

   ……

6. What MRA sequences DO show the abnormality?

   ……..

7. What MRA sequences, if any, DO NOT show the abnormality?

   ……

MR vascular imaging for planning and follow up of GKR for brain AVM

8. Regarding the size and Spetzler-Martin Grade for this AVM, please complete the table below:

Parameter		***Score***
Approximate lesion volume	Assume the lesion is ellipsoid (a x b x c /2)	
Size of AVM (nidus max diameter)	Small < 3 cm	1
	Medium 3 - 6 cm	2
	Large > 6 cm	3
Eloquence of adjacent brain (brainstem, thalamus, hypothalamus, cerebellar peduncles, sensorimotor, language, and primary visual cortices)	Non eloquent	0
	Eloquent	1
Pattern of venous drainage	Superficial only	0
	Deep	1
Total		

9. How many feeding arteries can you identify? (please give a number)

   a. Cortical: ……. b. Deep/perforating: ……. C. Infratentorial: …….

10. What is the main arterial feeder?

    ……

11. How many draining veins can you identify? (please give a number)

    a. Deep: ……. b. Superficial: …….

12. Can you detect any abnormality of the draining veins?

    a. Stenosis b. Varices C. Dilatation D.None

13. Can you detect any aneurism associated to this abnormality?

    No *Pre-nidal* *nidal* *post-nidal*

14. Can you observe an extra-nidal arterial-venous fistula in this MR examination?

    Yes *No*

15. How confident are you of this assessment?

    Not entirely confident *Confident* *Highly confident*